3D Architected Battery Electrodes for Exploring Battery Kinetics from Nano to Millimeter

Thesis by

Kai Narita

In Partial Fulfillment of the Requirements for

the Degree of

Doctor of Philosophy

CALIFORNIA INSTITUTE OF TECHNOLOGY

Pasadena, California

2021

Defended May 17, 2021

Kai Narita
ORCID: 0000-0002-3867-8234

ACKNOWLEDGEMENTS

I have been very fortunate to enjoy the journey at Caltech, which has guided me to the scientist I wanted to be. One of the biggest reasons I chose Caltech to spend my PhD life was to build up my foundation of science. No matter how far I have come as a scientist, this is never achievable without the enthusiastic and sincere support from my advisor, Prof. Julia R. Greer. Before coming to Caltech, I was moved by her paper about 3D architecture and the concept of introducing "architecture" to the foundation of materials science. I am grateful for this opportunity to spend 5 years in her group and to pursue building the concept of 3D architecture in battery fields. I would also like to thank my committee members, Prof. Bhattacharya, Prof. Faber, and Prof. See.

Since I started working on batteries, which I had almost zero knowledge about when I started, I always appreciate all the patience, support, and collaboration from former and current battery-troops in the Greer group: Dr. Heng Yang, Dr. John Throne, Dr. Xiaoxing Xia, Dr. Dylan Tozier, Dr. Mike Citrin, Kewei Xu, Max Saccone, Fernando Villafuerte, Yuchun Sun, and Chan Kim. I would like to especially thank Xiaoxing and Heng for sharing their knowledge and philosophy of science. The scientific discussion with Dr. Akira Kudo and Dr. Ye Shi was joyful, and I have learned a lot from their deep thoughts. I appreciate their tremendous help in building my scientific foundation. Expanding knowledge and technology is one of the challenges I went through at Caltech, and this has been achieved by thankful collaboration with Dr. Forrest Laskowski, Dr. Yunbin Guan, Dr. Chi Ma, and Carol Garland. I also would like to thank Brandan Taing and Andrew Friedman for the opportunities to explore the potentials of 3D carbon electrodes together. The time in the Greer group gave me pleasant moments with a variety of office mates as I hopped around a couple of offices; I would like to thank Jane, Anthony, Luizetta, Kewei, Eric, and Xiaoyue, and all the other Greer group members.

I also would like to acknowledge supports and international network outside Caltech, from the Takenaka Foundation and the Masason Foundation. I would like to thank Prof. Equo Kobayashi, who saw off my voyage and always support me from overseas. I am thankful to

my roommates, Masashi, Kyuta, and Taichi, who shared our social life and fun moments, especially under the covid-19 situation. I would like to express my enormous gratitude to my girlfriend, Shino Yamasaki, who support me and even recorded my moments at Caltech (and published on YouTube); I am so lucky to celebrate this journey with her. I would like to thank my family, mom, dad, and siblings, Ran, and Riku, who always supported me from overseas and helped me do remote work at home in Japan while the Caltech campus was closed. I have spent my PhD journey at different places and with different people in the world, and all the scientific lessons shape into this thesis, which is the end of my PhD and the commencement of myself as a scientist.

ABSTRACT

The ability to design a particular geometry of porous electrodes at multiple length scales in a lithium-ion battery can significantly and positively influence battery performance because it enables control over kinetics and trajectories of ion and electron transport. None of the existing methods of engineering electrode structure is capable of creating 3D architected electrodes designed with independent and flexible form-factors at multiscale that are also resilient against cell packaging pressure. In addition, battery kinetics coupled at multiscale from ion transport in an electrolyte to solid electrolyte interphase (SEI) growth has only been studied by numerical simulations, but has never been experimentally explored.

In this thesis, we demonstrate an additive manufacturing technique to engineer porous electrode structure in 3D and explore battery kinetics at multiscale. First, we develop 3D architected carbon electrodes, whose structural factors are independently controlled and whose dimensions span microns to centimeters, using digital light processing and pyrolysis. These free-standing lattice electrodes are disordered graphitic carbon composed of several stacked graphitic layers that are mechanically robust. Galvanostatic cycling using these architected carbon electrodes showed sloping capacity, typically observed in pyrolyzed carbon electrodes. We discuss the modified rate performance of the 3D architected carbon electrodes in the framework of ion transport kinetics in the electrode vs. electrolyte and overpotential, enabled by controlling structural factors of battery electrodes, including porosity, surface morphology, electrode thickness, and beam diameter, whose length scales range from nano to millimeter.

We then explore battery kinetics associated with SEI using deterministic, mechanically resilient, and thick 3D architected carbon electrodes, which allow us to study the formation, structure-resistance relationship, and position-dependent growth of SEI by combining the newly developed *in operando* DC-based technique and post-characterization using secondary ion mass spectroscopy. The amount of Li in SEI agrees with capacity losses, and the amount of F in SEI showed a strong linear correlation with SEI resistance evolutions. The position-dependent SEI growth was experimentally explored; the Li amount in SEI

along the electrode thickness agrees with the simulation results in prior work, but the F amount in SEI showed the opposite tendency, suggesting modeling of multilayer SEI is necessary to predict precisely battery aging especially for thick electrodes. Our work demonstrates the use of 3D architected electrodes as a model system to explore multiscale kinetics in Li-ion batteries.

PUBLISHED CONTENT AND CONTRIBUTIONS

Chapter 2, Chapter 3, and Chapter 4 have been adopted from

1. Narita, K.; Citrin, M. A.; Yang, H.; Xia, X.; Greer, J. R. 3D Architected Carbon Electrodes for Energy Storage. *Adv. Energy Mater*. 2021, 11, 1–13, doi:10.1002/aenm.202002637.

Contributions: K.N. designed and fabricated samples, performed and analyzed the experiments, and wrote the manuscript.

Chapter 5 has been adopted from

2. Narita, K.; Greer, J. R. Solid Electrolyte Interphase Growth, Structure, and Properties at multiple length scales. *In Preparation.*

Contributions: K.N. participated in the conception of the project, designed and fabricated samples, performed and analyzed the experiments, and wrote the manuscript.

TABLE OF CONTENTS

LIST OF ILLUSTRATIONS

LIST OF TABLES

Chapter 1

INTRODUCTION: BATTERY KINETICS AND ENGINEERED ELECTRODE STRUCTURES

1.1. Introduction to Lithium-Ion Batteries as Electrochemical Devices

Lithium (Li)-ion batteries are essential to supporting our modern life and realizing a sustainable society with ever-growing energy needs. The current utilization of Li-ion batteries is a huge accomplishment if we consider the complexity of Li-ion batteries: a wide range of materials and kinetics at multiple spatial and temporal scales. The materials assembled in Li-ion batteries include carbon, organic materials, metals, and oxides, which enable reversible electrochemical reactions on material interfaces and transport of electrons and Li-ions through these materials. These kinetics span from nanometers (atomic scale) to centimeters (battery cell scale) in space and from femtoseconds (reaction time) to years (aging period) in time.

Tremendous efforts on material development in academia and industry have led to the commercialization of safe and rechargeable Li-ion batteries. Whittingham proposed the concept of current Li-ion batteries in the 1970s based on his discovery of reversible Li intercalations in titanium disulfide [1]. Since then, significant developments and discoveries of intercalation materials have followed: Li_xMO_2 by Murphy in 1978 [2] and $LiCoO_2$ by Goodenough in 1980 [3], and reversible electrochemical intercalation of Li in graphite anode by Yazami in 1983 [4]. These developments facilitated the industry to produce commercial Li-ion battery cells: Yoshino patented carbon as an anode material for Li-ion batteries in 1985, and in 1986 he also patented the Li-ion battery cell that combined carbon anode and $LiCoO_2$ cathode. In the same period, Harada in Sony filed a patent of Li-ion batteries composed of petroleum coke as an anode material in 1988, which led to the first commercial Li-ion battery from Sony in 1991. Graphite electrodes, which are the current standard anode materials, started being used after Dahn demonstrated in 1990 that ethylene carbonate electrolyte prevented exfoliations of graphite during lithiation by forming stable SEI. Since

the initial commercialization, substantial efforts have led to further development of Li-ion batteries, for instance, improved energy density from ~90 Wh kg^{-1} in 1991 to ~250 Wh kg^{-1} in 2020 [5,6].

1.2. Transport Kinetics in Battery Operations

Discoveries and developments of materials are not only enablers of realizing high energy density and high power density of Li-ion batteries to date; understanding of battery kinetics facilitates the development of efficient battery cell architectures. During discharge, Li stored in cathodes undergoes spontaneous oxidation reaction and transport through an organic electrolyte, then it is reduced and stored in anodes. Simultaneously, electrons are transported from cathodes through metal current collectors toward external circuits, which allows the powering of electric devices. The reverse reactions and transport occur in a charging process that applies voltages between anodes and cathodes. The Li-ion transport in an electrolyte is driven by the applied voltage or an electrical field (i.e. migration), and concentration gradients (i.e. diffusion) if counter-ions contribute to the current. The reduced Li is also transported from an electrode surface toward the center, which is driven by the concentration gradients (diffusion). If voltages are operated beyond the stability window of the electrolyte, the electrolyte decomposes on the interface with electrodes. For anodes, the electrolyte decomposition or reduction reaction occurs to form a solid electrolyte interphase (SEI) if the lowest unoccupied molecular orbital (LUMO) of the organic electrolyte is lower than the Fermi energy level of the anode material [7]. The SEI growth is a key driver for battery degradation over long-term operations.

In Li-ion batteries with liquid electrolytes, transport rates in electrolyte, electrode, and SEI are several orders of magnitude different, which determines the length scales that effectively influence transport. Transport in an electrolyte is influenced by electrode thickness and porous electrode structure, spanning sub-millimeter to micrometer length scales. The feature size of electrodes determines transport length in an electrode, ranging from micron to sub-micron scales. Transport through SEI ranges nanometer scales. By considering these length scales of transport kinetics, controlling form factors of porous electrodes at multiple length scales enables engineering kinetics and trajectories of transports in batteries, resulting in

enhanced power density. Another important key figure of merit is energy density, determined by a fraction of active materials. The trade-off relationship between energy density and power density is a challenge for battery electrodes, especially for cost-effective and commercialized slurry electrodes.

1.3.Battery Electrode Structures and Influences

Most commercial Li-ion battery electrodes are slurry, stochastic porous structures composed of active material particles, binders, and conductive additives. The complex structure determines transport trajectories of ions and electrons, limiting the attainable power density of Li-ion batteries. The parameters to quantify a porous structure are porosity ε and tortuosity τ, which is geometrically defined as the square ratio of ion transport length across the electrode and electrode thickness [8]. These parameters are used to calculate the effective diffusion coefficient:

$$D_e = D\frac{\varepsilon}{\tau} \tag{1.1}$$

where D indicates diffusion coefficient in a bulk electrolyte solution. The tortuosity of porous electrode structure increases non-linearly to porosity as represented by Bruggeman's relation

$$\tau = \varepsilon^{-\alpha} \tag{1.2}$$

where α indicates Bruggeman exponent, which is commonly assigned to be 0.5, proven for the media mixed with insulating sphere monodisperse particles [9]. The correct value of α has been discussed by modeling and experiments that quantify diffusivity such as electrochemical impedance spectroscopy (EIS) in a symmetric cell [10–13] and 3D imaging of porous structure using X-ray tomography [11,14,15] or a focused ion beam (FIB)/SEM approach [16,17].

Eq. 1.1 and Eq. 1.2 suggest that the transport rate and a fraction of active materials (i.e. inverse of porosity) are in a trade-off relationship. One strategy to improve the energy density of stacked cells is increasing the thickness of electrodes and minimizing inactive materials

such as current collectors [18], but the thick stochastic structure is suffered from high tortuosity, which reduces power density.

In addition to the influence of high tortuosity attributed to stochastic structure on transport, local potentials within a stochastic structure can differ from globally monitored potentials, which may cause undesired phenomena such as heterogeneous SEI formation and local lithium plating. To overcome these trade-off relationships and challenges, methods to control electrode structures have been explored.

1.4. Methods to Control Porous Electrode Structure

There has been an interest in engineer battery porous structure because it enables minimizing tortuosity and attaining high power density with thick electrodes, which provide high energy density at the cell level. Here, the engineered porous electrode structures are summarized.

Slurry electrodes with anisotropic pores:

Slurry electrodes with anisotropic porous structures are manufactured by aligning active materials particles by external fields [19,20] or ice-templating methods [21–23] in the slurry making process. Laser ablating (cutting grooves) into the calendared slurry electrode enables anisotropic porous structure as well [24]. These methods can provide straight large channels for efficient Li-ion transport compared with conventional slurry electrode structures, which mitigate the trade-off relationship of energy density and power density (Figure 1. 1). Billaud et al. used a magnetic field to align iron oxide nanoparticles-loaded graphite flakes along the though-thickness direction [19]. Park et al. demonstrated in 2019 that laser structured electrodes enhanced the rate capability of the electrode and specific energy while improving or retaining the power density, due to increased diffusion homogeneity and electrolyte wettability [25]. The laser ablation technique can be incorporated into the existing roll-to-roll cell manufacturing facility and is scalable [26].

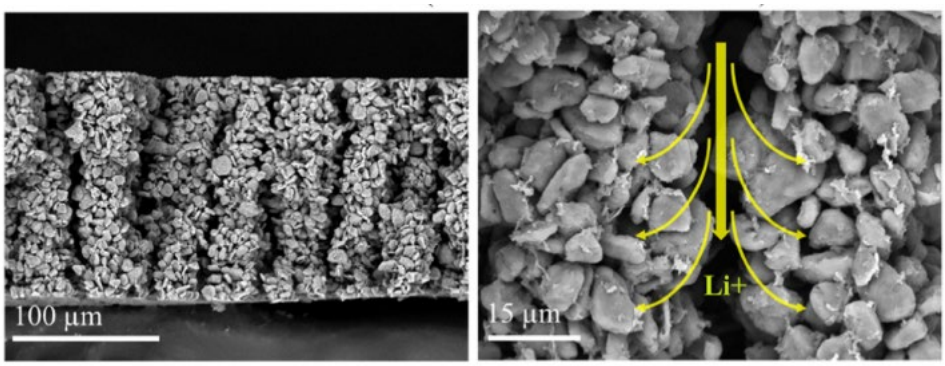

Figure 1. 1 SEM images at different magnifications of a superior graphite anode manufactured with freeze-tape-casting at Lawrence Berkeley National Laboratory. Li-ion transport in primary (channel spacing) and secondary region (channel width) are drawn. Adopted from [23].

Slurry electrodes filled in 3D conductive framework:

The 3D conductive framework or 3D current collector is used to support slurry electrodes physically and electrically [27–33]. The 3D metal current collectors such as nickel mesh and copper mesh (Figure 1. 2) are commercially available, and the 3D carbon framework is made by pyrolysis of commercially available polymer foam or chemical vapor deposition on the 3D metal current collector. These 3D current collectors are reviewed in the literature [34]. Slurry electrodes filled in the 3D conductive framework can increase a total electrode thickness and areal mass loading by minimizing electron transport length between the current collector and active material, as against conventional slurry electrodes whose electron transport length depends on the electrode thickness. In the case of a stochastic 3D current collector, ionic transport trajectories in an electrolyte may be tortuous and limit power density. An aligned conductive framework has been developed by aligned carbon fibers [35] and carbonization of wood [36], which showed low tortuosity and improved rate performance.

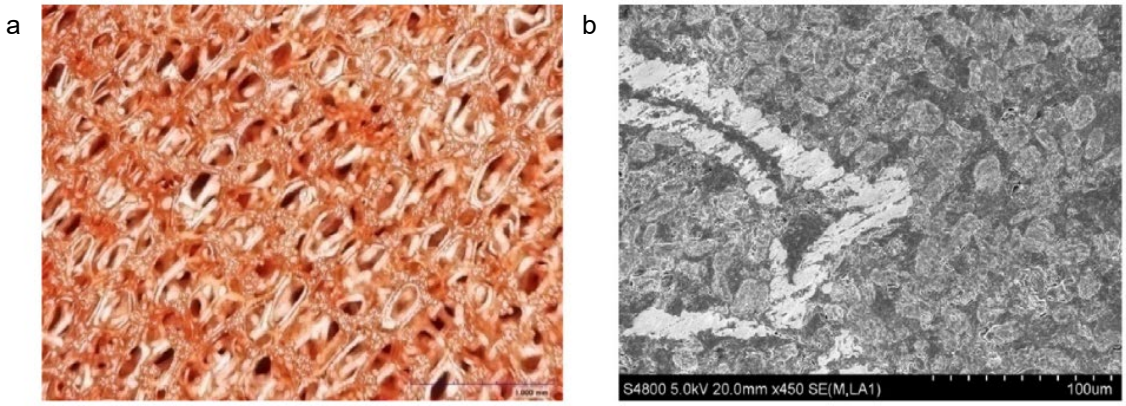

Figure 1. 2 Images of 3D foam structures and prepared electrodes. (a) Cu foam as a current collector for negative electrode; (b) graphite negative electrode using Cu foam. Adopted from [28]

Thick monolith electrodes:

The thick monolith electrodes or bulk electrodes are binder-free electrodes thicker than conventional slurry electrodes (~100 μm-thick), which have been developed by powder-sintering techniques [37–39]. Lai demonstrated that thick monolith electrodes of lithium cobalt oxide reached their relative density up to 87 vol.%, enabling high energy density (600 W L^{-1}, Figure 1. 3) [37], although all the structural factors such as porosity, tortuosity, and transport lengths are coupled one another like slurry electrodes.

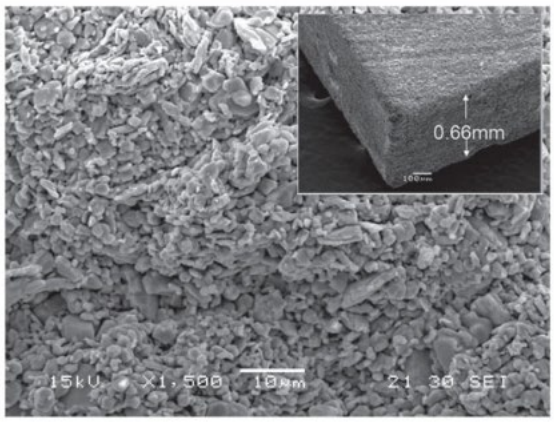

Figure 1. 3 SEM image of a 660-μm-thick, sintered monolithic cathode (inset) and cross-section of a fracture surface from a 74% dense sintered cathode. Adopted from [37].

Electrode film on 3D conductive framework:

Coating active materials on the 3D current collector allow precise control of Li transport length in an electrode and minimize electron transport length. The morphology of the 3D current collector ranges from stochastic to periodic structure. Zhang et al. demonstrated a ~30 nm-thick MnO_2 coated 3D inverse opal structured current collector (Figure 1. 4), which enabled 90%-charge in 2 minutes due to efficient ion and electron pathways [40]. This technique allows independent control of diffusion length in an electrode and a fraction of active materials by modifying coating thickness and structure of 3D current collector. Despite very promising battery performance at lab scale, the existing challenges for practical application include uniform loading of active materials in a scaffold system, which are controlled within 2% in modern manufacturing methods [41].

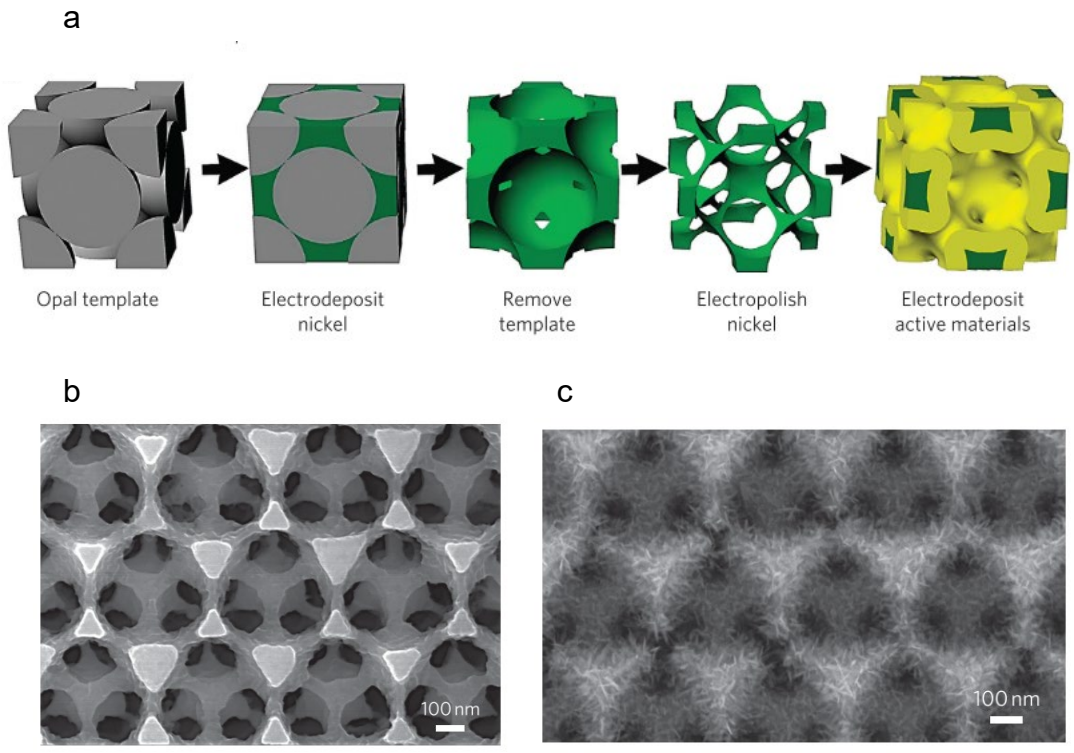

Figure 1. 4 MnO_2 coated 3D inverse opal structured current collector. (a) Bicontinuous electrode fabrication process. The electrolytically active phase is yellow and the porous metal current collector is green. The electrolyte fills the remaining pores. (b) Nickel inverse opal after electropolishing. (c) MnO_2/nickel composite cathode

3D interconnected porous electrodes by sacrificial template:

3D porous monolith structures composed of active materials using sacrificial templates have been developed by various template methods, including but not limited to the usage of monodisperse particles (i.e. inverse opal) [42], bio-template (Figure 1. 5) [43], bicontinuous nanoporous alloy [44], and salt-template [45]. Control capabilities of electrode structures depend on sacrificial templates; form factors of inverse opal structures are similar, bio-template structure alters by individual differences of natural materials, bicontinuous nanoporous alloy and selective etching allow the control of solid-diffusion length and fraction of active materials [44], and the usage of the salt particles as a space holder can only control pore size distribution and porosity, but not tortuosity or solid-diffusion length.

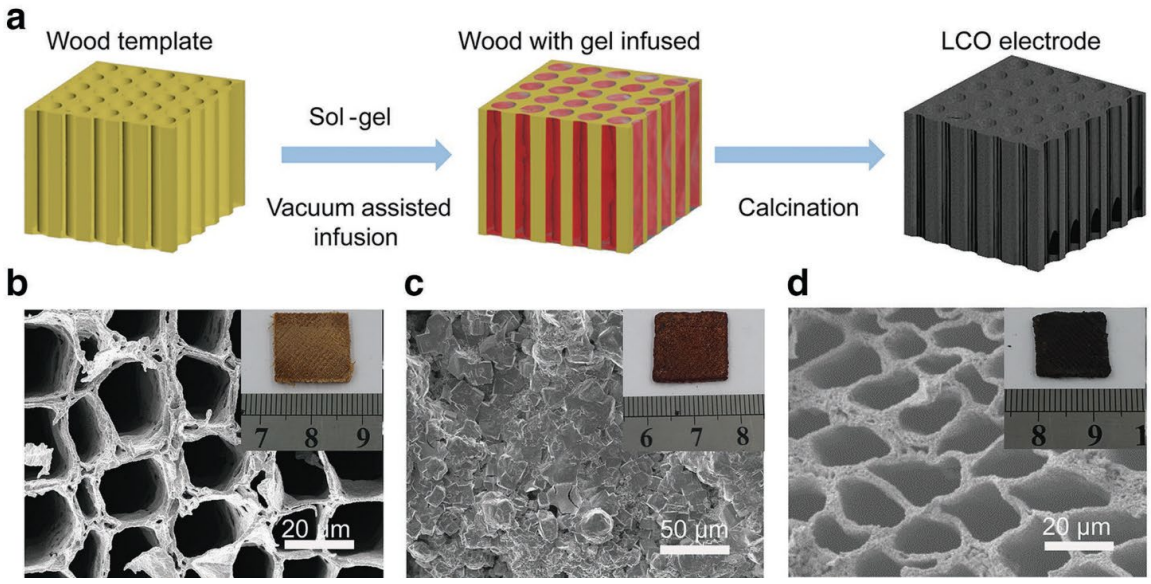

Figure 1. 5 The fabrication and characterization of ultrathick bulk LCO cathodes by wood templating. (a) The illustration of fabrication procedure of ultrathick LCO cathode by wood templating. Top views of (b) original wood, (c) original wood after sol infusion and gel formation, and (d) LCO electrode. The inserts in (b)–(d) are corresponding photos of samples. Adopted from [43].

Extrusion-based 3D printing of electrodes

The extrusion-based 3D printing is capable of macro/micro-control of depositing slurry electrodes, which allows making interdigitated microbattery architectures (Figure 1. 6)

[46,47]. The fraction and size of active materials particles are tuned to obtain suitable rheological properties for a precise extrusion, limiting the range of controllable structural factors such as diffusion length in an electrode. This extrusion-based 3D printing can be combined with other techniques such as applying an external electric field to control extruded slurry architecture [20].

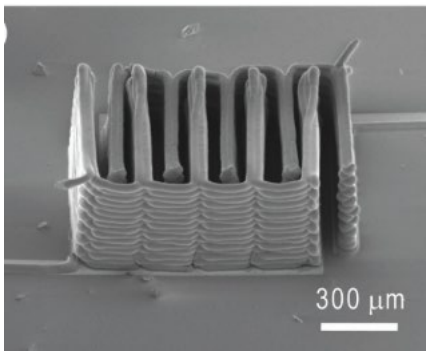

Figure 1. 6 SEM image of printed and annealed 16-layer interdigitated LTO-LFP electrode architectures. Adopted from [47].

Lithography-based additive manufacturing of electrodes

The lithography-based method has been actively investigated to aim at 3D interdigitated batteries (Figure 1. 7) [48–51]. Form factors of electrode structures are controllable, although reported battery electrodes fabricated by lithography-based techniques showed only 2.5D structure such as pillar arrays, whose form factors are not controllable along the direction normal to a substrate. This technique is often combined with other methods such as thin-film coating [49] and slurry inclusion [48].

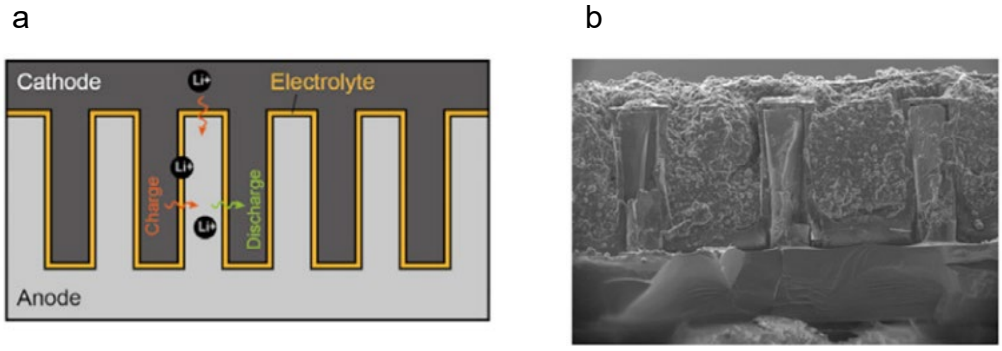

Figure 1. 7 3D interdigitated full batteries using lithography-based method. (a) Charging schematic of complete 3D battery. (b) SEM image of full 3D battery composed of SU-8-Coated Silicon Arrays and infiltrated NCA cathodes. Adopted from [48].

1.5. Thesis Overview

The summarized electrode structures demonstrate improved battery performance compared with conventional slurry electrodes, but still limit their control capabilities of structural factors; for instance, the usage of slurry electrodes cannot decouple tortuosity and porosity, and template methods are not capable of varying tortuosity. None of these methods is capable of creating 3D-architected electrodes that are designed with independent and flexible form-factors and are also resilient against cell packaging pressure. The aim of this thesis is to demonstrate an additive manufacturing technique to engineer porous electrode structure in 3D with multiple length scale form factors, explore battery kinetics including transport in an electrode, an electrolyte, and SEI, which spans from nano to millimeter using the developed 3D architected electrodes, and provide guidelines for optimizing electrode structures for superior battery performance including energy density, power density, and cycle life.

Chapter 2 introduces a novel and simple method to create 3D architected carbon electrodes, and demonstrates characterizations of 3D architected carbon for microstructure and mechanical behaviors.

Chapter 3 demonstrates the 3D architected carbon electrodes as Li-ion battery anode materials using galvanostatic cycling. We discuss the capacity gain mechanism of the fabricated 3D architected carbon electrodes with the understanding of microstructure.

Chapter 4 discusses electrode structures and electrochemical performance relationship by independently controlling structural factors of 3D architected carbon electrodes from micrometer to millimeter. We independently control feature size, electrode thickness, porosity, and surface morphology, and discuss rate performance with the framework of diffusion in electrode and electrolyte.

Chapter 5 discusses battery kinetics associated with SEI using 3D architected carbon electrodes, electrochemical characterizations, and nano-secondary ion mass spectroscopy (SIMS). Along the way, we develop a new *in operando* technique to investigate overpotential evolutions using direct currents (DC), which allows us to understand SEI resistance evolution during battery cycling. SIMS results facilitate elucidating SEI structure throughout deterministic 3D architected carbon electrodes. We propose a big picture of kinetics associated with SEI, including formation and structure-property relationship, and suggest their distributions throughout porous electrodes at the millimeter scale.

Lastly, in Chapter 6, we summarize the lessons learned from the development of 3D architected carbon electrodes and explorations of battery kinetics at multiple length scales, and provide an outlook for further opportunities of using 3D architected electrodes for exploring scientific questions and engineering applications.

REFERENCES

1. Whittingham, M.S. Electrical energy storage and intercalation chemistry. *Science.* **1976**, *192*, 1126–1127, doi:10.1126/science.192.4244.1126.

2. Murphy, D.W.; Di Salvo, F.J.; Carides, J.N.; Waszczak, J. V. Topochemical reactions of rutile related structures with lithium. *Mater. Res. Bull.* **1978**, *13*, 1395–1402, doi:10.1016/0025-5408(78)90131-9.

3. Mizushima, K.; Jones, P.C.; Wiseman, P.J.; Goodenough, J.B. LixCoO2 (0<x<-1): A new cathode material for batteries of high energy density. *Mater. Res. Bull.* **1980**, *15*, 783–789, doi:10.1016/0025-5408(80)90012-4.

4. Yazami, R.; Touzain, P. A reversible graphite-lithium negative electrode for electrochemical generators. *J. Power Sources* **1983**, *9*, 365–371, doi:10.1016/0378-7753(83)87040-2.

5. Armand, M.; Axmann, P.; Bresser, D.; Copley, M.; Edström, K.; Ekberg, C.; Guyomard, D.; Lestriez, B.; Novák, P.; Petranikova, M.; et al. Lithium-ion batteries – Current state of the art and anticipated developments. *J. Power Sources* **2020**, *479*, doi:10.1016/j.jpowsour.2020.228708.

6. Masias, A.; Marcicki, J.; Paxton, W.A. Opportunities and challenges of lithium ion batteries in automotive applications. *ACS Energy Lett.* **2021**, *6*, 621–630, doi:10.1021/acsenergylett.0c02584.

7. Tan, J.; Matz, J.; Dong, P.; Shen, J.; Ye, M. A Growing appreciation for the role of lif in the solid electrolyte interphase. *Adv. Energy Mater.* **2021**, doi:10.1002/aenm.202100046.

8. Ebner, M.; Wood, V. Tool for tortuosity estimation in lithium ion battery porous electrodes. *J. Electrochem. Soc.* **2014**, *162*, A3064–A3070, doi:10.1149/2.0111502jes.

9. Tjaden, B.; Cooper, S.J.; Brett, D.J.; Kramer, D.; Shearing, P.R. On the origin and application of the Bruggeman correlation for analysing transport phenomena in electrochemical systems. *Curr. Opin. Chem. Eng.* **2016**, *12*, 44–51, doi:10.1016/j.coche.2016.02.006.

10. Pouraghajan, F.; Christensen, J.; Knight, H.; Wray, M.; Mazzeo, B.; Subbaraman, R.; Wheeler, D. Quantifying tortuosity of porous li-ion battery electrodes: comparing polarization-interrupt and blocking-electrolyte methods. *J. Electrochem. Soc.* **2018**, *165*, A2644–A2653, doi:10.1149/2.0611811jes.

11. Lim, C.; Yan, B.; Kang, H.; Song, Z.; Lee, W.C.; De Andrade, V.; De Carlo, F.; Yin, L.; Kim, Y.; Zhu, L. Analysis of geometric and electrochemical characteristics of lithium cobalt oxide electrode with different packing densities. *J. Power Sources* **2016**, *328*, 46–55, doi:10.1016/j.jpowsour.2016.07.119.

12. Landesfeind, J.; Hattendorff, J.; Ehrl, A.; Wall, W.A.; Gasteiger, H.A. Tortuosity Determination of battery electrodes and separators by impedance spectroscopy. *J. Electrochem. Soc.* **2016**, *163*, A1373–A1387, doi:10.1149/2.1141607jes.

13. Inoue, G.; Kawase, M. Numerical and experimental evaluation of the relationship between porous electrode structure and effective conductivity of ions and electrons in lithium-ion batteries. *J. Power Sources* **2017**, *342*, 476–488, doi:10.1016/j.jpowsour.2016.12.098.

14. Chung, D.W.; Ebner, M.; Ely, D.R.; Wood, V.; Edwin García, R. Validity of the Bruggeman relation for porous electrodes. *Model. Simul. Mater. Sci. Eng.* **2013**, *21*, 1–16, doi:10.1088/0965-0393/21/7/074009.

15. Ebner, M.; Chung, D.W.; García, R.E.; Wood, V. Tortuosity anisotropy in lithium-ion battery electrodes. *Adv. Energy Mater.* **2014**, *4*, 1–6, doi:10.1002/aenm.201301278.

16. Hutzenlaub, T.; Asthana, A.; Becker, J.; Wheeler, D.R.; Zengerle, R.; Thiele, S. FIB/SEM-based calculation of tortuosity in a porous LiCoO2cathode for a Li-ion battery. *Electrochem. Commun.* **2013**, *27*, 77–80, doi:10.1016/j.elecom.2012.11.006.

17. Ender, M.; Joos, J.; Carraro, T.; Ivers-Tiffée, E. Three-dimensional reconstruction of a composite cathode for lithium-ion cells. *Electrochem. Commun.* **2011**, *13*, 166–168, doi:10.1016/j.elecom.2010.12.004.

18. Gallagher, K.G.; Trask, S.E.; Bauer, C.; Woehrle, T.; Lux, S.F.; Tschech, M.; Lamp, P.; Polzin, B.J.; Ha, S.; Long, B.; et al. Optimizing areal capacities through understanding the limitations of lithium-ion electrodes. *J. Electrochem. Soc.* **2016**, *163*, A138–A149, doi:10.1149/2.0321602jes.

19. Billaud, J.; Bouville, F.; Magrini, T.; Villevieille, C.; Studart, A.R. Magnetically aligned graphite electrodes for high-rate performance Li-ion batteries. *Nat. Energy* **2016**, *1*, 1–6, doi:10.1038/nenergy.2016.97.

20. Li, J.; Liang, X.; Liou, F.; Park, J. Macro-/Micro-Controlled 3D Lithium-Ion batteries via additive manufacturing and electric field processing. *Sci. Rep.* **2018**, *8*, 1–11, doi:10.1038/s41598-018-20329-w.

21. Huang, C.; Dontigny, M.; Zaghib, K.; Grant, P.S. Low-tortuosity and graded lithium ion battery cathodes by ice templating. *J. Mater. Chem. A* **2019**, *7*, 21421–21431, doi:10.1039/c9ta07269a.

22. Huang, C.; Grant, P.S. Coral-like directional porosity lithium ion battery cathodes by ice templating. *J. Mater. Chem. A* **2018**, *6*, 14689–14699, doi:10.1039/c8ta05049j.

23. Usseglio-Viretta, F.L.E.; Mai, W.; Colclasure, A.M.; Doeff, M.; Yi, E.; Smith, K. Enabling fast charging of lithium-ion batteries through secondary- /dual-pore network: Part I–Analytical diffusion model. *Electrochim. Acta* **2020**, *342*, 136034, doi:10.1016/j.electacta.2020.136034.

24. Chen, K.H.; Namkoong, M.J.; Goel, V.; Yang, C.; Kazemiabnavi, S.; Mortuza, S.M.; Kazyak, E.; Mazumder, J.; Thornton, K.; Sakamoto, J.; et al. Efficient fast-charging of lithium-ion batteries enabled by laser-patterned three-dimensional graphite anode architectures. *J. Power Sources* **2020**, *471*, 228475,

doi:10.1016/j.jpowsour.2020.228475.

25. Park, J.; Hyeon, S.; Jeong, S.; Kim, H.J. Performance enhancement of Li-ion battery by laser structuring of thick electrode with low porosity. *J. Ind. Eng. Chem.* **2019**, *70*, 178–185, doi:10.1016/j.jiec.2018.10.012.

26. Pfleging, W. Recent progress in laser texturing of battery materials: A review of tuning electrochemical performances, related material development, and prospects for large-scale manufacturing. *Int. J. Extrem. Manuf.* **2021**, *3*, doi:10.1088/2631-7990/abca84.

27. Cheng, X.B.; Peng, H.J.; Huang, J.Q.; Zhu, L.; Yang, S.H.; Liu, Y.; Zhang, H.W.; Zhu, W.; Wei, F.; Zhang, Q. Three-dimensional aluminum foam/carbon nanotube scaffolds as long- and short-range electron pathways with improved sulfur loading for high energy density lithium-sulfur batteries. *J. Power Sources* **2014**, *261*, 264–270, doi:10.1016/j.jpowsour.2014.03.088.

28. Wang, J.S.; Liu, P.; Sherman, E.; Verbrugge, M.; Tataria, H. Formulation and characterization of ultra-thick electrodes for high energy lithium-ion batteries employing tailored metal foams. *J. Power Sources* **2011**, *196*, 8714–8718, doi:10.1016/j.jpowsour.2011.06.071.

29. Hu, L.; La Mantia, F.; Wu, H.; Xie, X.; McDonough, J.; Pasta, M.; Cui, Y. Lithium-ion textile batteries with large areal mass loading. *Adv. Energy Mater.* **2011**, *1*, 1012–1017, doi:10.1002/aenm.201100261.

30. Gaikwad, A.M.; Khau, B. V.; Davies, G.; Hertzberg, B.; Steingart, D.A.; Arias, A.C. A high areal capacity flexible lithium-ion battery with a strain-compliant design. *Adv. Energy Mater.* **2015**, *5*, 1–11, doi:10.1002/aenm.201401389.

31. Ji, H.; Zhang, L.; Pettes, M.T.; Li, H.; Chen, S.; Shi, L.; Piner, R.; Ruoff, R.S. Ultrathin graphite foam: A three-dimensional conductive network for battery electrodes. *Nano Lett.* **2012**, *12*, 2446–2451, doi:10.1021/nl300528p.

32. Yang, G.-F.; Song, K.-Y.; Joo, S.-K. Ultra-thick Li-ion battery electrodes using different cell size of metal foam current collectors. *RSC Adv.* **2015**, *5*, 16702–16706, doi:10.1039/C4RA14485F.

33. Liu, W.; Chen, Z.; Zhou, G.; Sun, Y.; Lee, H.R.; Liu, C.; Yao, H.; Bao, Z.; Cui, Y. 3D porous sponge-inspired electrode for stretchable lithium-ion batteries. *Adv. Mater.* **2016**, *28*, 3578–3583, doi:10.1002/adma.201505299.

34. Jin, S.; Jiang, Y.; Ji, H.; Yu, Y. Advanced 3D current collectors for lithium-based batteries. *Adv. Mater.* **2018**, 1802014, doi:10.1002/adma.201802014.

35. Shi, B.; Shang, Y.; Pei, Y.; Pei, S.; Wang, L.; Heider, D.; Zhao, Y.Y.; Zheng, C.; Yang, B.; Yarlagadda, S.; et al. Low tortuous, highly conductive, and high-areal-capacity battery electrodes enabled by through-thickness aligned carbon fiber framework. *Nano Lett.* **2020**, *20*, 5504–5512, doi:10.1021/acs.nanolett.0c02053.

36. Chen, C.; Zhang, Y.; Li, Y.; Kuang, Y.; Song, J.; Luo, W.; Wang, Y.; Yao, Y.; Pastel, G.; Xie, J.; et al. Highly conductive, lightweight, low-tortuosity carbon frameworks as ultrathick 3d current collectors. *Adv. Energy Mater.* **2017**, *7*, 3–10, doi:10.1002/aenm.201700595.

37. Lai, W.; Erdonmez, C.K.; Marinis, T.F.; Bjune, C.K.; Dudney, N.J.; Xu, F.; Wartena, R.; Chiang, Y.M. Ultrahigh-energy-density microbatteries enabled by new electrode architecture and micropackaging design. *Adv. Mater.* **2010**, *22*, 139–144, doi:10.1002/adma.200903650.

38. Jiang, J.J.; Gasik, M.; Laine, J.; Lampinen, M. Electrochemical evaluation of sintered metal hydride electrodes for electric vehicle applications. *J. Alloys Compd.* **2001**, *322*, 281–285, doi:10.1016/S0925-8388(01)01257-9.

39. Qin, X.; Wang, X.; Xie, J.; Wen, L. Hierarchically porous and conductive LiFePO4bulk electrode: Binder-free and ultrahigh volumetric capacity Li-ion cathode. *J. Mater. Chem.* **2011**, *21*, 12444–12448, doi:10.1039/c1jm11642h.

40. Zhang, H.; Yu, X.; Braun, P. V Three-dimensional bicontinuous ultrafast-charge and -discharge bulk battery electrodes. *Nat. Nanotechnol.* **2011**, *6*, 277–281, doi:10.1038/nnano.2011.38.

41. Braun, P. V.; Cook, J.B. Deterministic Design of Chemistry and Mesostructure in Li-Ion Battery Electrodes. *ACS Nano* **2018**, *12*, 3060–3064, doi:10.1021/acsnano.8b01885.

42. Lee, K.T.; Lytle, J.C.; Ergang, N.S.; Oh, S.M.; Stein, A. Synthesis and rate performance of monolithic macroporous carbon electrodes for lithium-ion secondary batteries. *Adv. Funct. Mater.* **2005**, *15*, 547–556, doi:10.1002/adfm.200400186.

43. Lu, L.L.; Lu, Y.Y.; Xiao, Z.J.; Zhang, T.W.; Zhou, F.; Ma, T.; Ni, Y.; Yao, H. Bin; Yu, S.H.; Cui, Y. Wood-inspired high-performance ultrathick bulk battery electrodes. *Adv. Mater.* **2018**, *30*, doi:10.1002/adma.201706745.

44. Wang, C.; Chen, Q. Reduction-induced decomposition: spontaneous formation of monolithic nanoporous metals of tunable structural hierarchy and porosity. *Chem. Mater.* **2018**, *30*, 3894–3900, doi:10.1021/acs.chemmater.8b01431.

45. Elango, R.; Demortière, A.; De Andrade, V.; Morcrette, M.; Seznec, V. Thick Binder-Free Electrodes for Li-ion battery fabricated using templating approach and spark plasma sintering reveals high areal capacity. *Adv. Energy Mater.* **2018**, *1703031*, 1–8, doi:10.1002/aenm.201703031.

46. Fu, K.; Wang, Y.; Yan, C.; Yao, Y.; Chen, Y.; Dai, J.; Lacey, S.; Wang, Y.; Wan, J.; Li, T.; et al. Graphene oxide-based electrode inks for 3d-printed lithium-ion batteries. *Adv. Mater.* **2016**, *28*, 2587–2594, doi:10.1002/adma.201505391.

47. Sun, K.; Wei, T.S.; Ahn, B.Y.; Seo, J.Y.; Dillon, S.J.; Lewis, J.A. 3D printing of interdigitated Li-ion microbattery architectures. *Adv. Mater.* **2013**, *25*, 4539–4543, doi:10.1002/adma.201301036.

48. Hur, J.I.; Smith, L.C.; Dunn, B. High areal energy density 3D lithium-ion

microbatteries. *Joule* **2018**, 1–15, doi:10.1016/j.joule.2018.04.002.

49. Ning, H.; Pikul, J.H.; Zhang, R.; Li, X.; Xu, S.; Wang, J.; Rogers, J.A.; King, W.P.; Braun, P. V. Holographic patterning of high-performance on-chip 3D lithium-ion microbatteries. *Proc. Natl. Acad. Sci. U. S. A.* **2015**, *112*, 6573–6578, doi:10.1073/pnas.1423889112.

50. Cirigliano, N.; Sun, G.; Membreno, D.; Malati, P.; Kim, C.J.; Dunn, B. 3D architectured anodes for lithium-ion microbatteries with large areal capacity. *Energy Technol.* **2014**, *2*, 362–369, doi:10.1002/ente.201402018.

51. Wang, C.; Taherabadi, L.; Jia, G.; Madou, M.; Yeh, Y.; Dunn, B. C-MEMS for the manufacture of 3D microbatteries. *Electrochem. Solid-State Lett.* **2004**, *7*, A435, doi:10.1149/1.1798151.

Chapter 2

PROCESS AND CHARACTERIZATION OF 3D ARCHITECTED PYROLYTIC CARBON ELECTRODES

Chapter Abstract

Multiscale control capabilities of a porous electrode structure enable us to create optimal electrode structures for Li to transport within an electrode at the micrometer-scale and within an electrolyte at the millimeter-scale, as discussed in Chapter 1. We developed a simple technique to fabricate 3D architected carbon electrodes with flexible micrometer-to-centimeter form-factors by combining digital light processing (DLP) 3D printing with post-exposure pyrolysis. X-ray diffraction (XRD), energy dispersed spectroscopy (EDS), Raman spectroscopy, and transmitted electron microscope (TEM) showed that the 3D pyrolytic carbon was disordered graphitic carbon composed of several stacked graphitic layers. Uniaxial compression tests using 3D architected carbon with a relative density of 0.1 revealed its mechanical resilience, as manifested by a maximum collapse strength of 27 MPa.

This chapter has been adapted from:

Narita, K.; Citrin, M.A.; Yang, H.; Xia, X.; Greer, J.R. 3D architected carbon electrodes for energy storage. *Adv. Energy Mater.* 2021, 11, 1–13, doi:10.1002/aenm.202002637.

Contributions: K.N. designed and fabricated samples, performed and analyzed the experiments, and wrote the manuscript.

2.1. Introduction: Pyrolysis with Additive Manufacturing

Pyrolysis is a thermal decomposition process of materials at elevated temperatures in an inert atmosphere. Figure 2.1 illustrates the overview of the pyrolysis process of organic materials [1]. Organic materials can be converted into carbonaceous materials by releasing hydrocarbon and foreign atoms as gas at temperatures up to 800 °C [2]. The residues may experience a liquid phase depending on precursor materials. Above 800 °C, the concentration of foreign atoms decreases in carbon materials by polycondensation with H_2 gas evolution; heat treatment at higher temperatures leads to a realignment of graphitic layers or graphitization, the degree of which is influenced by boding states of foreign atoms in the carbonaceous solid [3]. These processes, the final microstructure, and composition may vary depending on precursor materials [4] and pyrolysis conditions such as temperatures and atmospheres [5,6].

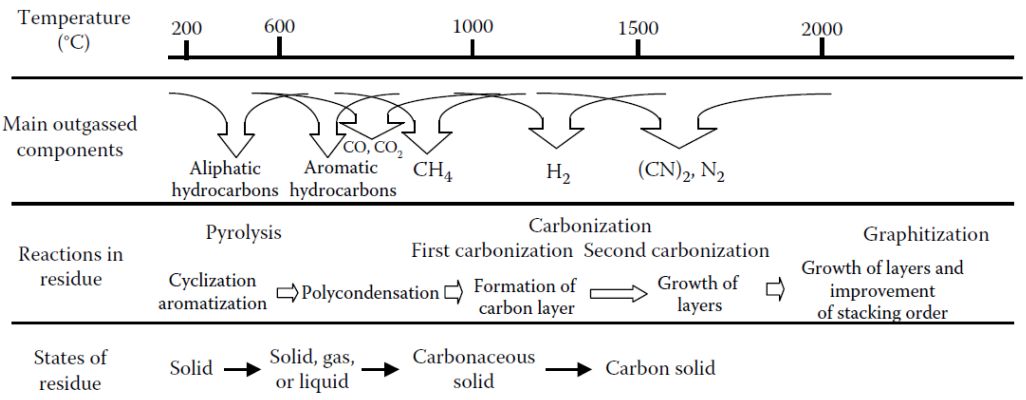

Figure 2. 1 Pyrolysis process of solid organic materials. Adapted from [1].

Manufacturing pyrolytic carbon with prescribed architecture was proposed by Prof. G. M. Whitesides and his group for micro-electromechanical system (MEMS) applications in 1997 [7]. Glassy carbon arrays were developed by pyrolyzing phenol-formaldehyde resins which are micro-molded in a patterned poly(dimethylsiloxane) (PDMS) [7]. A decade after their development, patterned pyrolytic carbon started receiving attention with the help of growing additive manufacturing technologies. Prescribed pyrolytic pillars and 3D periodic structures were manufactured by combining pyrolysis and various lithography-based techniques,

including interference lithography [8–10], self-propagating wave-guided additive manufacturing [11], stereolithography [12,13], and two-photon lithography [14,15]. The carbon architecture was studied for its mechanical resilience [14–16], and has found use in neural microsensors [17], for micro/nano-electromechanical system (MEMS/NEMS) applications [18], and as catalytic supports [19], but the carbon architecture has not been demonstrated as a battery electrode.

In this chapter, we introduce a method to fabricate 3D architected carbon for energy storage with independently controlled micron-to-centimeter form-factors, using lithography-based 3D printing of a commercial photocurable resin and post-exposure pyrolysis. In addition, we demonstrate characterizations of the 3D architected carbon for microstructure and mechanical behaviors.

2.2. Process of 3D Architected Pyrolytic Carbon Electrodes

Figure 2. 2 illustrates the fabrication processes and images of the fabricated 3D architected carbon. The structure was designed using 3D computer-aided design (CAD) software (Figure 2. 2a) and printed using a digital light processing (DLP) 3D printer (Figure 2. 2b). In the DLP 3D-printing process, an acrylate-based resin (PR-48, formulation is shown in Figure 2. 3 and Detailed Experimental Procedures) is patterned in a layer-by-layer manner by projected ultraviolet light to build the CAD-designed structure. The printed samples were rinsed with isopropanol to remove the uncured resin, dried, and then pyrolyzed in an alumina boat inside a tube furnace under vacuum at 1000°C for 4 hours following heating steps at 300°C and 400°C (See Experimental Section for more details on the pyrolysis process). Thermogravimetric analysis (TGA) revealed that resin decomposition initiated at 300°C followed by a rapid 78 wt. % decrease at ~400°C, to arrive at complete carbonization at ~650°C (Figure 2. 4). The sequential heating steps at 300°C and 400°C were prescribed to avoid trapping gas bubbles inside the structure during decomposition and shrinkage. Figure 2. 2d-f shows optical and SEM images of a typical sample before and after pyrolysis, which indicate clear isotropic shrinkage by a factor of ~3. The insets in the SEM images of 3D polymer architecture (Figure 2. 2e) and of its carbon replica (Figure 2. 2f) show top view of the same architecture to convey the straight, non-tortuous, through-sample pores.

Representative architected carbon samples used for chemical and mechanical characterization were disc-shaped, with a diameter of 1.1 cm and a thickness of 1 mm, comprised of a 45° tilted square lattice with 166 μm-wide unit cells and 28 μm-diameter beams, and had a relative density of 10% (i.e. 90% porous). We chose the same unit cell architecture (Figure 2. 2a, inset) whose all beams have a consistent angle (45°) to the printing direction and are printed in consistent printing conditions, to survey the effect of different structural parameters, like sample thickness and beam diameter, on battery performance. This fabrication approach is capable of creating a wide variety of arbitrary 3D architectures out of carbon and is not limited to periodicity: for example, a cubic-unit cell (Figure 2. 2g) and a lotus flower (Figure 2. 2h).

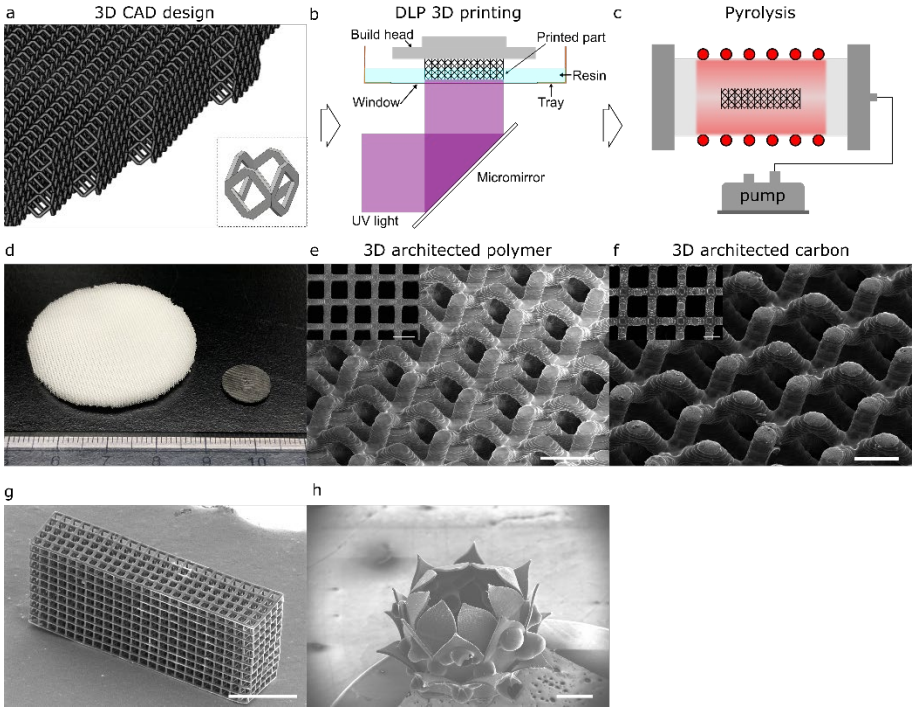

Figure 2. 2 Fabrication and images of 3D architected carbon. (a) 3D computer-aided design (CAD) of a periodic 3D lattice, with unit cell shown in the inset. Schematics of (b) Digital light processing (DLP) 3D printing process and (c) post-patterning pyrolysis. (d) A photograph of a typical as-fabricated 3D architected polymer and its post-pyrolysis carbon replica, consistently shrunk isotropically by a factor of ~3. Scanning electron microscope (SEM) images of (e) the same samples as shown in d as-fabricated 3D architected polymer and (f) its architected carbon replica. Insets in (e) and (f): zoomed-in top views of the electrodes with straight beams and pores. Arbitrary 3D architecture can be created out of carbon such as (g) periodic structure composed of a cubic-unit cell and (h) lotus flower-like structure. Scale bars are 500 μm for (e) and inset of (e), 100 μm for (f) and inset of (f), 1 mm for (g) and (h).

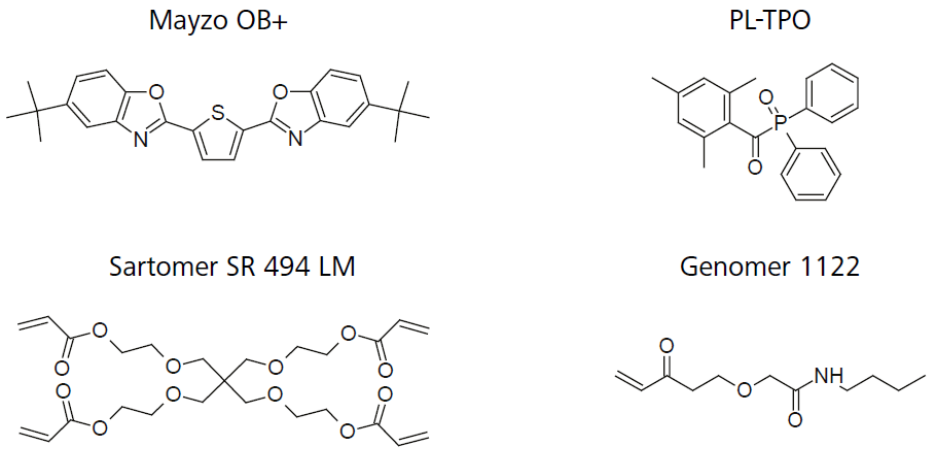

Figure 2. 3 Structural formulations of components in PR48 photocurable resin.

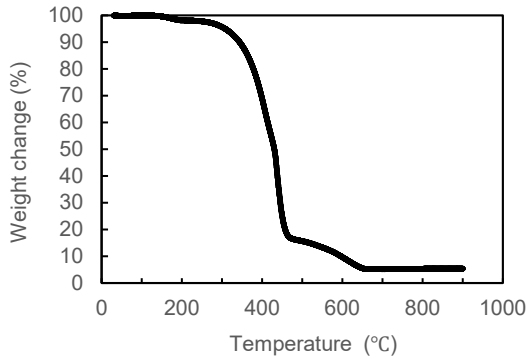

Figure 2. 4 Thermogravimetric analysis (TGA) of acryl-based photoresin under a N_2 flow.

2.3. Microstructural Characterization of 3D Architected Pyrolytic Carbon

Figure 2. 5 contains microstructural and chemical characterization of the 3D architected carbon. SEM image of a typical beam cross section demonstrates its monolithic, pore-less morphology (Figure 2. 5a) and smooth outer surfaces (Figure 2. 5b). EDS analysis (Figure 2. 5a, inset) of the same surface shows an average composition of 98.4 at. % carbon with 1.6 at. % oxygen, homogeneously distributed through the beam (Figure 2. 5c). To uncover the atomic-level microstructure of pyrolytic carbon, we fragmented the samples using a razor blade and ground it into powder using glass slides. Figure 2. 5d shows high-resolution TEM

(HRTEM) image and reveals the microstructure to be mostly composed of several differently oriented graphitic layers separated by 3.63 Å (lower inset). The diffraction pattern in the upper inset of Figure 2. 5e shows diffused diffraction rings of (002), (100), and (110) characteristic of graphite.

Figure 2. 5f shows a typical X-ray Diffraction (XRD) spectrum of pyrolytic carbon that contains three broad peaks at 2θ = 23.5°, 44.3°, and 79.8°, which correspond to (002), (100), and (110) diffractions. A reference XRD spectrum for graphite is also provided for comparison [20]. The presence of these broad peaks indicates that pyrolytic carbon contains turbostratic graphene layers [21]. This spectrum reveals the average interlayer spacing between graphene segments along (002) direction, d_{002}, to be 3.78 Å, according to Bragg's law, $2d\ sin\theta = \lambda$, where d is the interlayer spacing, θ is the diffraction angle, and λ is the wavelength of incident beam. This is 12.5% greater than that of graphite, 3.36 Å, shown as reference. From the (002) peak, we determined the crystallite size along (002) direction, L_c to be 9.4 Å using Scherrer equation, $L = K\lambda/Bcos\theta$, where K is the Scherrer constant (K=0.9), and B is the full width at half maximum of the diffraction peak , measured in 2θ, and θ is the peak position [22]. These findings suggest that a crystallite is composed of several stacked graphitic layers that are separated, on average, by 3.78 Å. Figure 2. 5g shows Raman spectra obtained from the surface of 3D architected carbon. We deconvoluted the Raman spectra into five peaks: strong peaks of D1 (at 1355 cm^{-1}) and G (at 1603 cm^{-1}) and weak peaks of D2 (at 1613 cm^{-1}), D3 (at 1539 cm^{-1}), and D4 (1225 cm^{-1}). The G peak corresponds to the in-plane bond-stretching motion of pairs of sp^2-carbon atoms with E_{2g} symmetry [23]. The D1 peak appears only in the presence of lattice disorder and corresponds to a graphitic lattice vibration mode with A_{1g} symmetry [23]. We attributed the D2 peak to graphitic lattice vibrations, and the D3 and D4 peaks to amorphous or glassy carbon, consistent with literature [24,25]. The Brunauer−Emmett−Teller (BET) specific surface area was measured and found to be 15.2 $m^2\ g^{-1}$.

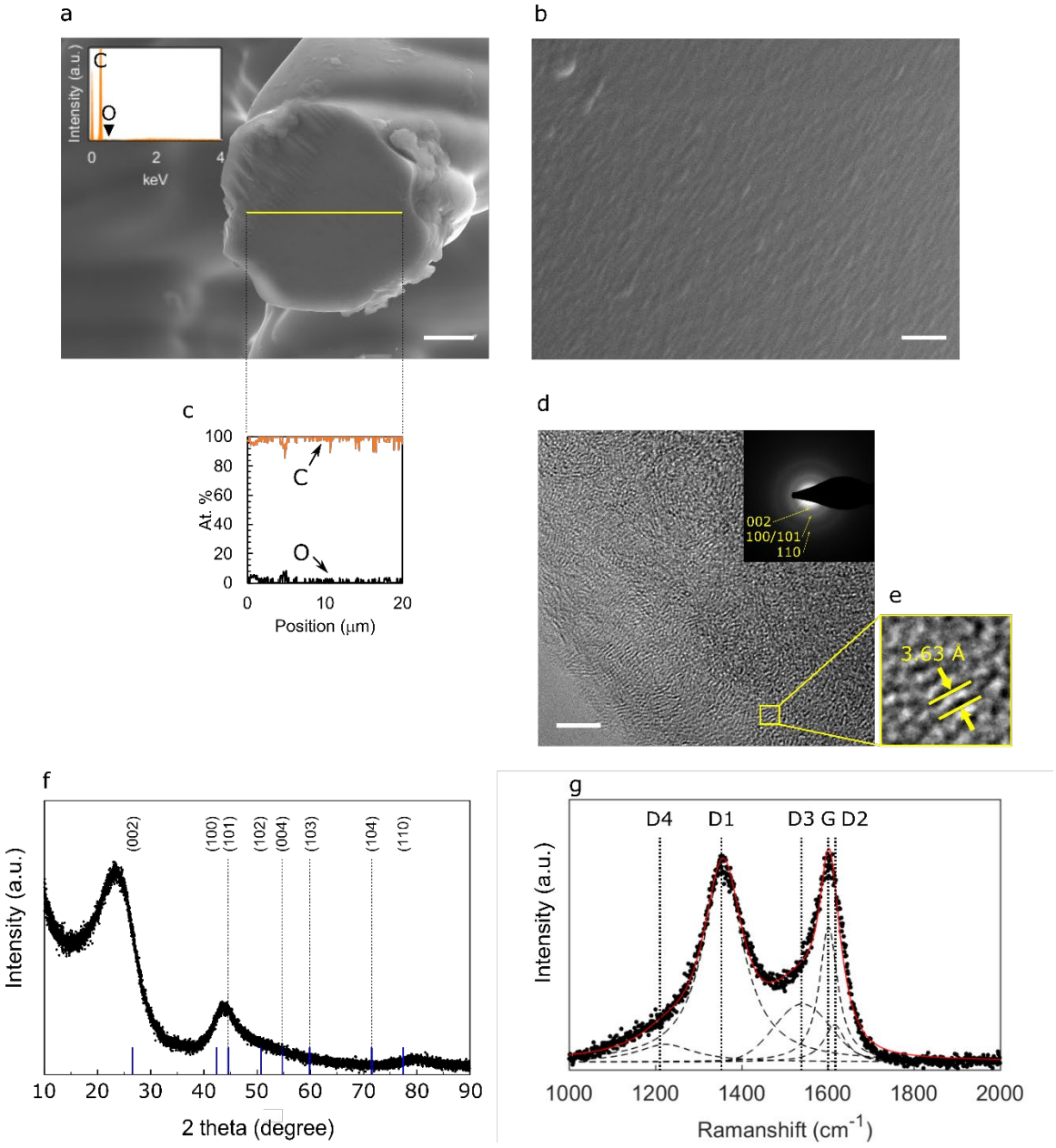

Figure 2. 5 Microstructural and chemical characterization of 3D architected carbon. (a) SEM image of cross-section and energy dispersive spectroscopy (EDS) spectrum on the cross-section. (b) High magnification of SEM image of the 3D architected carbon showing smooth surface. (c) Line analysis of EDS on the cross-section. (d) High resolution transmitted electron microscope (HRTEM) image and diffraction pattern (inset). (e) Magnified image of (d) showing several stacked layers. (f) X-ray diffraction (XRD) pattern and (g) Raman spectrum with experimental data (●), fitted curves for each band (dot lines), and the linear combination of these bands (red line). Scale bars are 5 μm for (a), 100 nm for (b), and 5 nm in (d).

2.4. Mechanical Behaviors of 3D Architected Pyrolytic Carbon

We investigated the mechanical behavior of architected carbon by conducting uniaxial compression experiments with simultaneous video frames capture. These experiments revealed that the deformation occurred via a series of half-layer brittle collapse events, interspersed with the combination of linear and quadratic loading segments, as classified by regions I-IV (Figure 2.6). Figure 2.6a shows a representative mechanical response under load, marking specific events during the deformation that are shown in Figure 2.6c (full movie is provided in the Supporting Information). The instantaneous stiffness was calculated as a ratio of infinitesimal changes in applied load and measured displacement using mean values of 3 adjacent data points.

Mechanical data reveals that the initial slightly imperfect contact, caused by structural imperfections from the 3D printing process, was succeeded by a quadratic load increase and a concomitant linear stiffness increase, indicative of establishing full contact, until the displacement of ~55 μm, at which the first brittle local collapse event occurred. The successive local collapse events were characterized by a load removal over ~20 μm (region I). The video frame captured during this collapse in Figure 2.6c-2 reveals several gaps and voids that formed mostly at the sample/substrate. Region II commenced after the first collapse events, with the contact re-established at a displacement of 75 μm, followed by another linear stiffness increase and load decrease segment until the displacement of 95 μm. Linear loading commenced thereafter and transitioned into quadratic at a displacement of 115 μm, followed by a brittle half-layer collapse, which occurred at a displacement of ~140 μm. The slopes of linear stiffness change before and after the constant stiffness section in region II where they were self-consistent (~1.7 MN/mm^2), as depicted by green slope markers in Fig. 3b. After the second collapse, the 3D architected carbon started re-establishing contact with the substrate, indicated by a linear stiffness increase until the highest stiffness of 51 kN/mm, which corresponds to 520 MPa over ~40 μm displacement until it sustained the maximum precollapse load of 2.7 kN, which corresponds to 30 MPa axial stress (region III). Figure 2.6c-3 and c-4 captures the images before and after the collapse with the maximum load. The subsequent analogous half-layer collapse at a

displacement of 320 μm occurred in region IV with the same stiffness change as shown by red slope markers in Fig. 3b. This layer-by-layer collapse signature was observed in all deformed samples (Figure 2. 7). The average maximum stresses before each collapse are tabulated in Table 2. 1.

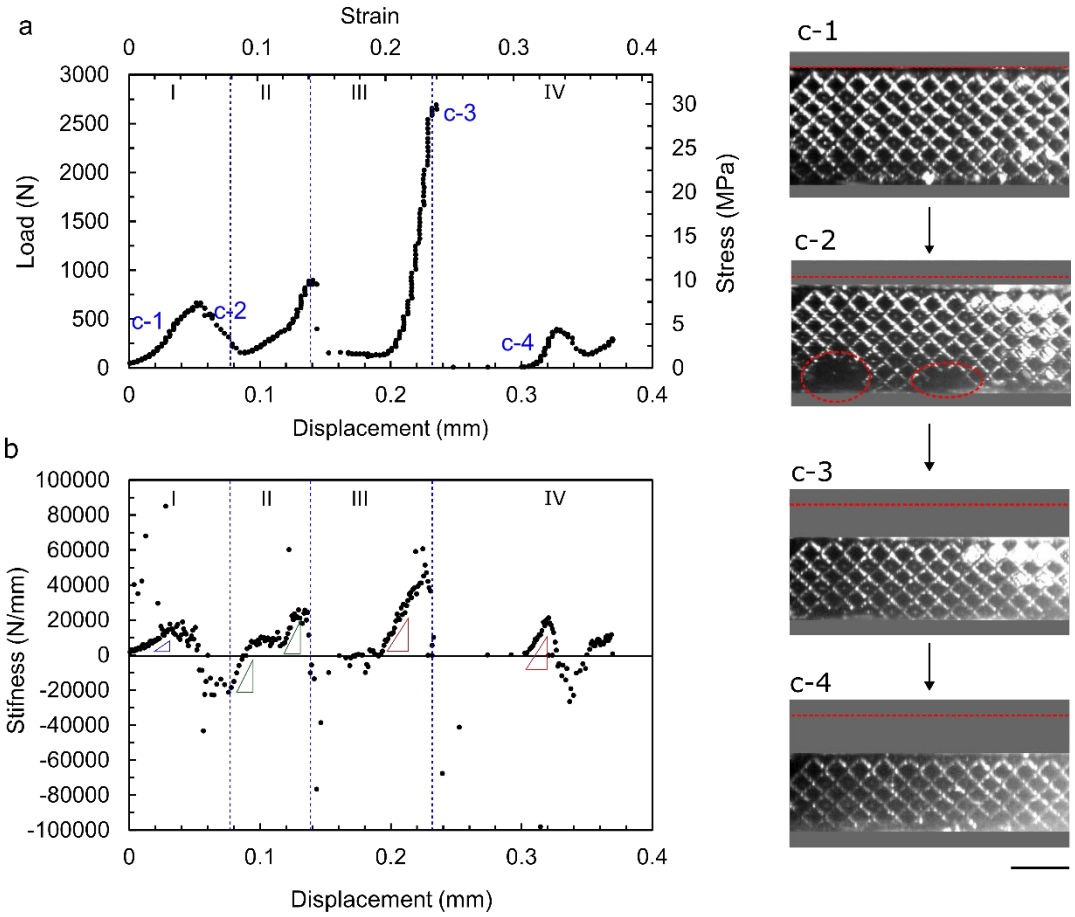

Figure 2.6 Compression test results of 3D architected carbon. (a) Load-displacement curve and (b) stiffness-displacement curve of 3D architected carbon. Different deformation behaviors are classified by regions I to III. Triangles guide the linear stiffness increase sections. (c-1)~(c-4) the side view-images at events marked in (a) and (b). Substrate and top load cell were grayed out. Scale bar is 500 μm for (c-1)~(c-4).

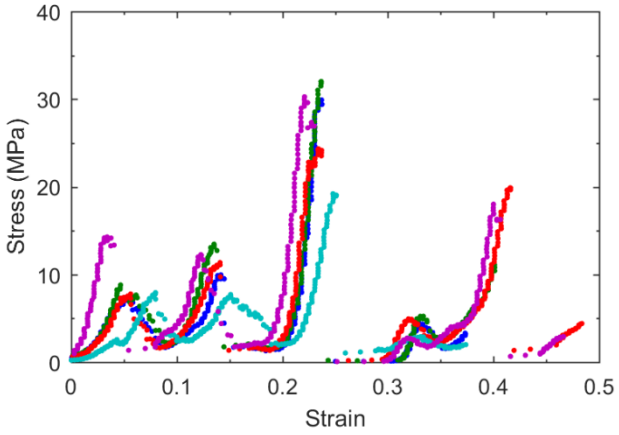

Figure 2. 7 Stress-strain curves of five samples of the 3D architected carbon.

Table 2. 1 Average values and standard deviations (SD) of the 1st, 2nd, and 3rd collapse stress.

	1st collapse	2nd collapse	3rd collapse
Average (MPa)	9.2	14.2	27.1
SD (MPa)	2.9	6.4	5.3

2.5. Carbonization of 3D Printed Polymer by Pyrolysis

We demonstrate that a combination of DLP 3D printing and pyrolysis realizes a fabrication process that accesses multiple length scales and more flexible form-factors than other methods of structural engineering, especially for device applications. The DLP 3D printing enables scaling up free-standing architected polymers up to centimeter length scales, with a resolution of several hundred microns (Figure 2. 2a and e). The post-patterning pyrolysis step converts the polymer into monolithic glassy carbon, with a concomitant 3x linear isotropic shrinkage (see cross-section in Figure 2. 5a) [7,16,26]. Compared with some other photolithography-based techniques, to which post-patterning pyrolysis presents a challenge, this process requires simple steps for creating architected carbon with controlled form-factors. For example, two-photon lithography and stereolithography require the sample to be attached to a substrate during pyrolysis, which poses significant challenges for preserving shape integrity during shrinkage; photolithography [27] and interferometric lithography [10] are limited by the mask patterns; the common photocurable polymers, such as SU-8 lose

structural integrity by softening during pyrolysis [9]. The described combination of DLP 3D printing and pyrolysis overcome these limitations and enhance the structural electrode parameter space to include a broad range of form factors, shapes, and dimensions that may not be accessible with other techniques (Figure 2. 2).

2.6. Structural Integrity of the 3D Architected Carbon

Uniaxial compression experiments demonstrate that structured carbon electrodes deformed via layer-by-layer collapse, attaining the highest average stress of 27.1 MPa, higher than previously reported values of carbon lattices at a similar relative density: 24.80 MPa for octet-lattice with 16% relative density and 3.9-10.2 MPa for Octrahedral-type microlattice with 12.8 % relative density [11,28]. We calculated the specific strength of architected carbon, defined as the ratio of maximum precollapse stress and lattice density, to be 101 kN m kg^{-1}, a value comparable to that of the 6061 aluminum alloy used in aircrafts [29] and of novel battery electrodes developed for structural multifunctional batteries [30]. Thomas and Qidwai reported that load-bearing structure and battery components occupy 20-40% of the total weight in unmanned airborne vehicles (UAVs), and proposed that decreases in those weights are 1.5 times more effective for increasing endurance time than increases in the stored battery energy density [31]. This suggests that architected pyrolytic carbon electrodes can be used as multifunctional materials that simultaneously provide superior energy storage and load-bearing capabilities in UAVs. The mechanical properties of 3D-sculpted materials can be further improved by optimizing their architecture [15]. The observed maximum initial precollapse stress of 9 MPa is higher than the static pressure of 0.1-1 MPa typically reported for packaged cells [32], which renders it resilient in packaged cells. This is consistent with our observations that the morphology and shape integrity of architected carbon was preserved after 500 galvanostatic cycles at 100 mA g^{-1}, which is discussed in Chapter 3. This mechanical resilience brings about the advantage of this process over other methods of electrode engineering that may require protection via dedicated packaging to avoid posing direct pressure on the battery electrodes [33–36].

2.7. Summary

We used commercially available DLP 3D printing and post-exposure pyrolysis to develop a facile and scalable method to fabricate 3D architected carbon electrodes with flexible micron-to-centimeter form-factors. The pyrolysis step converts the polymer into monolithic pyrolytic carbon, with a concomitant 3x linear isotropic shrinkage. Microstructural characterization indicates that the microstructure of pyrolytic carbon is disordered graphitic carbon composed of several stacked graphitic layers. The fabricated free-standing architected carbon exhibits great structural integrity, manifested by sustaining compressive stress of 27 MPa, which suggests that architected pyrolytic carbon electrodes can be used as multifunctional materials that simultaneously provide superior energy storage and load-bearing capabilities.

2.8. Detailed Experimental Procedures

Fabrication of the 3D architected polymer and carbon

The architecture was prescribed by a computer-aided design program (Solidworks, Dassault Systems) and printed by a commercial digital light processing (DLP) 3D printer (Ember, Autodesk) using commercial acryl-based photocurable resin (PR-48, Colorado photopolymer solutions). PR-48 resin is composed of 39.776 wt. % Allnex Ebecryl 8210 and 39.776 wt.% Sartomer SR 494 as oligomers, 0.400 wt. % Esstech TPO+ (2,4,6-Trimethylbenzoyl-diphenylphosphine oxide) as photoinitiator, 19.888 wt. % Rahn Genomer 1122 as a reactive diluent, and 0.160 wt. % Mayzo OB+ (2,2'-(2,5-thiophenediyl)bis(5-tertbutylbenzoxazole)) as UV blocker. In the DLP 3D printer, a 2D digital pattern was irradiated by UV light through a glass window and cured on a build head or the previous layer, and the 3D architecture was printed in a layer-by-layer manner as the build head rose (Figure 2. 2b). The layer thickness was 25 μm, and the one-pixel size of the 2D digital pattern corresponded to 50 × 50 μm. The printing time, which depends on the number of printing layers for the DLP printing, exposure time, and other parameters, was a half-hour for the 3D architected polymer with 3 mm tall. After removing the printed object from the build head, the printed object was rinsed with isopropanol and dried. Then, the printed object on an alumina boat was pyrolyzed by a tube furnace (OTL-1500X-UL, MTI). The heating process

started after reaching the pressure below 100 mTorr, and the step heating processes were employed at 300°C for 4 hours, 400°C for 1 hour, and 1000°C for 4 hours at a heating rate of 5°C/min. Then, the furnace was cooled down at 5°C/min up to around 300°C and at a natural cooling rate up to room temperatures. The specimens were weighed by an analytical balance (XS105, Mettler Toledo) and measured for diameter and thickness by a caliper. Lattice density was calculated by dividing mass by volume, including void spaces using the measured diameter and thickness. The apparent densities were used to calculate the relative density and specific strength of electrodes. Some of the 3D printed polymer samples were etched using O_2 plasma asher (Zepto B, Diener electronic) for 6 hours and pyrolyzed in the conditions as described above.

Characterizations of the 3D architected polymer and carbon

Thermogravimetry (TG) analysis (STA 6000, PerkinElmer) was conducted for the 3D architected polymer in a 99.999 % nitrogen flow at 20 ml /min at a heating rate of 5°C/min. The morphology of the 3D architecture was observed by scanning electron microscope (Versa 3D Dual Beam, FEI). A specimen of the 3D architected carbon was cut by a razor blade and the cross-section was analyzed by a field emission SEM (ZEISS 1550 VP) equipped with energy-dispersive spectroscopy (Oxford X-max SDD). The 3D architected carbon was crushed into powder using a mortar and pestle for X-ray diffraction analysis (X'Pert, Philips) to investigate the crystal structure. Cu Kα radiation (1.54 Å) was used at 45 kV and 40 mA. The L_c parameter was calculated using Scherrer's equation with the values of K = 0.89. The carbon microstructure was analyzed by Raman spectroscopy (M-1000, Renishaw) using a laser at the wavelength of 514 nm on the flat surface of the 3D architected carbon. More than three different spots were obtained, and the spectrum closest to their average was chosen as a representative. A transmission electron microscope (TEM, Tecnai F30ST, FEI) was conducted for high-resolution imaging and obtaining diffraction patterns. The sample was prepared by breaking the 3D architected carbon into particles and ground them with glass slides. The particles bridged on the hole of a sample holder were observed to avoid obtaining information from the amorphous carbon substrate. Nitrogen isotherms

were measured at 77 K, and surface areas were calculated using the Brunauer-Emmett-Teller (BET) method.

Compression test

Uniaxial compression tests for five specimens were conducted using a materials testing machine (Instron 5569) with a laser extensometer (LE-01, Electronic Instrument Research) for obtaining displacement and a CMOS camera (Aptina MT9VV022, FLIR) for simultaneous video frames capture. The side of 3D architected carbon which had beam imperfections was placed on the bottom. The strain rate was 0.15 mm/min. Load and displacement data were acquired every 0.5 seconds. The top cross-head and substrate were grayed out to clarify the sample position from them because lattice morphology was reflected on the cross-head and substrate. A full movie with the trajectory of stress-strain curves is available in the Supporting Information.

REFERENCES

1. Inagaki, M. Structure and texture of carbon materials. In *Carbons for Electrochemical Energy Storage and Conversion Systems*; 2009; pp. 37–76.

2. Tang, M..; Bacon, R. Carbonization of cellulose fibers—I. Low temperature pyrolysis. *Carbon N. Y.* **1964**, *2*, 211–220, doi:10.1016/0008-6223(64)90035-1.

3. Gladkova, L.G.; Kolpikova, E.F.; Vygodskii, Y.S.; Fialkov, A.S. Specific pyrolysis of polycondensation polymers. *Russ. Chem. Rev.* **1988**, *57*, 999–1011, doi:10.1070/rc1988v057n10abeh003407.

4. Franklin, R.E. Crystallite growth in graphitizing and non-graphitizing carbons. *Proc. R. Soc. A Math. Phys. Eng. Sci.* **1951**, *209*, 196–218, doi:10.1098/rspa.1951.0197.

5. Kiyono, M.; Williams, P.J.; Koros, W.J. Effect of pyrolysis atmosphere on separation performance of carbon molecular sieve membranes. *J. Memb. Sci.* **2010**, *359*, 2–10, doi:10.1016/j.memsci.2009.10.019.

6. Luo, W.; Wang, B.; Heron, C.G.; Allen, M.J.; Morre, J.; Maier, C.S.; Stickle, W.F.; Ji, X. Pyrolysis of cellulose under ammonia leads to nitrogen-doped nanoporous carbon generated through methane formation. *Nano Lett.* **2014**, *14*, 2225–2229, doi:10.1021/nl500859p.

7. Schueller, O.J.A.; Brittain, S.T.; Whitesides, G.M. Fabrication of glassy carbon microstructures by pyrolysis of microfabricated polymeric precursors. *Adv. Mater.* **1997**, *9*, 477–480, doi:10.1002/adma.19970090604.

8. Xiao, X.; Beechem, T.E.; Brumbach, M.T.; Lambert, T.N.; Davis, D.J.; Michael, J.R.; Washburn, C.M.; Wang, J.; Brozik, S.M.; Wheeler, D.R.; et al. Lithographically defined three-dimensional graphene structures. *ACS Nano* **2012**, *6*, 3573–3579,

doi:10.1021/nn300655c.

9. Jin, W.M.; Moon, J.H. Supported pyrolysis for lithographically defined 3D carbon microstructures. *J. Mater. Chem.* **2011**, *21*, 14456–14460, doi:10.1039/c1jm10599j.

10. Spoerke, E.D.; Polsky, R.; Burckel, D.B.; Wheeler, D.R.; Bunker, B.C. Rapid thermal pyrolysis of interferometrically patterned resist. *Carbon N. Y.* **2012**, *50*, 2894–2898, doi:10.1016/j.carbon.2012.02.058.

11. Jacobsen, A.J.; Mahoney, S.; Carter, W.B.; Nutt, S. Vitreous carbon micro-lattice structures. *Carbon N. Y.* **2011**, *49*, 1025–1032, doi:10.1016/j.carbon.2010.10.059.

12. Chen, X.; Zhao, G.; Wu, Y.; Huang, Y.; Liu, Y.; He, J.; Wang, L.; Lian, Q.; Li, D. Cellular carbon microstructures developed by using stereolithography. *Carbon N. Y.* **2017**, *123*, 34–44, doi:10.1016/j.carbon.2017.07.043.

13. Rezaei, B.; Pan, J.Y.; Gundlach, C.; Keller, S.S. Highly structured 3D pyrolytic carbon electrodes derived from additive manufacturing technology. *Mater. Des.* **2020**, *193*, 108834, doi:10.1016/j.matdes.2020.108834.

14. Crook, C.; Bauer, J.; Guell Izard, A.; Santos de Oliveira, C.; Martins de Souza e Silva, J.; Berger, J.B.; Valdevit, L. Plate-nanolattices at the theoretical limit of stiffness and strength. *Nat. Commun.* **2020**, *11*, 1–11, doi:10.1038/s41467-020-15434-2.

15. Bauer, J.; Schroer, A.; Schwaiger, R.; Kraft, O. Approaching theoretical strength in glassy carbon nanolattices. *Nat. Mater.* **2016**, *15*, 438–443, doi:10.1038/nmat4561.

16. Zhang, X.; Vyatskikh, A.; Gao, H.; Greer, J.R.; Li, X. Lightweight, flaw-tolerant, and ultrastrong nanoarchitected carbon. *Proc. Natl. Acad. Sci. U. S. A.* **2019**, *116*, 6665–6672, doi:10.1073/pnas.1817309116.

17. Yang, C.; Cao, Q.; Puthongkham, P.; Lee, S.T.; Ganesana, M.; Lavrik, N. V.; Venton, B.J. 3D-Printed carbon electrodes for neurotransmitter detection. *Angew. Chemie* -

Int. Ed. **2018**, *57*, 14255–14259, doi:10.1002/anie.201809992.

18. Jiang, S.; Shi, T.; Zhan, X.; Xi, S.; Long, H.; Gong, B.; Li, J.; Cheng, S.; Huang, Y.; Tang, Z. Scalable fabrication of carbon-based MEMS/NEMS and their applications: A review. *J. Micromechanics Microengineering* **2015**, *25*, doi:10.1088/0960-1317/25/11/113001.

19. Burckel, D.B.; Washburn, C.M.; Raub, A.K.; Brueck, S.R.J.; Wheeler, D.R.; Brozik, S.M.; Polsky, R. Lithographically defined porous carbon electrodes. *Small* **2009**, *5*, 2792–2796, doi:10.1002/smll.200901084.

20. Trucano, P.; Chen, R. Structure of graphite by neutron diffraction. *Nature* **1975**, *258*, 136–137, doi:10.1038/258136a0.

21. Li, Z.Q.; Lu, C.J.; Xia, Z.P.; Zhou, Y.; Luo, Z. X-ray diffraction patterns of graphite and turbostratic carbon. *Carbon N. Y.* **2007**, *45*, 1686–1695, doi:10.1016/j.carbon.2007.03.038.

22. Tasco, J.M.D.; Cuesta, A.; Dhamelincourt, P.; Laureyns, J. Comparative performance of X-ray diffraction and Raman microprobe techniques for the study of carbon materials. **1998**, 2875–2879.

23. Ferrari, A.C.; Robertson, J. Interpretation of Raman spectra of disordered and amorphous carbon. *Phys. Rev. B* **2000**, *61*, 14095–14107, doi:10.1103/PhysRevB.61.14095.

24. Pawlyta, M.; Rouzaud, J.N.; Duber, S. Raman microspectroscopy characterization of carbon blacks: Spectral analysis and structural information. *Carbon N. Y.* **2015**, *84*, 479–490, doi:10.1016/j.carbon.2014.12.030.

25. Sadezky, A.; Muckenhuber, H.; Grothe, H.; Niessner, R.; Pöschl, U. Raman microspectroscopy of soot and related carbonaceous materials: Spectral analysis and structural information. *Carbon N. Y.* **2005**, *43*, 1731–1742, doi:10.1016/j.carbon.2005.02.018.

26. Zhang, X.; Zhong, L.; Mateos, A.; Kudo, A.; Vyatskikh, A.; Gao, H.; Greer, J.R.; Li,

X. Theoretical strength and rubber-like behaviour in micro-sized pyrolytic carbon. *Nat. Nanotechnol.* **2019**, *14*, 762–769, doi:10.1038/s41565-019-0486-y.

27. Wang, C.; Taherabadi, L.; Jia, G.; Madou, M.; Yeh, Y.; Dunn, B. C-MEMS for the manufacture of 3D microbatteries. *Electrochem. Solid-State Lett.* **2004**, *7*, A435, doi:10.1149/1.1798151.

28. Kudo, A.; Misseroni, D.; Wei, Y.; Bosi, F. Compressive response of non-slender octet carbon microlattices. *Front. Mater.* **2019**, *6*, 1–12, doi:10.3389/fmats.2019.00169.

29. Davis, J.R. Light metals and alloys-aluminum and aluminum alloys. *Alloy. Underst. Basics* **2001**, 351–416, doi:10.1361/autb2001p351.

30. Evanoff, K.; Benson, J.; Schauer, M.; Kovalenko, I.; Lashmore, D.; Ready, W.J.; Yushin, G. Ultra strong silicon-coated carbon nanotube nonwoven fabric as a multifunctional lithium-ion battery anode. *ACS Nano* **2012**, *6*, 9837–9845, doi:10.1021/nn303393p.

31. Thomas, J.P.; Qidwai, M.A. The design and application of multifunctional structure-battery materials systems. *JOM* **2005**, *57*, 18–24, doi:10.1007/s11837-005-0228-5.

32. Cannarella, J.; Arnold, C.B. Stress evolution and capacity fade in constrained lithium-ion pouch cells. *J. Power Sources* **2014**, *245*, 745–751, doi:10.1016/j.jpowsour.2013.06.165.

33. Jiang, J.J.; Gasik, M.; Laine, J.; Lampinen, M. Electrochemical evaluation of sintered metal hydride electrodes for electric vehicle applications. *J. Alloys Compd.* **2001**, *322*, 281–285, doi:10.1016/S0925-8388(01)01257-9.

34. Lai, W.; Erdonmez, C.K.; Marinis, T.F.; Bjune, C.K.; Dudney, N.J.; Xu, F.; Wartena, R.; Chiang, Y.M. Ultrahigh-energy-density microbatteries enabled by new electrode architecture and micropackaging design. *Adv. Mater.* **2010**, *22*, 139–144, doi:10.1002/adma.200903650.

35. Billaud, J.; Bouville, F.; Magrini, T.; Villevieille, C.; Studart, A.R. Magnetically aligned graphite electrodes for high-rate performance Li-ion batteries. *Nat. Energy* **2016**, *1*, 1–6, doi:10.1038/nenergy.2016.97.

36. Saleh, M.S.; Li, J.; Park, J.; Panat, R. 3D printed hierarchically-porous microlattice electrode materials for exceptionally high specific capacity and areal capacity lithium ion batteries. *Addit. Manuf.* **2018**, *23*, 70–78, doi:10.1016/j.addma.2018.07.006.

Chapter 3

BATTERY DEMONSTRATION OF 3D ARCHITECTED CARBON ELECTRODES

Chapter Abstract

Successfully developed 3D architected carbon electrodes are demonstrated as Li-ion battery electrodes in this chapter. Galvanostatic cycling tests at 2 mAg^{-1} using a half-cell of 3D carbon electrodes and Li meatal with an electrolyte of $LiPF_6$ in EC: DEC show abrupt voltage change from 2.0 V to 1.0 V, and a gradual change up to 0.1 V and a shift to a plateau at lower voltages. The reversible capacity of the 3D architected carbon with ~23 mg cm^{-2} of a mass loading was ~230 mAh g^{-1} (7 mAh cm^{-2}) at 16 mA g^{-1} and 43 mAh g^{-1} (1.3 mAh cm^{-2}) at 300 mA g^{-1}. A long cycling test at 100mA g^{-1} (2.4 mA cm^{-2}) revealed the capacity of 3D architected carbon retained from 3.2 mAh cm^{-2} with a gradual decrease up to around 1 mAh cm^{-2} over 500 cycles. The cycled electrode showed preserved architecture, and the rinsing process of the electrodes recovered their capacity up to 2.6 mAh cm^{-2}. Overall, galvanostatic cycling using the 3D architected carbon electrodes exhibited typical discharge and charge behaviors of hard carbon, and demonstrated structural integrity, enabling a systematic study of the relationship between electrode architecture and battery performance.

This chapter has been adapted from:

Narita, K.; Citrin, M.A.; Yang, H.; Xia, X.; Greer, J.R. 3D architected carbon electrodes for energy storage. *Adv. Energy Mater.* 2021, 11, 1–13, doi:10.1002/aenm.202002637.

Contributions: K.N. designed and fabricated samples, performed and analyzed the experiments, and wrote the manuscript.

3.1. Introduction: Pyrolytic carbon as an Anode Material for a Lithium-Ion Battery

Pyrolytic carbon is categorized into “graphitizable carbon” and “non-graphitizable carbon” by their crystalline growth behaviors at elevated temperatures, as proposed by Franklin in 1951 [1]. Graphitizable carbons can transform into crystalline graphite by being heated up to 3000 °C, while non-graphitizable carbons do not transform into graphite at any temperature. These types of carbon are called “soft carbon” (graphitizable carbon) and “hard carbon” (non-graphitizable carbon) in the battery community, which have been developed from the 1980s as lithium-ion battery anode materials [2–4]. Hard carbon was used as an anode material in the first commercial lithium ion batteries from Sony in 1991. Hard carbon showed stability to propylene carbonate (PC) electrolyte, which causes exfoliation for graphite electrodes by cointercalation of solvents [5,6]. Prof. J. R. Dahn showed in 1990 that ethylene carbonate (EC) electrolyte successfully forms stable SEI and desolvates Li-ions on graphite electrodes for intercalation [7], which resulted in replacing anode materials from hard carbon to graphite, a current standard anode material.

Hard carbon generates renewed scientific excitement for its potential as an anode material because of its high capacity and rate performance and is commercially used by companies such as EnerDel, Kuraray, and ATEC. Prof. Dahn and his group studied the mechanism of lithium insertion into hard carbon and showed higher capacities of hard carbon (>700 mAh/g) than the theoretical capacity of graphite (372 mAh/g) [3]. Although some debate remains in the mechanism of capacity gain of hard carbon electrodes, there are three commonly known mechanisms: 1) pseudocapacitance or carbon-edge redox reaction with surface functional groups (2-0.4 V vs Li) [8], 2) lithium insertion into nanopores surrounding differently-oriented graphene layers (< 0.4 V vs Li) [3,9], and 3) lithium intercalation into graphitic layers (< 0.2 V vs Li) [10]. These capacity gain mechanisms are associated with carbon microstructure such as surface functional groups, crystallinity size, an interlayer distance of graphene layers, controllable by pyrolysis conditions and precursor materials [5].

In this chapter, we demonstrate 3D architected pyrolytic carbon as an anode material for lithium-ion batteries, having demonstrated in Chapter 2 a successful process of 3D

architected carbon. The 3D architected pyrolytic carbon is composed of tangled carbon microstructures with several stacks of graphene layers, characteristic features of hard carbon [11]. Here, we electrochemically characterize the 3D architected carbon as hard carbon electrodes to build a foundation for discussing structural factors and their influences on rate performance (Chapter 4) and solid electrolyte interphase (Chapter 5).

3.2. Galvanostatic Cycling with 3D Architected Carbon Electrodes

To evaluate the electrochemical performance of architected carbon electrodes, we used a 2032 coin cell to assemble a half-cell with a 23.5-23.6 mg cm^{-2} mass loading of active materials against lithium metal as a counter and a reference electrode (Figure 3. 1). Figure 3. 2a-c shows the results of galvanostatic cycling of 3D architected carbon sample at different current densities. Figure 3. 2a contains the first and second discharge-charge curves of galvanostatic cycling at 2mA g^{-1}, which leads to 379 mAh g^{-1} and 367 mAh g^{-1} of reversible capacity and 78 % and 96 % of Coulombic efficiency in the first and second cycle, respectively. During the first discharge, the voltage first dropped abruptly to 0.8 V, followed by a gradual decrease to ~0.1 V and a plateau below 0.1 V. During the subsequent charge, the voltage increased without an inflection point at 0.8 V, which occurred during the first discharge. In the second cycle, the discharge and charge processes exhibited a similar hysteresis: an abrupt change up to 1.0 V, a more gradual change at lower voltages between 1.0 – 0.1 V, and a plateau below 0.1 V. Figure 3. 2b shows the discharge capacities at step currents from 16.7 mA g^{-1} (0.39 mA cm^{-2}) to 300 mA g^{-1} (7.07 mA cm^{-2}), followed by 100 cycles at 16.7 mA g^{-1}, and reveals their deterioration with current density. The Coulombic efficiencies during the first and second cycle were 71.7% and 97.8%. At each current step from 33.3 mA g^{-1}, the Coulombic efficiencies at the first cycle ranged from 91.4% to 97.7%, lower than those in the subsequent cycles (>99%). The capacity recovered from 43 mAh g^{-1} at 300 mA g^{-1} up to 260 mAh g^{-1} (6.13 mAh cm^{-2}) in the second cycle after returning to 16.7 mA g^{-1}, with >80 % capacity retained after 117 cycles, dropping to ~70% after the 130th cycle. Galvanostatic cycling in a three-electrode configuration with a separated reference lithium electrode from a lithium counter electrode was also conducted (Figure 3. 3), showing <15% difference in capacities at step currents from that of a two-electrode configured half-cell. Figure 3. 2c shows a long cycling test at 100mA g^{-1} (2.4 mA cm^{-2}) that lasted over 500

cycles after three pre-cycles at 16.7 mA g^{-1} intended to form the solid electrolyte interface (SEI). The capacities rapidly decreased from 131 mAh g^{-1} (3.2 mAh cm^{-2}) to around 98 mAh g^{-1} (2.3 mAh cm^{-2}) by 10 cycles and gradually decreased over 500 cycles. The Coulombic efficiency remained high, >99.9 % for 2nd through 500th cycles, with the first cycle 92 % at 100 mA g^{-1}.

Figure 3. 2d shows an SEM image of this 3D architected carbon electrode after >300 charge-discharge cycles at 100mA g^{-1} and conveys that the shape integrity and the prescribed architecture were preserved. The surface was covered by SEI formed during cycling (Figure 3. 4). We recycled the architected carbon electrode after 500 cycles by rinsing it with dimethyl carbonate (DMC) and water twice, drying in a vacuum oven, and assembling it in the same way in a new coin cell with a fresh electrolyte. After the three pre-cycles at 16.7 mA g^{-1}, the recycled 3D architected carbon showed the recovered capacity of up to 110 mAh g^{-1} (2.58 mAh cm^{-2}), which decreased to 80 mA g^{-1} (1.95 mAh cm^{-2}) after five cycles at 100 mA g^{-1}. The capacity then decreased gradually by 18% over subsequent 45 cycles while maintaining 99.9% of Coulombic efficiencies. All discharge-charge curves for Figure 3. 2b and c are provided in Figure 3. 5.

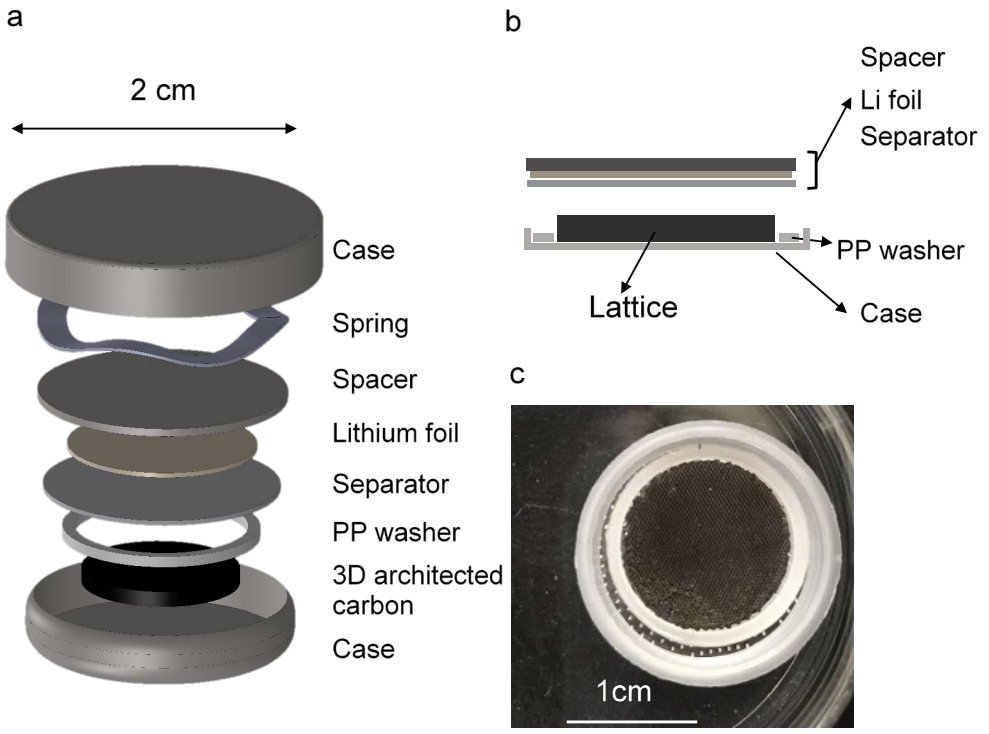

Figure 3. 1 Coin cell components used for cycling 3D architected carbon electrodes. (a) Schematic images of coin cell components. (b) schematic side view of coin cell components (without top case and spring). (c) top view of the 3D architected carbon surrounded by a polypropylene washer on a bottom case.

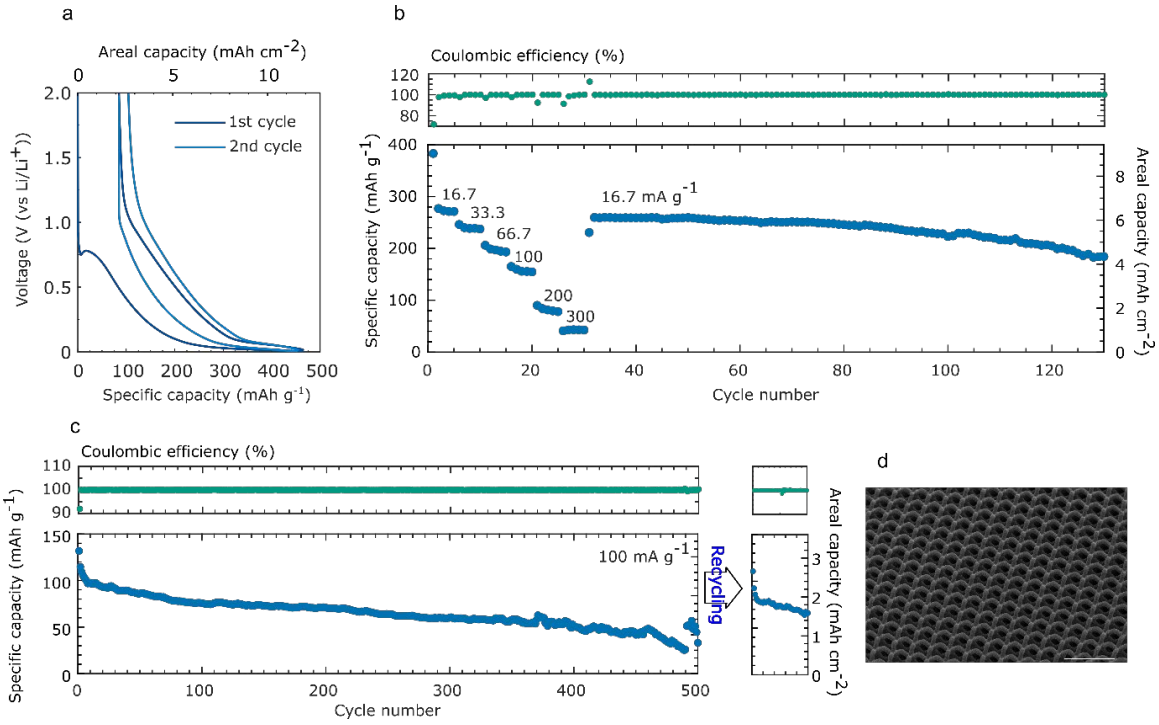

Figure 3. 2 Galvanostatic cycling of architected carbon electrodes. (a) First and second discharge-charge curves at a low current of 2 mA g^{-1}. (b) Columbic efficiency (top) and discharge capacities (bottom) at step currents indicated by the number above each segment and one long cycle at 16.7 mA g^{-1}. (c) Cycling for 500 cycles at 100 mA g^{-1}. (d) SEM image of a representative architected carbon electrode after > 300 cycles at 100 mA g^{-1}. Scale bar is 500 μm for (d).

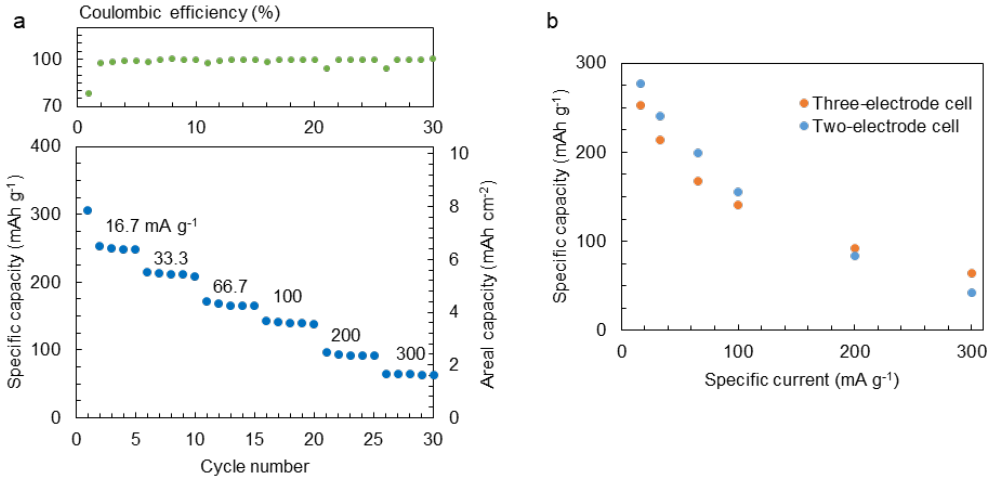

Figure 3. 3 Galvanostatic cycling of architected carbon electrodes using a three-electrode configuration cell. (a) Columbic efficiency (top) and discharge capacities (bottom) at step currents indicated by the number above each segment. (b)

Discharge capacities at 2nd cycle in each step current of the architected carbon electrodes cycled in a three-electrode configuration cell shown in (a) and cycled in a two-electrode configuration cell shown in Figure 3. 2b.

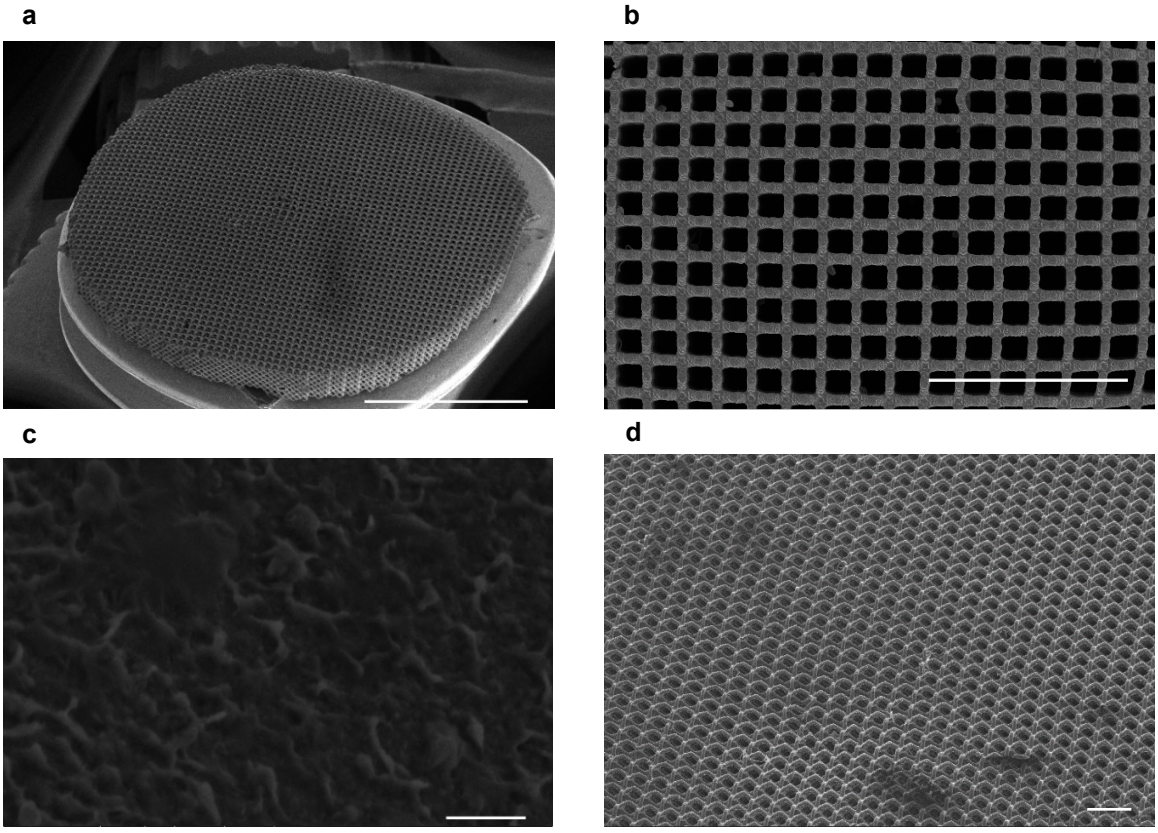

Figure 3. 4 Representative SEM images of the 3D carbon electrodes after >300 cycles at 100 mA g^{-1} in a coin cell. (a) whole view, (b) defected beam pointed by the red circle (c) surface morphology of the beam. (d) SEM image of an 3D carbon electrode after +500 cycles. The scale bars are 5 mm in (a), 1 mm in (b), 500 nm in (c), and 400 mm in (d).

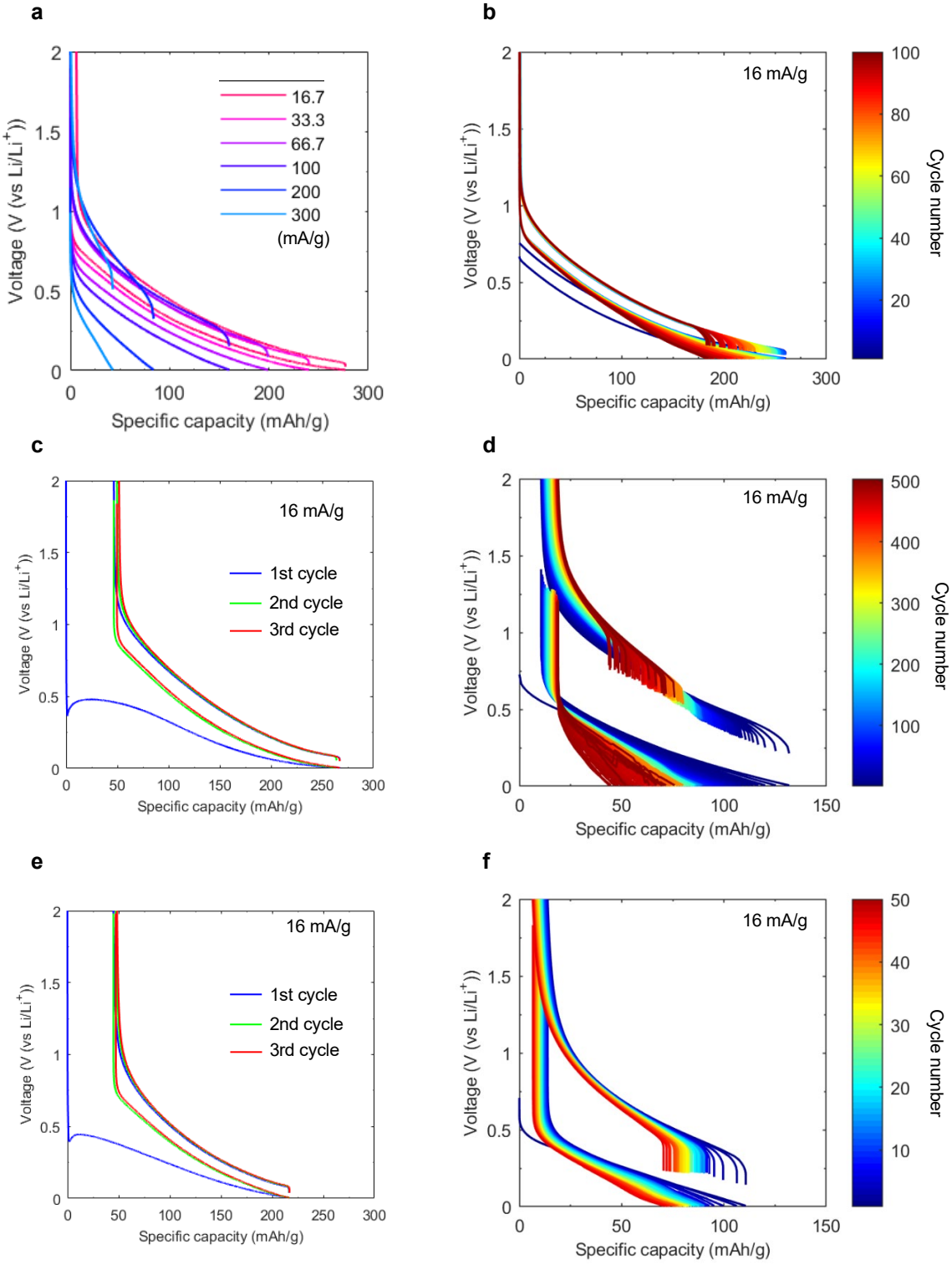
a
Voltage (V (vs Li/Li+))
Specific capacity (mAh/g)
16.7
33.3
66.7
100
200
300
(mA/g)
b
16 mA/g
Cycle number
c
16 mA/g
1st cycle
2nd cycle
3rd cycle
d
16 mA/g
e
16 mA/g
1st cycle
2nd cycle
3rd cycle
f
16 mA/g

Figure 3. 5 Discharge-charge curves for Figure 3.2b: (a) at step currents and (b) at 16 mA g^{-1} after step currents. Discharge-charge curves for Figure 3.2c: (c) at 17 mA g^{-1} as three pre-cycles and (d) at 100 mA g^{-1}, and after recycling (e) at 17 mA g^{-1} as three pre-cycles and (f) at 100 mA g^{-1}.

3.3. Battery Performance of the 3D Architected Carbon Electrode and Electrode Recycling

The architected carbon electrodes in this work display typical discharge and charge behaviors of Li-ion battery hard carbon electrodes. The galvanostatic cycling at 2 mA g^{-1} shows a gradual change in voltage above 0.1 V, with a shift to a plateau at lower voltages, a signature of intercalation into graphitic layers (Figure 3. 2a) [3,8,12]. The abrupt voltage change above 1 V indicates a negligible contribution of double-layer capacitance to the overall measured capacity of architected carbon and is consistent with the relatively low surface area (15 m^2/g) obtained by BET measurement. The capacitive behavior was exhibited by pulverized carbon slurry, which possessed a higher surface area and gained 2.5x greater capacity at high voltages (Figure 4.5, discussed in Chapter 4). The slope region capacity below 1V may be originated from pseudocapacitance and lithium insertion into nanopores surrounding differently-oriented crystallines.

The large irreversible capacity of the first cycle is also not surprising for carbon electrodes; it is indicative of SEI formation during the irreversible reaction in contrast to the reversible lithiation-delithiation reactions [13]. This irreversible capacity can be mitigated by coating soft carbon [14], modifying the photo-resin [15], and optimizing pyrolysis conditions [16].

The Coulombic efficiency beyond 100% at the first cycle after switching current densities from 300 mA g^{-1} to 16.7 mA g^{-1} (Figure 3. 3b) was because of extracting the excess amount of the lithium remained in carbon at former cycles at high current densities.

The architected carbon electrodes retained their structural integrity throughout the cycling and do not require binders, conductive additives, or a substrate, which renders them amenable to recycling and to not require additional treatments, such as mixing with additives, typically necessary for conventional slurry-based electrodes. We demonstrate the recyclability of

architected carbon electrodes by simply washing them in DMC and water, which may have also removed the thick SEI layer, that is likely the key driver of capacity deterioration [17].

3.4. Summary

These architected carbon electrodes with a 23.5-23.6 mg cm^{-2} mass loading showed typical discharge and charge behaviors of hard carbon; abrupt voltage change from 2.0 V to 1.0V, a gradual change up to 0.1 V (pseudocapacitance and lithium insertion into defect sites), and a shift to a plateau at lower voltages (intercalation). An areal capacity of architected carbon electrodes were 4 mAh cm^{-2} at 0.38 mA cm^{-2} over 100 cycles and 3.2 mAh cm^{-2} at 2.4 mA cm^{-2} with a gradual decrease up to around 1 mAh cm^{-2} over 500 cycles. The abrupt voltage change above 1 V indicates a negligible contribution of double-layer capacitance to the overall measured capacity of architected carbon and is consistent with the relatively low surface area (15 m^2/g). Capacitive behavior was exhibited by pulverized carbon slurry, which gained 2.5x greater capacity at high voltages (Figure 4.5). The architected carbon electrodes preserved their prescribed architecture after 500 cycles and were recycled by simple rinsing treatments by DMC and water.

3.5. Detailed Experimental Procedures

Coin cell making process

The cells with 3D architected carbon electrodes were prepared using a stainless steel 2032 coin cell (20 mm diameter. 3.2 mm thickness, MTI). Half-cell was assembled against a lithium foil (99.9%, Sigma-Aldrich) as a counter and reference electrode with 1.0 M lithium hexafluorophosphate in 1:1 (v/v) ratio of ethylene carbonate: diethyl carbonate (Dongguan Shanshan Battery Materials) as received. In addition to standard parts of a coin cell (i.e. cases, electrodes, spring, separator, and spacer), a polypropylene washer was put surrounding the 3D architected carbon to make sure the carbon electrode was positioned in the projected region of the lithium foil. The polypropylene porous separator (gifted from Samsung) was used. The schematics of the components of the coin cell are illustrated in Figure 3. 1. The electrolyte was flooded in a coin cell, and coin cell assembly was conducted using a hydraulic

crimper (MTI) by applying 500 psi on the coin cell. All battery construction was performed in an Ar-filled glove box (HE-243-XW, Vacuum Atmospheres).

Galvanostatic cycling tests and electrode recycling

Galvanostatic cycling tests were conducted using the assembled coin cells by a battery testing machine (BTS3000, Neware) or a battery cycling system (BCS-805, Biologic) at room temperature. Open-circuit voltage was applied for more than four hours before starting cycling tests to obtain equilibrium. Slow current density cycling tests at 2 mA g^{-1} were performed to investigate discharge/charge behaviors without kinetics limitations. Step currents tests were also conducted at 16.7, 33.3, 66.7, 100, 200, 300 mA g^{-1} for every five cycles to evaluate the rate performance of the 3D architected carbon electrodes with different thicknesses. Open-circuit voltage was applied for ten hours before changing the current density. The step current tests were employed for a three-electrode configuration cell (PAT-Cell, EL-CELL) with 3D architected carbon with a 25.7 mg cm^{-2} mass loading as a working electrode, Li foil as a counter electrode, and another Li foil as a reference electrode with 1.0M lithium hexafluorophosphate in 1:1 (v/v) ratio of ethylene carbonate: diethyl carbonate. The voltage between the working and reference electrode was monitored for cut-off voltages. The voltage of the counter electrode against the reference electrode was also monitored.

For the 3D architected carbon, after step currents, 16.7 mA g^{-1} of the current density was applied for investigating the cycle life. Galvanostatic cycling tests at 100 mA g^{-1} were also conducted for more than 500 cycles following three pre-cycling at 16.7 mA g^{-1}. For all galvanostatic cycling tests, cut-off voltages were set at 2 V and 0.005 V. After ending the charge process of the cycles at 100 mA g^{-1} for more than 300 cycles, the coin cell was disassembled with the caution not to deform the 3D architected carbon in the Ar-filled glove box. The cycled 3D architected carbon was rinsed, immersed in dimethyl carbonate (DMC) for overnight, and then dried for observation by SEM. The exposure of the carbon electrode to air while transferring the specimens was minimized up to a few seconds. The 3D architected carbon after 500 cycles was rinsed by DMC and then deionized water. The rinsed sample was dried in a vacuum oven overnight at over 100°C. The rinsing with DMC and

water and drying processes were repeated. Then, a new cell using the 3D architected carbon was assembled with a fresh electrolyte and tested by galvanostatic cycling at 100 mA g^{-1} following three pre-cycling at 16.7 mA g^{-1}.

REFERENCES

1. Franklin, R.E. Crystallite Growth in Graphitizing and Non-Graphitizing Carbons. *Proc. R. Soc. A Math. Phys. Eng. Sci.* **1951**, *209*, 196–218, doi:10.1098/rspa.1951.0197.

2. Kanno, R.; Takeda, Y.; Ichikawa, T.; Nakanishi, K.; Yamamoto, O. Carbon as negative electrodes in lithium secondary cells. *J. Power Sources* **1989**, *26*, 535–543, doi:10.1016/0378-7753(89)80175-2.

3. Dahn, J.R.; Zheng, T.; Liu, Y.; Xue, J.S. Mechanisms for lithium insertion in carbonaceous materials. *Science.* **1995**, *270*, 590–593, doi:10.1126/science.270.5236.590.

4. Takami, N. Structural and kinetic characterization of lithium intercalation into carbon anodes for secondary lithium batteries. *J. Electrochem. Soc.* **1995**, *142*, 371, doi:10.1149/1.2044017.

5. Kubota, K.; Shimadzu, S.; Yabuuchi, N.; Tominaka, S.; Shiraishi, S.; Abreu-Sepulveda, M.; Manivannan, A.; Gotoh, K.; Fukunishi, M.; Dahbi, M.; et al. Structural Analysis of sucrose-derived hard carbon and correlation with the electrochemical properties for lithium, sodium, and potassium insertion. *Chem. Mater.* **2020**, *32*, 2961–2977, doi:10.1021/acs.chemmater.9b05235.

6. Endo, M.; Kim, C.; Nishimura, K.; Fujino, T.; Miyashita, K. Recent development of carbon materials for Li ion batteries. *Carbon N. Y.* **2000**, *38*, 183–197, doi:10.1016/S0008-6223(99)00141-4.

7. Fong, R.; von Sacken, U.; Dahn, J.R. Studies of Lithium intercalation into carbons using nonaqueous electrochemical cells. *J. Electrochem. Soc.* **1990**, *137*, 2009–2013, doi:10.1149/1.2086855.

8. Ogihara, N.; Igarashi, Y.; Kamakura, A.; Naoi, K.; Kusachi, Y.; Utsugi, K. Disordered carbon negative electrode for electrochemical capacitors and high-rate batteries. *Electrochim. Acta* **2006**, *52*, 1713–1720, doi:10.1016/j.electacta.2006.01.082.

9. Legrain, F.; Sottmann, J.; Kotsis, K.; Gorantla, S.; Sartori, S.; Manzhos, S. Amorphous (Glassy) carbon, a promising material for sodium ion battery anodes: A combined first-principles and experimental study. *J. Phys. Chem. C* **2015**, *119*, 13496–13501, doi:10.1021/acs.jpcc.5b03407.

10. Flandrois, S.; Simon, B. Carbon materials for lithium-ion rechargeable batteries. *Carbon N. Y.* **1999**, *37*, 165–180, doi:10.1016/S0008-6223(98)00290-5.

11. Deringer, V.L.; Merlet, C.; Hu, Y.; Lee, T.H.; Kattirtzi, J.A.; Pecher, O.; Csányi, G.; Elliott, S.R.; Grey, C.P. Towards an atomistic understanding of disordered carbon electrode materials. *Chem. Commun.* **2018**, *54*, 5988–5991, doi:10.1039/c8cc01388h.

12. Alvin, S.; Cahyadi, H.S.; Hwang, J.; Chang, W.; Kwak, S.K.; Kim, J. Revealing the intercalation mechanisms of lithium, sodium, and potassium in hard carbon. *Adv. Energy Mater.* **2020**, *10*, 1–16, doi:10.1002/aenm.202000283.

13. An, S.J.; Li, J.; Daniel, C.; Mohanty, D.; Nagpure, S.; Wood, D.L. The state of understanding of the lithium-ion-battery graphite solid electrolyte interphase (SEI) and its relationship to formation cycling. *Carbon N. Y.* **2016**, *105*, 52–76, doi:10.1016/j.carbon.2016.04.008.

14. Lee, J.H.; Lee, H.Y.; Oh, S.M.; Lee, S.J.; Lee, K.Y.; Lee, S.M. Effect of carbon coating on electrochemical performance of hard carbons as anode materials for lithium-ion batteries. *J. Power Sources* **2007**, *166*, 250–254, doi:10.1016/j.jpowsour.2006.12.078.

15. Fujimoto, H.; Tokumitsu, K.; Mabuchi, A.; Chinnasamy, N.; Kasuh, T. The anode performance of the hard carbon for the lithium ion battery derived from the oxygen-containing aromatic precursors. *J. Power Sources* **2010**, *195*, 7452–7456, doi:10.1016/j.jpowsour.2010.05.041.

16. Fujimoto, H.; Mabuchi, A.; Tokumitsu, K.; Kasuh, T. Irreversible capacity of lithium secondary battery using meso-carbon micro beads as anode material. *J. Power Sources* **1995**, *54*, 440–443, doi:10.1016/0378-7753(94)02120-R.

17. Vetter, J.; Novák, P.; Wagner, M.R.; Veit, C.; Möller, K.C.; Besenhard, J.O.; Winter, M.; Wohlfahrt-Mehrens, M.; Vogler, C.; Hammouche, A. Ageing mechanisms in lithium-ion batteries. *J. Power Sources* **2005**, *147*, 269–281, doi:10.1016/j.jpowsour.2005.01.006.

Chapter 4

STRUCTURAL FACTORS AND INFLUENCES ON BATTERY PERFORMANCE

Chapter Abstract

Structural factors of battery electrodes such as porosity, tortuosity, and feature size of electrodes affect maximum Li storage capabilities and trajectories of Li-ion transports, which influences battery performance. In this chapter, we demonstrate 3D architected carbon electrodes as a model system to investigate structural factors and their influences on transports and battery performance. We discuss rate performance as a function of structural factors, including electrode thickness, porosity, feature size, and surface morphology in the framework of ion transport kinetics in the electrode vs. electrolyte and overpotential. The characteristic diffusion time in electrode vs electrolyte revealed that electrode diffusion-limiting rate performance is consistent with our systematically controlled experiments. Surface morphology modification by O_2-plasma etching showed reduced overpotential. We summarize state-of-art battery structure engineering methods, demonstrating that the combination of DLP 3D printing and pyrolysis only enables independent control of the three essential electrode engineering factors (porosity, tortuosity, and feature size) with simultaneous structural integrity. Finally, we discuss rational battery electrode design with the framework of diffusion in electrode and electrolyte.

This chapter has been adapted from:

Narita, K.; Citrin, M.A.; Yang, H.; Xia, X.; Greer, J.R. 3D architected carbon electrodes for energy storage. *Adv. Energy Mater.* 2021, 11, 1–13, doi:10.1002/aenm.202002637.

Contributions: K.N. designed and fabricated samples, performed and analyzed the experiments, and wrote the manuscript.

4.1. Introduction: Structural Factors of Li-Ion Battery Electrodes

Engineering structural factors of porous components facilitate the development of lithium-ion batteries. Porosity, tortuosity, and thickness of porous electrodes at micrometer-to-millimeter scales are key figures of merit in the kinetics and trajectories of electron and ion transports, influencing the power density of batteries. Surface morphology influences electrochemical reactions, and a fraction of active materials in a cell limits the maximum amount of Li that can be stored.

Studies of structural factors and their influence on battery performance have been conducted by modeling and experiments. Commonly employed lithium-ion battery simulations are based on Neman's model [1–3], which accounts for transport in an electrolyte by the concentrated solution theory and porous electrode theory, electrochemical reactions by the Butler-Volmer equation, and transport in electrodes by the diffusion equation. The porous electrode theory averages local structural factors of porous electrodes such as tortuosity, porosity, and electrode diffusion length over a cell, which allows predicting overall battery cell performance with moderate computational power and time and optimizing structural factors for rate performance [3]. Facilitated by these simulations, the structural optimization of battery components are experimentally demonstrated in prior studies using slurry electrodes [4,5], the thin film deposited 3D conductive scaffolds such as inverse opal structures [6] and nano-porous gold [7], and electrodes with unidirectional pore channels by sacrificial templates or laser ablation [8–10].

Among structural engineering methods to control porous electrode structures introduced here and in Chapter 1, none of these methods is capable of creating 3D-architected electrodes that are designed with independent and flexible form-factors from microns to centimeters and are also resilient against cell packaging pressure. The absence of the combination remains indeterministic structural factors under an applied static pressure in a cell for systematic study. This chapter discusses a proof-of-concept study to demonstrate 3D architected carbon electrodes as a model system to investigate structural factors and influences on transports and battery performance. The independent control of structural factors is demonstrated by varying electrode thickness, porosity, feature size, and surface morphology. Slurry electrodes

that represent stochastic structures were employed for comparison. We discuss rate performance as a function of these factors in the framework of ion transport kinetics in the electrode vs. electrolyte and overpotential.

4.2. Battery Performance Comparison between Low-Tortuous and Stochastic Structures

We chose to vary the mass loading by changing the number of lattice layers of 3D architected carbon electrodes while locking all other parameters constant. This allowed us to maintain the same relative density, beam diameter, and surface-area-to-volume ratio for all mass loadings. Figure 4. 1a I-III and b I-III show the specific capacity and areal capacity of 3D architected carbon, respectively, as well as that of two different slurries: (1) the intentionally pulverized architected carbon mixed with conductive additives and binders, referred to as "pulverized slurry" and (2) a commercial graphite slurry electrode, as a function of mass loading for three different charging rates (Figure 4. 2). The highest mass loading attained by 3D architected carbon was ~70 mg cm^{-2}, which corresponds to the thickness of 2 mm; the slurries' loading, controlled through their thickness, hardly approached 30 mg cm^{-2} for pulverized carbon slurry and >40 mg cm^{-2} for graphite slurry and before cracking and delamination from the current collector.

Figure 4. 1a-I reveals that at a slow current of 16.7 mA g^{-1}, the capacity of graphite slurry was more than 30 % higher at ~14 and 40 mg cm^{-2} compared with two other electrode types. A different response was observed at the current of 100 mA g^{-1} (Figure 4. 1a-II), where the capacity of the graphite slurry diminished rapidly with mass loading, leading to more than three times lower capacities than that of the 3D architected carbon at 40 mg cm^{-2}, despite similar capacities at 14 mA g^{-1}. The current of 300 mA g^{-1} (Figure 4. 1a-III) led to a more drastic capacity reduction for graphite slurry at high mass loadings and a superior capacity of 3D architected carbon and pulverized carbon slurry at 14 mg cm^{-2}. Above 30 mg cm^{-2}, only 5-10 mAh g^{-1} of capacity was obtained for both architected carbon and graphite slurry. Figure 4. 1b I-III illustrates that areal capacity increased nearly linearly with mass loading at 16.7 mA g^{-1}, reaching 10.1 mAh cm^{-2} of 3D architected carbon at 65.1 mg cm^{-2}. The 3D

architected carbon attained maximum areal capacity of 3.8 mA cm^{-2} at 23.6 mg cm^{-2} for 100 mA g^{-1} and 1.5 mA cm^{-2} at 13.8 mg cm^{-2} for 300 mA g^{-1}.

We measured overpotential during galvanostatic cycling tests as the voltage drop from the cut-off voltage (2V) in the final charge cycle at each step current to the initially acquired open circuit voltage. Figure 4. 1c I-III shows overpotential measured for the samples as shown in Figure 4. 1a I-III, revealing that overpotential linearly increased with mass loading. The measured overpotential includes a contribution from a lithium counter-electrode, which is likely to be consistent at the same mass loading and specific current density (i.e. same absolute current) among different types of working-electrodes, allowing for a comparison of working-electrode overpotential. We measured the overpotential of a lithium counter-electrode using a three-electrode configuration cell (Figure 4. 3), indicating a 10-20% contribution to cell overpotential. Figure 4. 4 illustrates the correlation of specific capacity and overpotential for different types of electrodes, revealing that graphite slurry showed the most rapid capacity deterioration by overpotential, followed by pulverized slurry and architected carbon.

Discharge and charge curves of architected carbon, pulverized carbon slurry, and graphite slurry with around 14 mg cm^{-2} of mass loading are provided in Figure 4. 5. 3D architected carbon showed less than 10 mAh g^{-1} capacity above 1 V with overlapped charged curves at different current densities. In contrast, pulverized carbon slurry gained more than 25 mAh g^{-1} at 300 mA g^{-1} and above 1 V, and the voltage slope increased at higher current densities in the charge process. The capacity gain from the voltage plateaus for the graphite slurry decreased by over 180 mAh g^{-1} between 16.7 mA g^{-1} to 100 mA g^{-1}, and no voltage plateau was seen at 300 mA g^{-1}. Similar trends were also seen for different mass loadings.

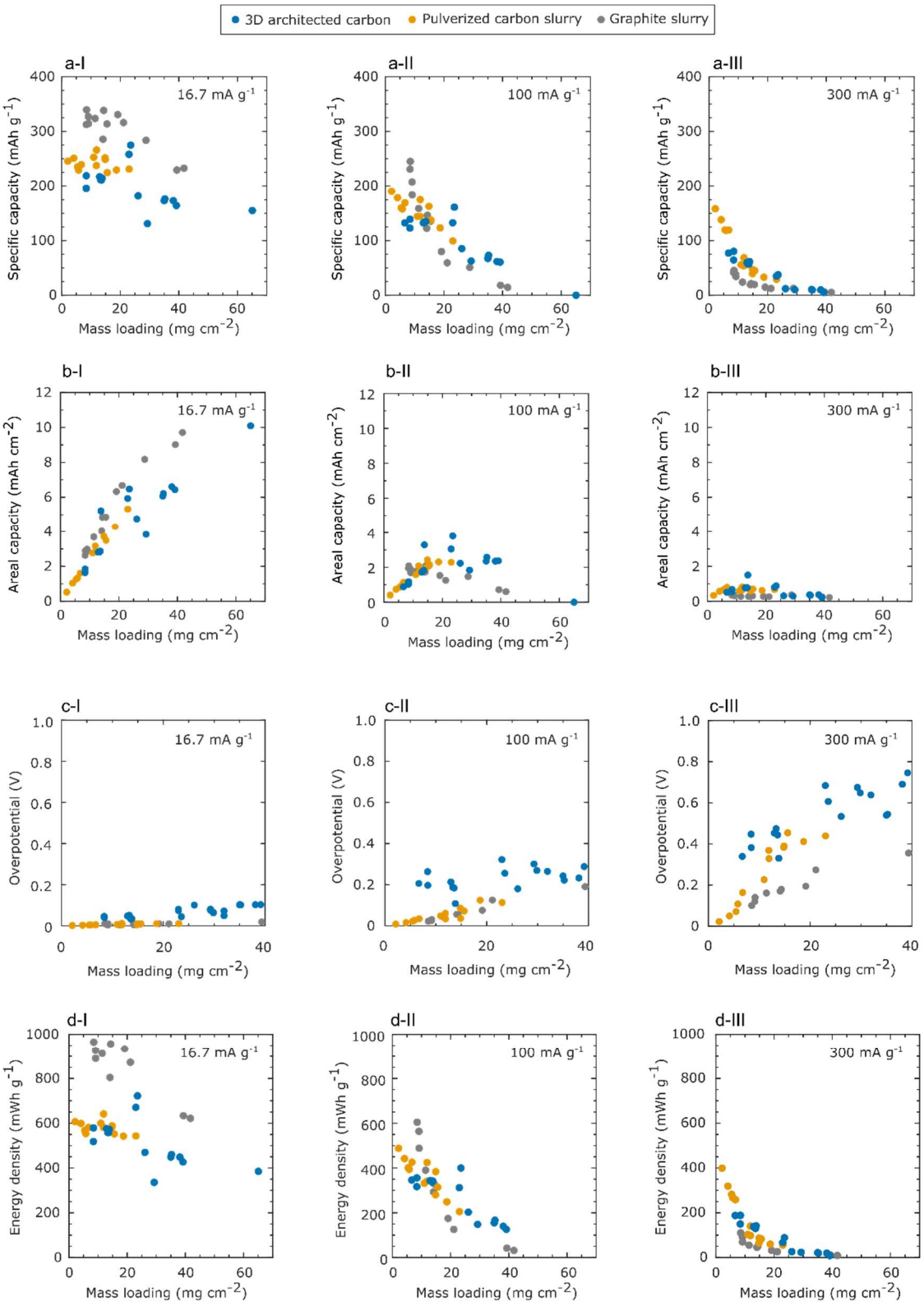
3D architected carbon
Pulverized carbon slurry
Graphite slurry
a-I
a-II
a-III
b-I
b-II
b-III
c-I
c-II
c-III
d-I
d-II
d-III
16.7 mA g-1
100 mA g-1
300 mA g-1
Specific capacity (mAh g-1)
Areal capacity (mAh cm-2)
Overpotential (V)
Energy density (mWh g-1)
Mass loading (mg cm-2)

Figure 4. 1 Comparison of various electrochemical results vs. mass loading for three different types of electrodes at different current densities: specific capacities at (a-I) 16.7 mA g^{-1}, (a-II) 100 mA g^{-1}, and (a-III) 300 mA g^{-1}, areal capacities at (b-I) 16.7 mA g^{-1}, (b-II) 100 mA g^{-1}, and (b-III) 300 mA g^{-1}, overpotential at (c-I) 16.7 mA g^{-1}, (c-II) 100 mA g^{-1}, and (c-III) 300 mA g^{-1}, and energy density vs theoretical SHE cathode at (d-I) 16.7 mA g^{-1}, (d-II) 100 mA g^{-1}, and (d-III) 300 mA g^{-1}.

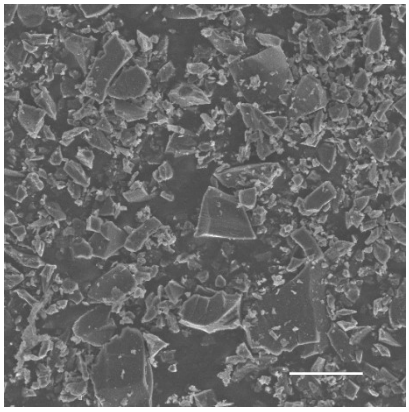

Figure 4. 2 SEM image of pyrolytic carbon particles pulverized from 3D architected carbon. The scale bar is 10 μm.

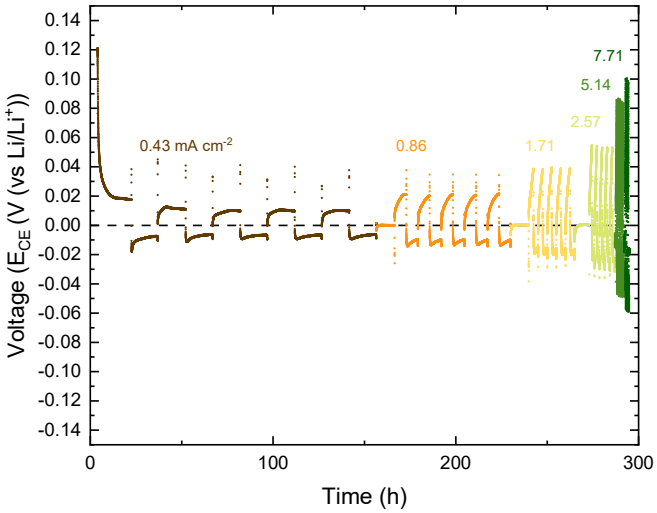

Figure 4. 3 Voltage changes of a lithium counter electrode against a lithium reference electrode in the three-electrode configuration cell with 3D architected carbon working electrode, cycled at step currents shown in Figure 3.3.

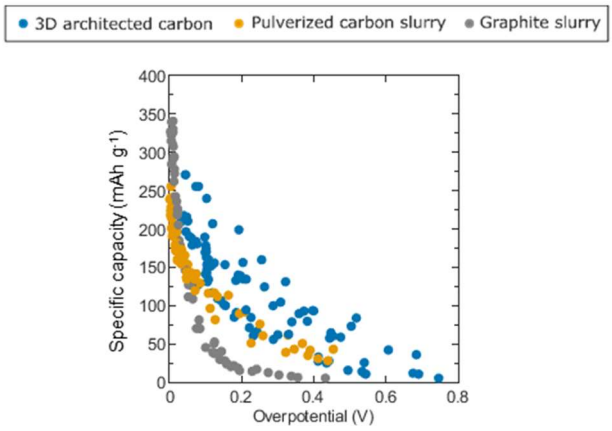

Figure 4. 4 Specific capacities of three types of electrodes with overpotential.

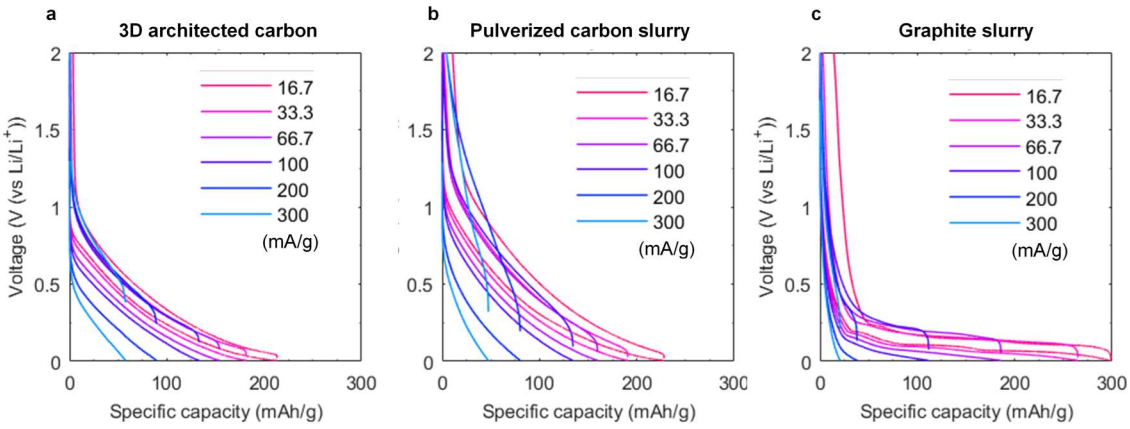

Figure 4. 5 Discharge-charge curves of (a) 3D architected carbon, (b) pulverized carbon slurry and (c) graphite slurry that have around 14 mg cm^{-2} slurry at the 2nd cycle in different current densities. The mass loadings were 13.6 mg cm^{-2} for 3D architected carbon, 15.6 mg cm^{-2} for pulverized carbon slurry, and 14.1 mg cm^{-2} for graphite slurry.

4.3. Independent Control of Structural Factors using 3D Architected Carbon Electrodes

We also explored electrode performance for beam diameters between ~17 and ~30 μm and different surface-area-to-volume-ratios. These structural factors were controlled by adding an O_2 plasma processing step before pyrolysis, which etched the beam diameters and

roughened the surface (Figure 4. 7). We conducted galvanostatic cycling tests on these electrodes to reveal capacity retention and overpontential. Figure 4. 6a shows that the etched 3D carbon had at least a factor of 3 smaller overpotential compared with their non-etched counterparts at a similar mass loading of ~8 mg cm^{-2}. Figure 4. 6b reveals that the charge capacity of the slenderer carbon lattices was 105 mAh g^{-1} at 300 mA g^{-1}, which is ~2.5 times higher than that of the as-fabricated 3D carbon. Those discharge-charge curves for Figure 4. 6a and b are provided in Figure 4. 8.

A fraction of active materials (i.e. relative density of architected carbon) was also explored between 10% and 35% (Figure 4. 9) by adjusting a unit cell-width. Figure 4. 10 compares specific capacity and areal capacity under a similar electrode thickness of ~ 1 mm or a mass loading of 38 mg cm^{-2}. Specific capacities were comparable for the electrodes with similar mass loadings and different relative densities. The denser architected carbon showed lower specific capacity by >30 mAh g^{-1}, but greater areal capacity up to 4.4 mA cm^{-2} than the looser counterparts; for instance, > 1mAh cm^{-2} higher at 0.64 mA cm^{-2}.

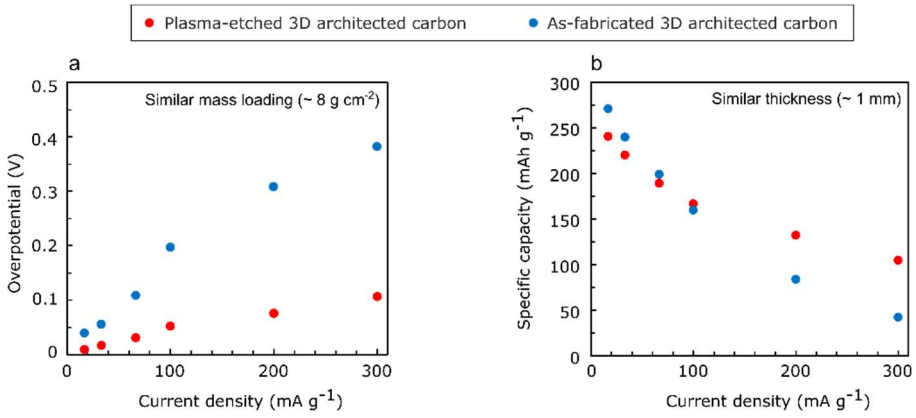

Figure 4. 6 Comparison of architected carbon between as-fabricated and plasma-etched for (a) overpotential with a similar mass loading of ~8 mg cm^{-2}, and (b) specific capacities with a similar thickness of ~1 mm.

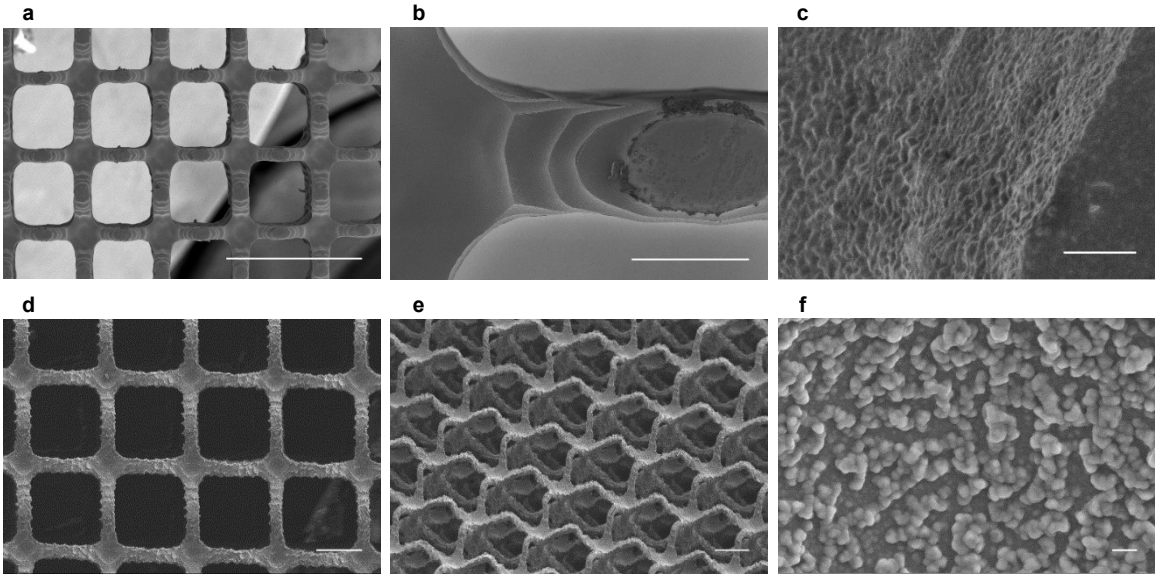

Figure 4. 7 SEM images of the 3D polymer and 3D carbon fabricated by the process involving O_2 plasma etching before pyrolysis. (a)-(c) the 3D polymer after O_2 plasma etching at different magnifications; (d)-(f) 3D carbon fabricated by pyrolysis of the etched 3D polymer at different magnifications. The scale bars are 1 μm in (a), 100 μm in (b), 1 μm in (c), 100 μm in (d) and (e), and 1 μm in (f).

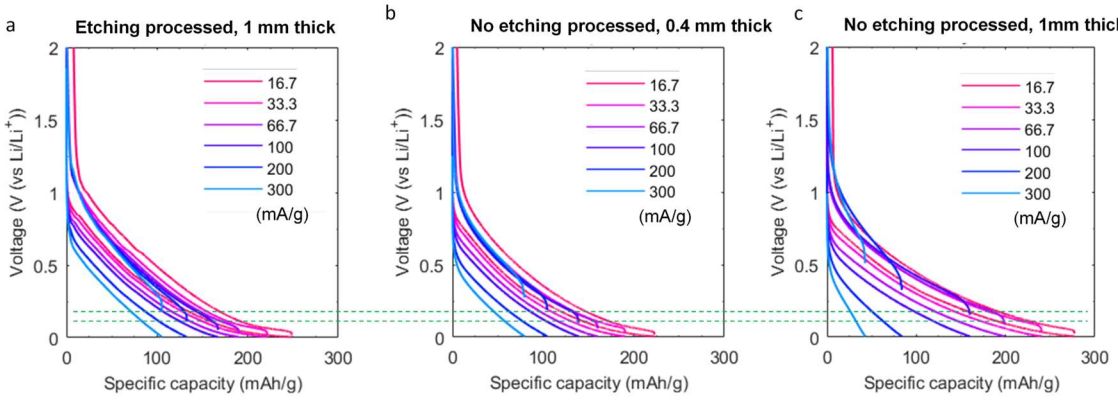

Figure 4. 8 Discharge-charge curves of 3D architected carbon (a) with and (b), (c) without O2 plasma etching process. The mass loadings of (a) and (b) are similar: 8.25 mg cm^{-2} for (a) and 8.42 mg cm^{-2} for (b); meanwhile (a) and (c) have similar thickness: 0.996 mm for (a) and 0.973 mm for (c). Green dot lines show the voltage at the first data acquisition in charge curves at 200 mA g^{-1} (0.1213 V) and 300 mA g^{-1} (0.184 V) for the 3D architected carbon with the etching process.

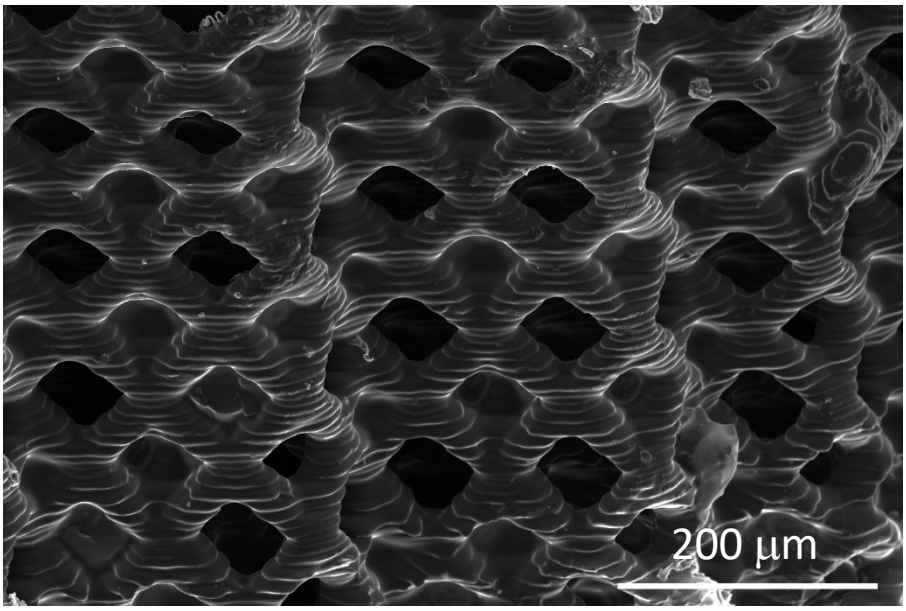

Figure 4. 9 3D architected carbon with 125 μm-wide unit cells.

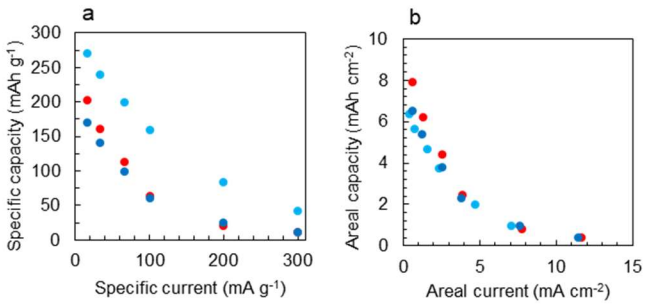

c

Marker	Electrode thickness	Relative density	Mass loading
●	1 mm	35%	38.9 mg cm^{-2}
●	1 mm	10%	24.6 mg cm^{-2}
●	1.4 mm	10%	38.1 mg cm^{-2}

Figure 4. 10 Comparison of rate performance with varied relative density. (a) Specific capacity vs specific current, (b) areal capacity vs areal current of architected carbon electrodes, and (c) geometry of the tested carbon electrodes.

4.4. Relationship between Structural Factors and Electrochemical Results

To develop some guidelines for designing structural factors of architected electrodes for optimal battery performance, we estimate the characteristic Li diffusion time in the electrode (or Li^+ diffusion time in the electrolyte), *t*, as

$$t = \frac{x^2}{D_{eff}} \tag{4.1}$$

for evaluating the rate-limiting process of the electrolyte in-filling the porous electrode structure. Here, x represents the electrode beam radius (or the electrode thickness), which indicate the furthest distances in the filled-in electrolyte and the electrode. The effective diffusivity, D_{eff}, can then be estimated using Bruggeman's relation:

$$D_{eff} = D\frac{\varepsilon}{\tau} \tag{4.2}$$

$$\tau = \varepsilon^{-0.5} \tag{4.3}$$

where D is the intrinsic diffusivity, ε is the electrode porosity, and τ is the tortuosity of the porous electrode. Additional details on these calculations are provided in Appendix A. We found the characteristic diffusion time in the electrode to be >×2 longer than that in the electrolyte, both calculated using Eqs. 4.1-3, for all tested samples but 2 mm-thick architected carbon with 65 mg cm^{-2} (Figure 4. 11). This indicates that the rate-limiting process in the as-fabricated and the pulverized carbon electrodes is diffusion within the solid electrode and not through the electrolyte. This finding is verified experimentally by reducing the diffusion time in the electrode by introducing O_2 plasma etching and showing the improved rate performance for the 3D architected carbon (Figure 4. 6b). The longer diffusion time in the architected carbon-electrolyte compared with that of the pulverized carbon slurry led to negligible difference for their rate performances at similar mass loadings. The architected carbon showed comparable rate performance by decreasing porosity from 90% to 65% with increasing electrode thickness from 1 mm to 1.4 mm to hold the mass loading, increasing diffusion time in the electrolyte (Figure 4. 10), which supports that the rate-limiting process is the transport in electrode.

Another important electrochemical result is overpotential, which is required to surpass resistances plus a thermodynamically determined potential to drive a reaction. The calculated overpotential was attributed to the product of absolute current and the lumped resistance that contains Ohmic resistance and charge transfer resistance as the overpotential scales linearly with the current (Figure 4. 6a). As mass loading increases, overpotential linearly scales at the

same specific current density, which lowered specific capacity (Figure 4. 1a I-III, c I-III, and Figure 4. 4).

To verify that structural factors can modify overpotential, we explored lattices with different surface-area-to-volume by utilizing O_2 plasma etching to create nano-porous surfaces and high surface area electrodes. This resulted in lower effective current densities at each charge transfer reaction site (i.e. currents coupled with charge transfer resistance) and a reduced overpotential (Figure 4. 6a). Our experiments indicate that systematically varying structural factors resulted in the independent control of the following parameters: the diffusion time in electrolyte, active material fraction, surface-to-volume ratio separately and leading to tuning electrochemical results.

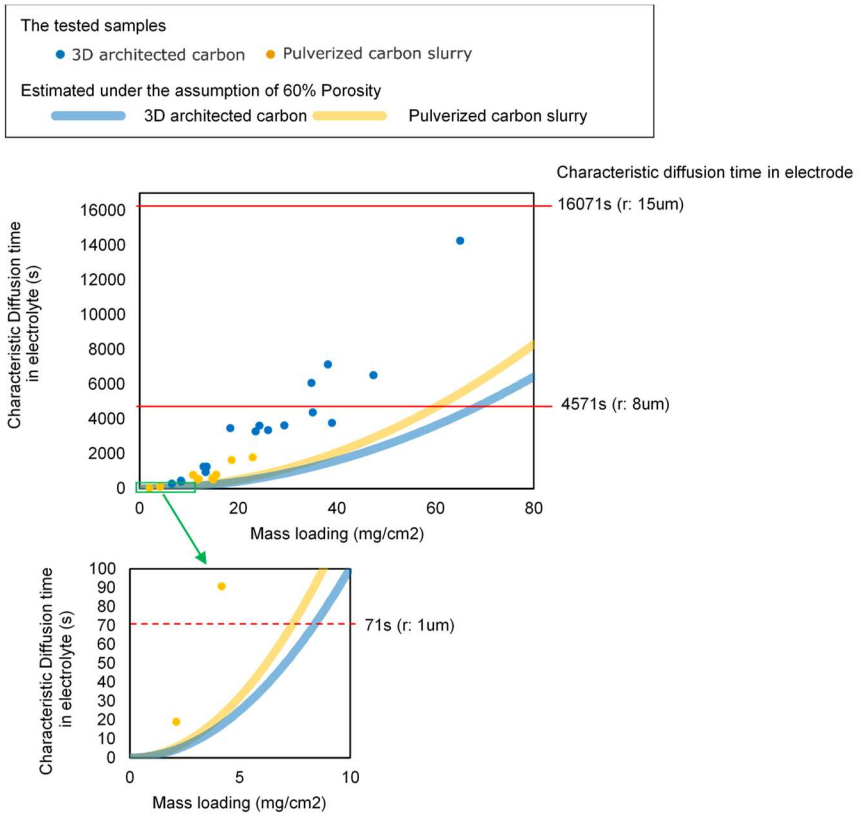

Figure 4. 11 Estimated characteristic diffusion time of Li ion in the electrolyte from tested samples (dots) and electrodes (red lines). Blue and yellow lines show calculated characteristic diffusion time in the electrolyte for 3D architected carbon and pulverized carbon slurry with the assumption of 60% in porosity.

4.5. Comparison with Graphite for Thick Electrodes

Both the architected carbon and the pulverized carbon slurry exhibited greater capacities than that of the graphite slurry with the combinations of high mass loadings and high specific current densities (e,g, >14 mg cm^{-2} at 100 mA g^{-1} or all >8 mg cm^{-2} at 300 mA g^{-1}), as revealed by Figure 4. 1 a I-III. Capacities of the graphite slurry deteriorated more rapidly with overpotential and were lower than those of the pulverized carbon slurry at > 0.05 V overpotential, as shown in Figure 4. 4. One explanation may be that the overpotential results in discharge voltage of graphite slurry reaches cut-off voltage without showing voltage plateaus that account for a large portion of its capacity (Figure 4. 5). Capacity loss of disordered carbon by overpotential is less because disordered carbon gains capacities at high voltage; pulverized carbon slurry gained more than 25 mAh g^{-1} at 300 mA g^{-1} and above 1 V (Figure 4. 8). We also calculated the energy density of architected carbon relative to the potential of theoretical standard hydrogen cathode to be +3.04 V vs Li/Li^+ (Figure 4. 1 d I-III) [11]. The 3D architected carbon and pulverized carbon slurry showed greater energy densities than graphite slurry with > 14 mg cm^{-2} at 100 mA g^{-1} and with > 9 mg cm^{-2} at 300 mA g^{-1}. For instance, energy density of 3D architected carbon was higher than that of graphite by 85 mWh g^{-1} at 40 mg cm^{-2} and 100 mA g^{-1}. It may be worth revisiting disordered carbon as an electrode material for thick electrodes for fast charge purposes.

4.6. Structural Engineering of Battery Electrodes and Their Rational Design

Table 4. 1 summarizes the capabilities of controllable factors among different methods of engineering structural electrodes for Li-ion batteries. In addition to materials versatility, we focus on the control capabilities of three electrode structural factors that significantly affect battery performance**: (1)** the Li diffusion length in an electrode, **(2)** the tortuosity of the porous structure of an electrode, and **(3)** the fraction of active materials in an electrode cell. We did not include other structural factors, such as the electron migration path in the

electrode, which can significantly affect ohmic resistance at high currents and significantly varies with material; for instance, electrical conductivity of carbon is higher than that of lithium transition metal oxides (e.g. lithium cobalt oxide) by 5 or 6 orders of magnitude. We color-coded the electrode engineering factors in Table 4. 1 as: (1) a "restricted factor" (white), i.e. one that has very limited range or cannot be reproducibly controlled, (2) a "correlated factor" (grey), i.e. one that can be reproducibly controlled, but inevitably affects other factors, and (3) an "independent factor" (green), i.e. parameters that can be controlled independently. We also included structural integrity that is a key factor to ensure safe battery operation.

Table 4. 1 Summary of state-of-art methods for engineering electrode structures.

"Reported value" — Restricted factor; Correlated factor; Independent factor

Method		Materials	Solid-diffusion length in electrode [μm]	Tortuosity of diffusion path in electrolyte	Fraction of active materials [v/v]	Structural integrity
Conventional slurry		Versatile	0.03-25	1-12	0.3-0.75	-
Slurry with anisotropic pores		C, LMO, LFP, LCO, NMC	0.05-10	1.3-6.5	0.24-0.59	Moderate
Slurry filled in 3D conductive framework		Versatile	0.05-10	~1	0.2-0.35	-
Planar thin film		Versatile	0.1-15	-	~1	-
Thick monolith		LCO, LFP, LTO	0.05-2	2-3	0.4-0.87	Good
Film on 3D conductive framework	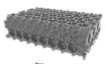	Versatile	0.02-0.2	~1	0.14-0.69	Good
3D monolith by sacrificial template		Versatile	0.005-10	1-3.3	0.26-0.68	Excellent
Extrusion-based 3D printing		LTO, LFP, LMO, Ag, S, LMFP, C	0.1-25	?	0.06-0.43	Moderate
Lithography-based		C, Si, Sn, LMO, LTO, LFP, LCO	0.07-50	1-3	0.08-0.20	Moderate
DLP 3D printing-based (this work)	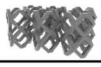	**C**	**8-30**	**~1**	**0.12-0.35**	**Excellent**

* C: carbon, LMO: lithium manganese oxide, LCO: lithium cobalt oxide, LFP: lithium iron phosphate, LTO: lithium titanate , Ag: silver, S: Sulfur, Si: silicon, NMC: Lithium nickel cobalt manganese oxide, LMFP: lithium manganese iron phosphate oxide

* Tortuosity is defined by $\tau = \left(\frac{L'}{L}\right)^2$ where L is apparent thickness and L' is effective ionic transport path

Table 4. 1 unambiguously demonstrates that the combination of DLP 3D printing and pyrolysis presented here enables independent control of the three electrode engineering

factors with a simultaneous structural integrity. Other structural engineering methods are more limited: for instance, sacrificial template methods like colloidal-crystal templates [12] can only fabricate a certain porous structure (i.e. restricted control in tortuosity) because their template structures rely on physical laws (e.g. minimizing free space in the self-assembly of mono-disperse particles [12,13] and phase separation of tri-block copolymers [14]) or natural materials (e.g. woods and diatoms). Extrusion-based 3D printing form stochastic micro/nano pores in the process of consolidating small particles in ink [15–19], having the three electrode engineering factors categorized as correlated factors, although the method can control precisely global geometry and relative positions of the electrodes pair. Other classifications and explanations for each method are described in Appendix B.

The demonstrated independent control of the electrode engineering factors enables us to tune the electrochemical performance, as indicated by the results of varied diffusion length and surface area of the architected carbon (Figure 4. 7). We analytically calculated the required diffusion length in the electrode to shift the rate-limiting process between transport within the electrode vs. in the electrolyte as a function of mass loading and a volume fraction of active materials (Figure 4. 12 and details in Appendix C). Figure 4. 12 indicates that the required electrode-diffusion length increases as the volume fraction decreases and mass loading increases. Specifically, decreasing the diffusion length in the electrode to 1 μm may shift the diffusion-limiting process from transport within the electrode to that in the electrolyte, as would be the case of the combined > 9 mg cm^{-2} of mass loading and 60 % porosity. Under these conditions, the non-tortuous 3D architected carbon may start showing superior rate performance than pulverized carbon slurry at the same mass loadings due to the shorter diffusion time in an electrolyte (Figure 4. 11). Producing electrodes with these factors, e.g. 1 μm beam radius, is a challenge for the existing DLP 3D printers because the resolution of DLP 3D printing depends on pixel resolution of the digital micromirror device, which ranges from 15 to 100 μm [20]. The ranges of controllable factors in the diffusion length in electrode and the fraction of active materials are limited compared with other methods. For instance, the lower limit of diffusion length in the electrode ranges is 15 μm which was several orders of magnitude higher than that of conventional slurry-based electrodes. The attained fraction of active materials in this study ranged in 10%-35%, lower

than that of commercial batteries (~75%) [21]. Those limits may be resolved by further development of 3D printing and other 3D lithography techniques, such as two-photon lithography [22], salt-templating method [23] and additional treatments such as O_2 plasma etching [24].

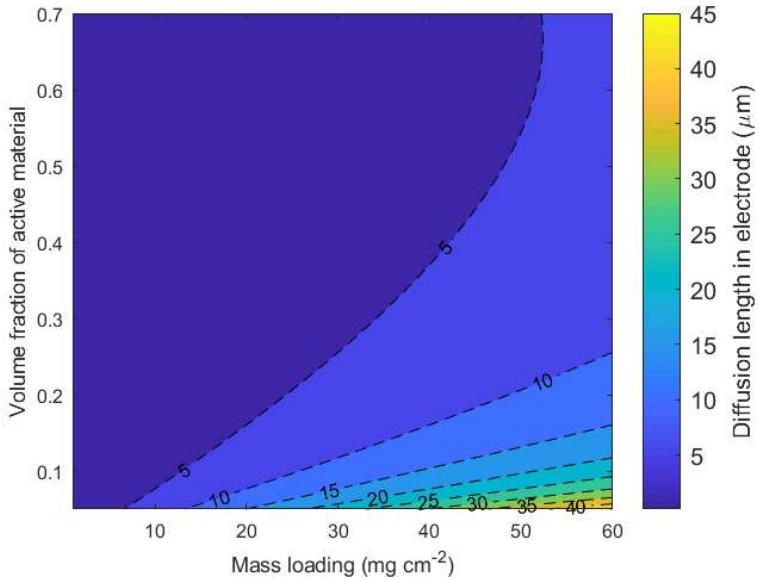

Figure 4. 12 Required diffusion length in the electrode to shift the rate-limiting process between transport in the electrode vs electrolyte as a function of a volume fraction of active materials and mass loading

4.7. Summary and Outlook

We demonstrate independent control of structural factors of the 3D architected carbon electrodes first by varying mass loading (i.e. electrode thickness) while locking other parameters constant and comparing galvanostatic cycling results with pulverized carbon slurry. The comparison of specific capacities with the various mass loadings revealed comparable rate performance at similar mass loadings. The varying porosity of the 3D architected carbon also showed similar rate performance. This is because the rate-limiting process is estimated to be diffusion within the solid electrode and not through the electrolyte, which is verified experimentally by introducing O_2 plasma etching in the fabrication process to reduce the electrode-diffusion time and showing the improved rate performance of the 3D architected carbon. Reducing overpotential was also demonstrated by increasing the surface-

area-to-volume ratio and decreasing effective current density at reaction sites for the 3D architected carbon electrodes.

We summarize the capabilities of controllable factors among different methods of engineering structural electrodes for Li-ion batteries. The combination of DLP 3D printing and pyrolysis in this work enables independent control of three electrode engineering factors with simultaneous structural integrity; however, the ranges of controllable factors are limited compared with other methods. Still, independently controlled electrode engineering factors can make sophisticated architecture—unlike periodic structures that we demonstrated in this study—such as graded pore structures [25], bio-mimetic architecture [26] as well as computationally optimized architecture [27,28]. The optimized architecture may enhance rate performance from the non-optimized 3D carbon in this study, still showing comparable performance to other structure-engineered anodes (Ragone plot in Figure 4. 13).

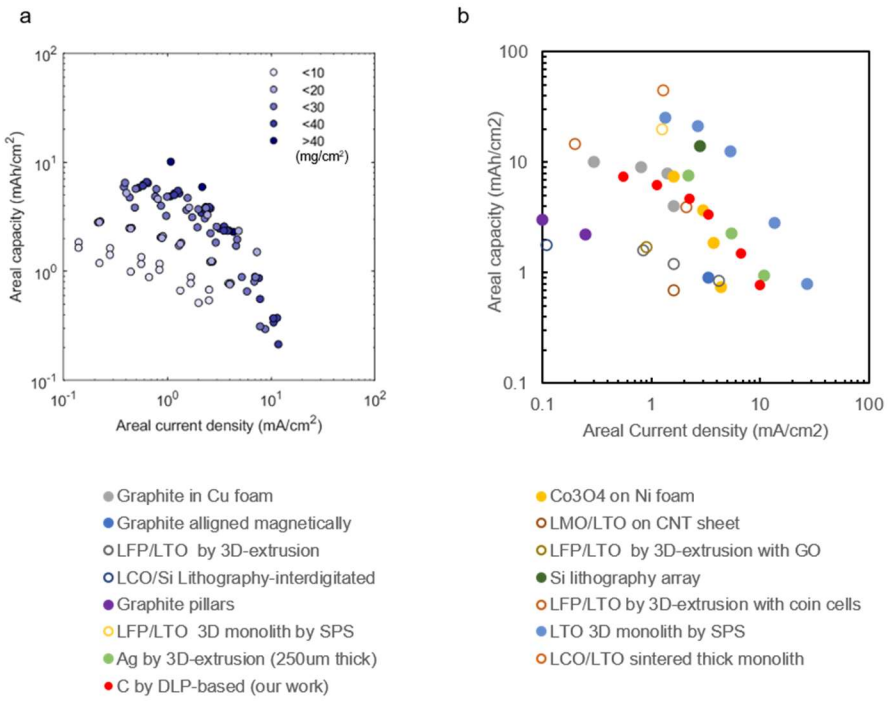

Figure 4. 13 Ragone plots of the structurally engineered electrodes. (a) the 3D architected carbon electrode with different mass loadings, and (b) anode half cells (closed circle) and full cells (open circle) assembled with structurally engineered electrodes. References: graphite in Cu foam [29], Co_3O_4 anode on Ni foam [30], graphite aligned magnetically [31], LMO/LTO on CNT sheet [32], LFP/LTO by 3D-extrusion [19], LFP/LTO by 3D-extrusion with GO [18], LCO/Si

lithography-interdigitated [33], Si lithography array [33], graphite pillars [34], LFP/LTO by 3D-extrusion with coin cells[35], LFP/LTO 3D monolith by SPS [36], LTO 3D monolith by SPS [36], Ag by 3D-extrusion (250um thick) [37], LCO/LTO sintered thick monolith [38]

4.8. Detailed Experimental Procedures

The fabrication and coin cell making procedures for 3D architected carbon electrodes were described in Chapter 2 and Chapter 3. Some of the 3D printed polymer samples were etched using O_2 plasma asher (Zepto B, Diener electronic) for 6 hours and pyrolyzed. The morphology of the etched polymer and pyrolytic carbon derived from the etched polymer was observed by SEM.

The slurry-based electrodes were made for comparison. The 3D architected carbon was crushed by a pestle and mortar, then further pulverized with isopropanol and zirconia balls at 1000 rpm using a vortex mixer (LP Vortex Mixer, Thermo Scientific). The pulverized carbon was dried in a vacuum oven at over 100°C overnight. The pulverized carbon slurry was made by mixing the carbon particles with 5 wt. % Super C65 (Timcal), 10 wt. % polyvinylidene fluoride (PVDF molecular weight 54000 Da, Aldrich) in 1-methyl-2-pyrrolidone (NMP, Sigma-Aldrich). The slurry was cast on a copper foil with various thicknesses using a micrometer film applicator (SH0335, TQC sheen) and dried. Then, the casted slurry was dried in a vacuum oven overnight at over 100°C and assembled using a 2032 coin cell in the same way as the 3D architected carbon except for the usage of the polypropylene washer. The commercial mesocarbon microbeads (MCMB) graphite slurry (MTI) was also made with 5 wt. % Super C65 and 10 wt. % PVDF and assembled in a coin cell in the same way as pulverized carbon slurry. All battery construction was performed in an Ar-filled glove box (HE-243-XW, Vacuum Atmospheres).

Step currents tests were conducted at 16.7, 33.3, 66.7, 100, 200, 300 mA g^{-1} for every five cycles to evaluate the rate performance of the 3D architected carbon electrodes, pulverized carbon slurry electrodes, and graphite slurry electrodes with different thicknesses. The

cycling tests with the step currents were also conducted using plasma-etched architected carbon electrodes.

REFERENCES

1. Doyle, M.; Fuller, T.F.; Newman, J. Modeling of galvanostatic charge and discharge of the lithium/polymer/insertion cell. *J. Electrochem. Soc.* **1993**, *140*, 1526–1533, doi:10.1149/1.2221597.

2. Fuller, T.F.; Doyle, M.; Newman, J. Simulation and optimization of the dual lithium ion insertion cell. *J. Electrochem. Soc.* **1994**, *141*, 1–10, doi:10.1149/1.2054684.

3. Doyle, M.; Newman, J. Analysis of capacity–rate data for lithium batteries using simplified models of the discharge process. *J. Appl. Electrochem.* **1997**, *27*, 846–856, doi:10.1023/A:1018481030499.

4. Du, Z.; Wood, D.L.; Daniel, C.; Kalnaus, S.; Li, J. Understanding limiting factors in thick electrode performance as applied to high energy density Li-ion batteries. *J. Appl. Electrochem.* **2017**, *47*, 405–415, doi:10.1007/s10800-017-1047-4.

5. Liu, C.; Liu, L. Optimal design of Li-ion batteries through multi-physics modeling and multi-objective optimization. *J. Electrochem. Soc.* **2017**, *164*, E3254–E3264, doi:10.1149/2.0291711jes.

6. Pikul, J.H.; Braun, P. V.; King, W.P. Performance modeling and design of ultra-high power microbatteries. *J. Electrochem. Soc.* **2017**, *164*, E3122–E3131, doi:10.1149/2.0151711jes.

7. Ye, J.; Baumgaertel, A.C.; Wang, Y.M.; Biener, J.; Biener, M.M. Structural optimization of 3D porous electrodes for high-rate performance lithium ion batteries. *ACS Nano* **2015**, *9*, 2194–2202, doi:10.1021/nn505490u.

8. Usseglio-Viretta, F.L.E.; Mai, W.; Colclasure, A.M.; Doeff, M.; Yi, E.; Smith, K. Enabling fast charging of lithium-ion batteries through secondary-/dual-pore network: Part I - Analytical diffusion model. *Electrochim. Acta* **2020**, *342*, 136034, doi:10.1016/j.electacta.2020.136034.

9. Mai, W.; Usseglio-Viretta, F.L.E.; Colclasure, A.M.; Smith, K. Enabling fast charging of lithium-ion batteries through secondary-/dual-pore network: Part II – Numerical model. *Electrochim. Acta* **2020**, *341*, 136013, doi:10.1016/j.electacta.2020.136013.

10. Bae, C.J.; Erdonmez, C.K.; Halloran, J.W.; Chiang, Y.M. Design of battery electrodes with dual-scale porosity to minimize tortuosity and maximize performance. *Adv. Mater.* **2013**, *25*, 1254–1258, doi:10.1002/adma.201204055.

11. Cao, Y.; Li, M.; Lu, J.; Liu, J.; Amine, K. Bridging the academic and industrial metrics for next-generation practical batteries. *Nat. Nanotechnol.* **2019**, *14*, 200–207, doi:10.1038/s41565-019-0371-8.

12. Lee, K.T.; Lytle, J.C.; Ergang, N.S.; Oh, S.M.; Stein, A. Synthesis and rate performance of monolithic macroporous carbon electrodes for lithium-ion secondary batteries. *Adv. Funct. Mater.* **2005**, *15*, 547–556, doi:10.1002/adfm.200400186.

13. Stein, A.; Wilson, B.E.; Rudisill, S.G. Design and functionality of colloidal-crystal-templated materials—chemical applications of inverse opals. *Chem. Soc. Rev.* **2013**, *42*, 2763–2803, doi:10.1039/C2CS35317B.

14. Werner, J.G.; Rodríguez-Calero, G.G.; Abruña, H.D.; Wiesner, U. Block copolymer derived 3-D interpenetrating multifunctional gyroidal nanohybrids for electrical energy storage. *Energy Environ. Sci.* **2018**, *11*, 1261–1270, doi:10.1039/c7ee03571c.

15. Lacey, S.D.; Kirsch, D.J.; Li, Y.; Morgenstern, J.T.; Zarket, B.C.; Yao, Y.; Dai, J.; Garcia, L.Q.; Liu, B.; Gao, T.; et al. Extrusion-based 3D printing of hierarchically porous advanced battery electrodes. *Adv. Mater.* **2018**, *1705651*, 1–9, doi:10.1002/adma.201705651.

16. Shen, K.; Mei, H.; Li, B.; Ding, J.; Yang, S. 3D printing sulfur copolymer-graphene architectures for Li-S batteries. *Adv. Energy Mater.* **2018**, *8*, 1–6, doi:10.1002/aenm.201701527.

17. Li, J.; Liang, X.; Liou, F.; Park, J. Macro-/micro-controlled 3D lithium-ion batteries via additive manufacturing and electric field processing. *Sci. Rep.* **2018**, *8*, 1–11, doi:10.1038/s41598-018-20329-w.

18. Fu, K.; Wang, Y.; Yan, C.; Yao, Y.; Chen, Y.; Dai, J.; Lacey, S.; Wang, Y.; Wan, J.; Li, T.; et al. Graphene oxide-based electrode inks for 3D-printed lithium-ion batteries. *Adv. Mater.* **2016**, *28*, 2587–2594, doi:10.1002/adma.201505391.

19. Sun, K.; Wei, T.S.; Ahn, B.Y.; Seo, J.Y.; Dillon, S.J.; Lewis, J.A. 3D printing of interdigitated Li-ion microbattery architectures. *Adv. Mater.* **2013**, *25*, 4539–4543, doi:10.1002/adma.201301036.

20. Low, Z.X.; Chua, Y.T.; Ray, B.M.; Mattia, D.; Metcalfe, I.S.; Patterson, D.A. Perspective on 3D printing of separation membranes and comparison to related unconventional fabrication techniques. *J. Memb. Sci.* **2017**, *523*, 596–613, doi:10.1016/j.memsci.2016.10.006.

21. Marks, T.; Trussler, S.; Smith, A.J.; Xiong, D.; Dahn, J.R. A Guide to Li-ion coin-cell electrode making for academic researchers. *J. Electrochem. Soc.* **2011**, *158*, A51, doi:10.1149/1.3515072.

22. Bauer, J.; Schroer, A.; Schwaiger, R.; Kraft, O. Approaching theoretical strength in glassy carbon nanolattices. *Nat. Mater.* **2016**, *15*, 438–443, doi:10.1038/nmat4561.

23. Chen, X.; Zhao, G.; Wu, Y.; Huang, Y.; Liu, Y.; He, J.; Wang, L.; Lian, Q.; Li, D. Cellular carbon microstructures developed by using stereolithography. *Carbon N. Y.* **2017**, *123*, 34–44, doi:10.1016/j.carbon.2017.07.043.

24. De Volder, M.F.L.; Vansweevelt, R.; Wagner, P.; Reynaerts, D.; Van Hoof, C.; Hart, A.J. Hierarchical carbon nanowire microarchitectures made by plasma-assisted pyrolysis of photoresist. *ACS Nano* **2011**, *5*, 6593–6600, doi:10.1021/nn201976d.

25. Dai, Y.; Srinivasan, V. On graded electrode porosity as a design tool for improving

the energy density of batteries. *J. Electrochem. Soc.* **2016**, *163*, A406–A416, doi:10.1149/2.0301603jes.

26. West, G.B.; Brown, J.H.; Enquist, B.J. The fourth dimension of life: Fractal geometry and allometric scaling of organisms. *Science.* **1999**, *284*, 1677–1679, doi:10.1126/science.284.5420.1677.

27. Dan, N.; Bejan, A. Constructal tree networks for the time-dependent discharge of a finite-size volume to one point. *J. Appl. Phys.* **1998**, *84*, 3042–3050, doi:10.1063/1.368458.

28. Usiskin, R.E.; Maier, J. Guidelines for optimizing the architecture of battery insertion electrodes based on the concept of wiring lengths. *Phys. Chem. Chem. Phys.* **2018**, *20*, 16449–16462, doi:10.1039/c8cp01946k.

29. Wang, J.S.; Liu, P.; Sherman, E.; Verbrugge, M.; Tataria, H. Formulation and characterization of ultra-thick electrodes for high energy lithium-ion batteries employing tailored metal foams. *J. Power Sources* **2011**, *196*, 8714–8718, doi:10.1016/j.jpowsour.2011.06.071.

30. Wang, X.; Fan, Y.; Agung Susantyoko, R.; Xiao, Q.; Sun, L.; He, D.; Zhang, Q. High areal capacity Li ion battery anode based on thick mesoporous Co3O4nanosheet networks. *Nano Energy* **2014**, *5*, 91–96, doi:10.1016/j.nanoen.2014.02.005.

31. Billaud, J.; Bouville, F.; Magrini, T.; Villevieille, C.; Studart, A.R. Magnetically aligned graphite electrodes for high-rate performance Li-ion batteries. *Nat. Energy* **2016**, *1*, 1–6, doi:10.1038/nenergy.2016.97.

32. Weng, W.; Sun, Q.; Zhang, Y.; He, S.; Wu, Q.; Deng, J.; Fang, X.; Guan, G.; Ren, J.; Peng, H. A gum-like lithium-ion battery based on a novel arched structure. *Adv. Mater.* **2015**, *27*, 1363–1369, doi:10.1002/adma.201405127.

33. Hur, J.I.; Smith, L.C.; Dunn, B. High Areal energy density 3D lithium-ion

microbatteries. *Joule* **2018**, 1–15, doi:10.1016/j.joule.2018.04.002.

34. Cirigliano, N.; Sun, G.; Membreno, D.; Malati, P.; Kim, C.J.; Dunn, B. 3D Architectured anodes for lithium-ion microbatteries with large areal capacity. *Energy Technol.* **2014**, *2*, 362–369, doi:10.1002/ente.201402018.

35. Wei, T.-S.; Ahn, B.Y.; Grotto, J.; Lewis, J.A. 3D printing of customized li-ion batteries with thick electrodes. *Adv. Mater.* **2018**, *1703027*, 1703027, doi:10.1002/adma.201703027.

36. Elango, R.; Demortière, A.; De Andrade, V.; Morcrette, M.; Seznec, V. Thick binder-free electrodes for li-ion battery fabricated using templating approach and spark plasma sintering reveals high areal capacity. *Adv. Energy Mater.* **2018**, *1703031*, 1–8, doi:10.1002/aenm.201703031.

37. Saleh, M.S.; Li, J.; Park, J.; Panat, R. 3D printed hierarchically-porous microlattice electrode materials for exceptionally high specific capacity and areal capacity lithium ion batteries. *Addit. Manuf.* **2018**, *23*, 70–78, doi:10.1016/j.addma.2018.07.006.

38. Robinson, J.P.; Ruppert, J.J.; Dong, H.; Koenig, G.M. Sintered electrode full cells for high energy density lithium-ion batteries. *J. Appl. Electrochem.* **2018**, *48*, 1297–1304, doi:10.1007/s10800-018-1242-y.

Chapter 5

FORMATION, STRUCTURE, AND RESISTANCE OF SOLID ELECTROLYTE INTERPHASE AT MULTIPLE LENGTH SCALES

Chapter Abstract

Solid state electrolyte (SEI) is associated with most of the degradation mechanisms of anodes in lithium-ion batteries. In this study, deterministic, periodic, and mechanically resilient 3D architected carbon electrodes with a thickness of >600 μm and a coin cell were used to assemble a half-cell with 1M $LiPF_6$ in 1:1 (v/v) ratio of EC: DEC for studying the formation, structure-resistance relationship, and position-dependent growth of SEI by combining the newly developed DC-based technique and depth analysis using secondary ion mass spectroscopy (SIMS) as post-characterization. We discovered that Li consumption estimation for SEI growth using the cumulative ΔQ, defined as the difference of capacity at each cycle and the last cycle, showed a strong linear correlation with the Li amount in SEI obtained by SIMS. The total counts of F in SEI obtained by SIMS showed a good correlation with SEI resistance evolution, which may be attributed to the formation of LiF, an ionic insulator, during SEI growth. The SIMS analysis along the electrode-thickness direction revealed a higher amount of Li and a lower amount of F in SEI toward the separator side, which implies that the consideration of LiF components as multi-layer SEI may be necessary for precise estimations of battery aging. These results provide new insights for battery aging of thick electrodes with fast charging.

This chapter has been adapted from:

Narita, K.; Greer, J.R. Solid electrolyte interphase growth, structure, and properties at multiple length scales. *In Preparation*.

Contributions: K.N. participated in the conception of the project, designed and fabricated samples, performed and analyzed the experiments, and wrote the manuscript.

5.1. Introduction

Improving the cycle life of Li-ion batteries is critical to reducing the environmental and economic impacts of the productions and disposal of batteries and to meeting ever-growing energy demands in modern human society. In battery operation, solid electrolyte interphase (SEI) is formed on the surface of anodes when potentials at the interface with an electrolyte are lower than the stability window of the electrolyte. The formed SEI covers the electrode surface, which protects from aggressive electrolyte decomposition and enables reversible lithiation/delithiation. However, the growth of SEI leads to battery degradation over long-term operation.

The degradation mechanisms of Li-ion batteries have been extensively investigated and proposed [1–5]. Table 5. 1 summarizes the mechanisms associated with anodes in a cell using a liquid electrolyte [5]. Electrolyte decomposition and SEI formation are associated with most of the degradation effects: 1) loss of cyclable lithium inventory [6], 2) impedance increase [7], 3) decrease of accessible surface area for lithiation/delithiation reactions, and 4) decrease of porosity, which limits Li-ion transport in an electrolyte [8]. These SEI-related degradation mechanisms can be linked to three different kinetics about SEI: a) Li consumption to form SEI, b) structure-property relationship of SEI, and c) position-dependent SEI growth.

Table 5. 1 Li-ion battery degradation mechanism associated with an anode. Adopted from [5].

Cause	Effect	Leads to	Reduced by	Enhanced by
Electrolyte decomposition (→SEI) (Continuous side reaction at low rate)	Loss of lithium Impedance rise	**Capacity fade** **Power fade**	Stable SEI (additives) Rate decreases with time	High temperatures High SOC (low potential)
Solvent co-intercalation, gas evolution and subsequent cracking formation in particles	Loss of active material (graphite exfoliation) Loss of lithium	Capacity fade	Stable SEI (additives) Carbon pre-treatment	Overcharge
Decrease of accessible surface area due to continuous SEI growth	Impedance rise	**Power fade**	Stable SEI (additives)	High temperatures High SOC (low potential)
Changes in porosity due to volume changes, SEI formation and growth	Impedance rise Overpotentials	Power fade	External pressure Stable SEI (additives)	High cycling rate High SOC (low potential)
Contact loss of active material particles due to volume changes during cycling	Loss of active material	**Capacity fade**	External pressure	High cycling rate High DOD
Decomposition of binder	Loss of lithium Loss of mechanical stability	Capacity fade	Proper binder choice	High SOC (low potential) High temperatures
Current collector corrosion	Overpotentials Impedance rise Inhomogeneous distribution of current and potential	Power fade Enhances other ageing mechanisms	Current collector pre-treatment (?)	Overdischarge Low SOC (high potential)
Metallic lithium plating and subsequent electrolyte decomposition by metallic Li	Loss of lithium (Loss of electrolyte)	Capacity fade (power fade)	Narrow potential window	Low temperature High cycling rates Poor cell balance Geometric misfits

Precise estimation of the amount of Li consumed for the SEI formation is essential to understand Li inventory loss and SEI growth, but has been overlooked. A common parameter used to estimate capacity used for SEI formation is irreversible capacity loss, which is defined as the difference between charge capacity and discharge capacity [2,9–11]. In particular, the irreversible capacity loss for the first cycle is often used as a parameter that represents SEI formation for carbon electrodes with different microstructure or surface modifications [9]. For the long cycle operation, cumulative irreversible capacities follow $time^{0.5}$ scaling, consistent with transport-limited surface layer growth [11,12]. These studies mostly employ electrochemical characterizations; it has not been experimentally demonstrated yet that irreversible capacity represents the consumption of Li for SEI formation with non-electrochemical characterizations.

Experimental investigations on the structure and property relationship of SEI have been conducted mostly using a thin electrode. SEI formed on a Cu film has been studied by

electrochemical impedance spectroscopy (EIS) and secondary ion mass spectroscopy (SIMS), which showed nonlinear resistance change as a function of SEI thickness [13,14]. Individual SEI components, Li_2O and LiF, were grown on Li metal at the same scale as SEI (i.e. tens nanometers) and evaluated for their conductivities: ~ 1×10^{-9} S cm^{-1} for Li_2O and ~5×10^{-10} S cm^{-1} for LiF. [15,16]. Investigating the multicomponent SEI formed on porous electrodes has been challenging because of its inhomogeneous formation [17], complex structure [18], air-sensitivity [19], and sensitivity to cell and cycling conditions [18,20–22]. Fluorine-containing binders (e.g. polyvinylidene difluoride (PVdF)) and transition metal oxide cathodes also have an influence on the SEI formation and structure, for instance, facilitating LiF formation [23,24] and transition metal incorporation [25], respectively.

Position-dependent SEI formation has been proposed by numerical simulations [26–28]. SEI grows faster at the position closer toward the separator along the through-thickness direction because of ion consumption in the electrolyte during lithiation processes. Pinson proposed that the position-dependent SEI formation is more noticeable for a thick electrode (e.g. 250 μm) with fast charging (e.g. 3C), which causes strong depletion of the electrolyte. The position-dependent SEI growth behaviors have not been experimentally demonstrated, mostly because of the deviation of local structural factors between experiments and simulations. The porous electrode theory adopted in Newman's model averages local structural factors in planes parallel to the stacked layers in a cell. In contrast, the local SEI growth in slurry electrodes may be significantly affected by these local structural factors, such as local porosity and tortuosity. This indicates that structure characterization of SEI at the nanoscale may not show a representative structure of SEI at a distance from the current collector. Quantifying these local structural factors in a stochastic and nondeterministic structure of slurry electrodes requires additional tomographic imaging and computationally expensive 3D multi-physics modeling. Overall, there is a lack of experimental studies on the relationship of structure, property, and formation of SEI and these variations in porous electrodes along the through-thickness direction.

To provide a systematic understanding of SEI, we employed 3D architected carbon electrodes with independently controlled micrometer-to-centimeter form-factors as a model system to study these SEI formation kinetics with post-characterizations and electrochemical characterizations. We used a secondary ion mass spectroscopy (SIMS) for post-characterizations, which elucidates the structure of SEI at the nanoscale by elemental depth profiles. For electrochemical characterizations, we developed a new technique that distinguishes different resistance contributions (e.g. SEI resistance vs charge transfer resistance) using constant currents or DC measurement; we coined Direct Current Spectroscopy (DCS). The deterministic, interconnected, periodic, and non-tortuous 3D architected carbon allows us to decouple complex aging mechanisms associated with SEI from an influence of transport due to local porosity decrease by SEI growth [8], the contribution of inactive materials such as binders and conductive additives to SEI growth, and electrical contact loss or contact resistance increase of active materials. We chose a half-cell with 3D architected carbon as a working electrode and a Li-metal counter and a reference electrode to eliminate influences by transition metal dissolution from cathodes and cyclable Li-inventory loss. The mechanical resilience of 3D architected carbon enables SIMS characterizations at different positions throughout the preserved architecture after cycling. In this experimental setting, we can unambiguously study the formation, structure, and resistance of SEI at the nanoscale and their position-dependency throughout porous electrodes at the sub-millimeter scale, not feasible by slurry electrodes or in-situ techniques using thin film electrodes.

5.2. Brief Procedures of Position-Dependent SEI Characterization using 3D Architected Carbon Electrodes

Figure 5. 1 overviews procedures to investigate SEI on 3D architected carbon electrodes; 1) fabricating 3D architected carbon electrodes with prescribed form factors, 2) conducting galvanostatic cycling using a coin cell, 3) disassembling the cell, rinsing the electrode, creating a cross-section, and coating the cross-section by gold in a glovebox, and 4) performing depth analysis by SIMS at different positions on the cross-section from the

current collector side to separator side. First, we fabricated the 3D carbon by DLP 3D printing and post-exposure pyrolysis processes at 1000°C. The detailed fabrication conditions are described in Chapter 2. Representative architected carbon samples used for cycling and SIMS analysis were disk-shaped composed of cuboid unit cells with a diameter of ~6 mm, a porosity of ~70%, and varied thicknesses of 0.6-1.1 mm. Diameters and intervals of the beams were ~35 μm and ~72 μm for the through-plane direction of the disk sample and ~22 μm and ~93 μm for the in-plane direction. The microstructure of the 3D carbon was disordered structures composed of several stacked graphitic layers (see Chapter 2 for more details). A 2032 coin cell was used to assemble a half-cell with the 3D architected carbon electrodes and a Li-metal counter and reference electrode. An electrolyte of 1M $LiPF_6$ in 1:1 (v/v) ratio of EC: DEC was flooded in the cell. For the selected electrodes, a polypropylene washer was inserted surrounding the caron electrode to minimize Li-ion transport from the side and effectively investigate an effect of Li-ion transport along the electrode thickness direction (denoted as with washer in Table 5. 2).

The assembled cells were first rested for more than 4 hours to ensure complete electrolyte wetting. As the extreme case exhibiting different SEI formation and structure, two selected cells were rested for more than 24 hours and disassembled in an Ar-filled glove box. The carbon electrodes were then rinsed by the 1M $LiPF_6$ in EC: DEC and used for assembling a new coin cell with fresh electrolyte and Li-metal (denoted as Reassembly in Table 5. 2). The cells were subject to galvanostatic processes at 50 mA g^{-1} for one cycle to form a stable SEI and at 200 mA g^{-1} for 10 cycles to cause polarization in the electrolyte and investigate position-dependent SEI formation. Potentiostatic electrochemical impedance spectroscopy was conducted after the first cycle and 11th cycles. One sample assembled without a washer underwent another discharge half-cycle at 20 mA g^{-1} as a reference to quantity Li concentrations in carbon and SEI as discussed later. The cycled cells were disassembled, rinsed by dimethyl carbonate, and dried in a glovebox. The dried cells were cut into a semi-circle disk shape, and the cross-section was coated with gold to prevent direct air exposure during the transfer to a SIMS instrument. The number of samples characterized by SIMS is summarized in Table 5. 2. The depth analyses of 6 different secondary ions (7Li, 12C,

16O1H, 19F, 31P, and 197Au) were conducted at 3-5 different positions on the cross-section along the electrode thickness direction by Cs^+ sputtering through a protective gold layer. Note that one sample without a washer and single assembly, and which ended the cycling process with charge (i.e., delitiation), was characterized by different secondary ions for Li (7Li16O).

Table 5. 2 summarizes the number of tested samples with different cell-making conditions. We show the results of cycling and the SIMS analysis using the sample with a single assembly and a washer as a representative sample throughout this chapter. For another sample type, such as the sample with washer and reassembly, the results are summarized in Figure 5. 7.

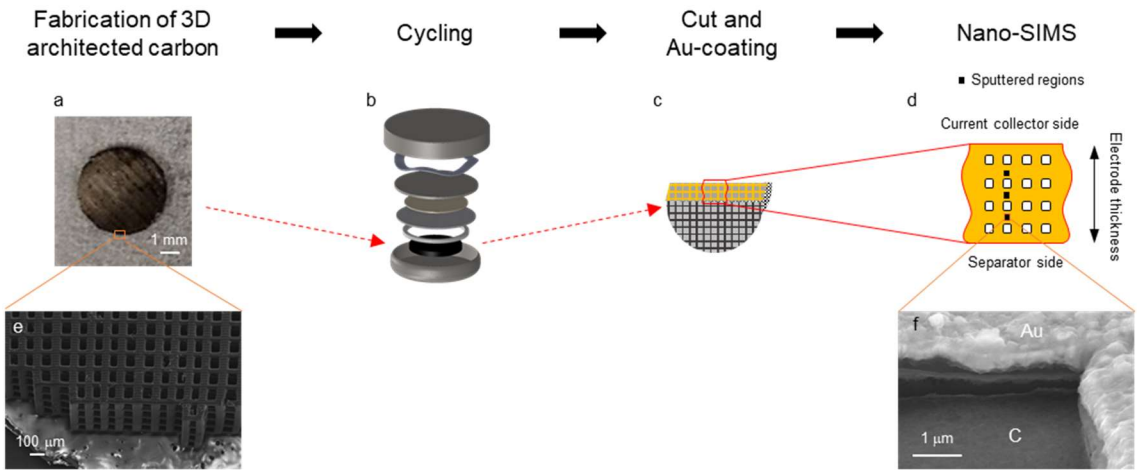

Figure 5. 1 Procedures of characterization of SEI using 3D architected carbon electrodes. (a) A photograph of disk-shaped 3D architected carbon electrode, (b) cycling using a coin cell assembled with a 3D architected carbon electrode and a washer, (c) cycled carbon electrode which is cut into a semi-circle shape and gold-coated, (d) sputtered regions for depth analysis in Nano-SIMS characterizations, SEM images of (e) 3D architected carbon composed of cuboid unit cells, and (f) a region sputtered through the Au layer to the carbon electrode.

Table 5. 2 The number of samples, categorized by cell-making conditions: the presence/absence of washer and reassembling process. Reassembly indicates that the cell was disassembled after the 24-hour rest and reassembled for galvanostatic cycling. One sample assembled without a washer and reassembling process was discharged (i.e., lithiated) before SIMS analysis.

	Without washer	With washer
Single assembly	N = 5 (2* for SIMS)	N = 2 (1 for SIMS)
Reassembly	N = 1	N = 2 (2 for SIMS)

5.3. Galvanostatic Cycling and Capacity Loss

Figure 5. 2 illustrates electrochemical characterization results obtained by galvanostatic cycling using the 3D architected carbon electrodes with the cell-making condition of a single assembly and a washer. Figure 5. 2a contains discharge and charge profiles of the first cycle at 50 mA g^{-1} and the subsequent ten cycles at 200 mA g^{-1}. During the first discharge, the voltage dropped up to ~0.2 V, followed by a gradual increase to 0.27 V with 28 mAh g^{-1} at the local maximum. The voltage then gradually decreased, leading to 191 mAh g^{-1} for the first discharge capacity. During the first charge, the voltage increased without an inflection point, which appeared at 0.2 V during the first discharge. The subsequent cycles at 200 mA g^{-1} showed gradual voltage slopes in discharge and charge profiles, typical behaviors for pyrolytic carbon [29,30].

Figure 5. 2b and c display dQ/dV analysis for discharge and charge from second to 11th cycle. The dQ/dV curves for discharge show peaks at ~0.05 V and ~0.22 V at the second cycle, which disappeared gradually over the cycles. The dQ/dV at >0.5 V showed little change over the cycles. During charge, the peak at ~0.78 V for the second cycle shifted to a higher voltage by 0.14 V at 11th cycle. The peak height gradually decreased from 1.1 mAh V^{-1} to 0.69 mAh V^{-1} during cycling. The dQ/dV for charging at >1.2 V showed little change from the second to 11th cycles.

Figure 5. 2d shows capacities and Coulombic efficiencies over cycling. Discharge and charge capacities at the first cycle were 191 mAh g^{-1} and 143 mAh g^{-1} with 75.2 % of Coulombic efficiency. The subsequent cycles at higher currents, 200 mA g^{-1}, showed reduced capacities, 93 mAh g^{-1} for the second discharge capacity. The rate performance was limited by diffusion in an electrode, as we discussed in Chapter 4. The capacities decreased over the cycles to 53 mAh g^{-1}. The Coulombic efficiencies were 87.0 % for the second reached ~100 % from the third cycle.

To estimate SEI growth from capacities that obtained galvanostatic cycling, we defined two indicators. First, we defined the difference between discharge and charge capacities at each cycle Q_{irr}:

$$Q_{irr}^{x} = Q_{dchg}^{x} - Q_{chg}^{x}. \tag{5.1}$$

Here, the superscript x indicates a cycle number, and capacity with the subscript "dchg" indicates discharge capacity, "chg" indicates charge capacity, and "irr" indicates an irreversible capacity loss. The irreversible capacity loss, Q_{irr} has been commonly used to estimate SEI formation and growth [2,9–11]. The underlying assumption is that capacity loss between discharge and charge is due to irreversible SEI formation, which consumes electrolyte and Li-ions. Figure 5. 2e shows the change of Q_{irr} over the cycles. The Q_{irr} decreases over the cycles and reaches approximately zero at the third cycle.

For the second indicator, we defined capacity loss ΔQ for second to 11th cycle as the difference of capacity at each cycle from the last cycle:

$$\Delta Q_{\alpha}^{x} = Q_{\alpha}^{x} - Q_{\alpha}^{last} \tag{5.2}$$

where subscript α can be discharge or charge, "last" indicates the last cycle (i.e. 11th cycle), and x ranges 2 to 11. ΔQ can be interpreted as an integral of difference of dQ/dV between the last cycle and the cycle of interest within the range of operated voltages (0.005 to 2 V). The concept of ΔQ for SEI growth was demonstrated by Attia [31] with assumptions that

storage mechanism and capabilities are consistent over cycles, and the SEI growth approaches zero as the cycle goes because of the rate-limiting transport mechanism for SEI growth [31,32]. Figure 5. 2f shows the change of ΔQ over cycles. ΔQ decreases with the cycle number from ~0.27 mAh, linearly from sixth cycle with the slope of 0.016 mA cycle^{-1}.

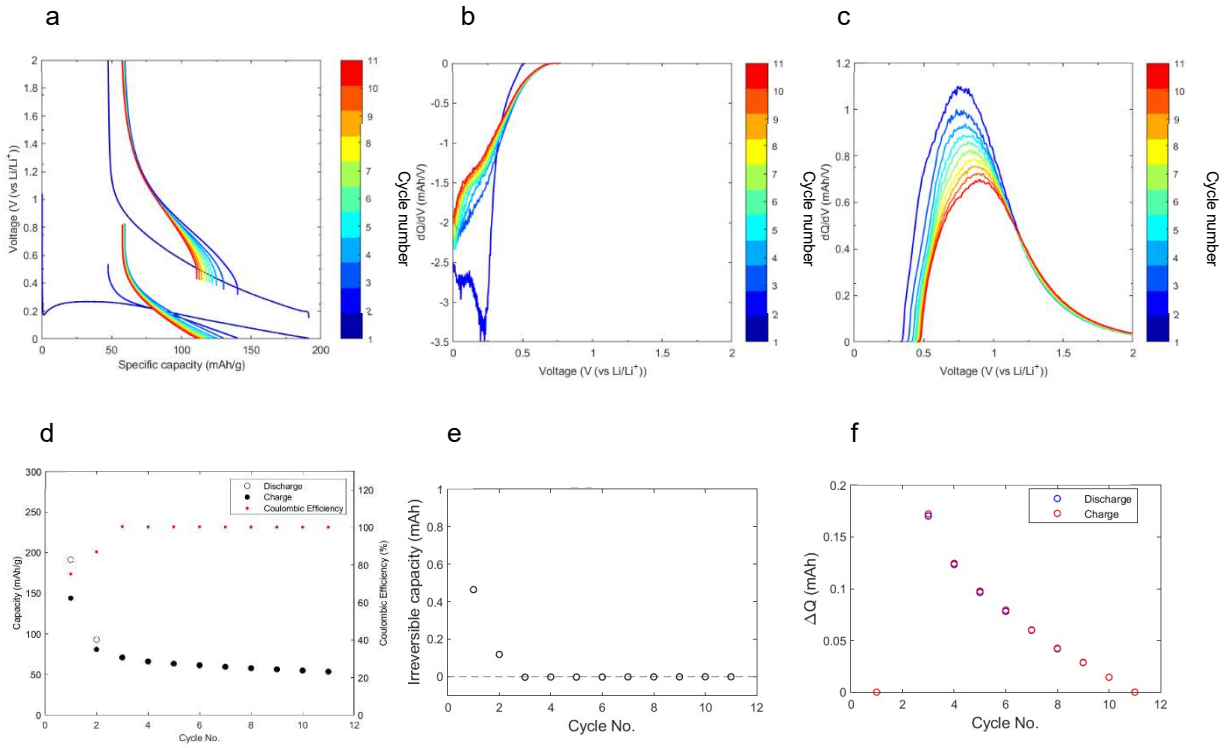

Figure 5. 2 Representative electrochemical characterization results with 3D architected carbon electrodes using galvanostatic cycling. (a) Discharge and charge profiles at 50 mA g^{-1} for the first cycle, and 200 mA g^{-1} for the following 10 cycles. (b) dQ/dV vs voltage curves from 2nd to 11th cycles for discharge process, and (c) charge process.
(d) Discharge capacity, charge capacity, and Coulombic efficiency vs cycle number. (c) Irreversible capacity, Q_{irr} vs cycle number. (d) ΔQ vs cycle number for discharge and charge processes.

5.4. Impedance Measurement by AC and DC

Electrochemical Impedance Spectroscopy

Figure 5. 3 shows representative Nyquist plots of PEIS obtained after the first cycle and 11th cycle for the sample with a single assembly and a washer. Two depressed semi-circles with characteristic frequencies of ~10^2 Hz (middle frequency) and ~10^0 Hz (low frequency), and the Warburg effect associated with diffusion were observed. Some samples show a small semi-circle at high frequencies, ~ 10^3 Hz, overlapped with the semi-circle associated with ~10^2 Hz. These frequency ranges, which represent underlying kinetics, agree with previous studies using a half-cell of carbon and Li electrodes [33]. We employed the equivalent circuit models shown in Figure 5. 13 to obtain resistances and capacitances attributed to different kinetics. The first parallel circuit associated with high frequencies (~10^3 Hz) is attributed to the conductance between 3D architected carbon and a coin cell case; the second parallel circuit at middle frequencies (~10^2 Hz) represents the influence of the SEI layer; the third parallel circuit at low frequencies (~10^0 Hz) represents the charge transfer reactions. The obtained resistances of SEI (R_{SEI}) and charge transfer (R_{CT}) are used to evaluate SEI formation and resistance evolutions in a later section.

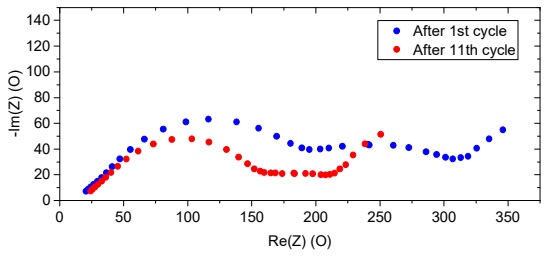

Figure 5. 3 Nyquist plots of PEIS conducted after the first cycle and 11th cycle using a half-cell composed of Li metal and 3D architected carbon electrode

Direct Current Spectroscopy (DCS)

To evaluate resistance evolution *in operando* without relaxing polarizations in an electrolyte, which is necessary for EIS, we developed a new direct current (DC)-based technique that can measure resistance attributed to the dynamic response at different time constants. This technique, which we coin as *DCS (direct current spectroscopy)*, monitors potential response to constant current and analyzes it with time constants of dynamics of interest. The constant current can be integrated into galvanostatic cycling or independently applied as a pulse current. In this chapter, we integrated the DCS technique into galvanostatic cycling. The details and validations of the DCS technique are described in the Appendix E, but we briefly summarize the concept and advantages of the DCS technique. The DCS technique with a pulse current is capable of detecting the resistance anisotropy that emerges when the direction of the applied current is reversed, distinguishing between the forward and reverse applied currents. The resistance evolution is obtained by dividing the overpotential at each given time by the applied current, analogous to the impedance evolution obtained by EIS. The Bode magnitude plots obtained by DCS and galvanostatic EIS (GEIS) show good agreement. This DCS technique acquires data up to the time constant of the dynamic process of interest, which renders it significantly more efficient than EIS, which requires measurements at different frequencies separately.

Figure 5. 4 illustrates the results of integrating the DCS method in galvanostatic cycling for the sample with a single assembly and a washer. Figure 5. 4a and b show voltage change up to 0.5 s during discharge/charge cycles, extracted from Figure 5. 2a. Resistance evolutions were calculated by dividing overpotentials by the applied currents, as shown in Figure 5. 4c. Figure 5. 4d shows Bode amplitude plots, converted from Figure 5. 4c by using $\tau = 1/2\pi f$, where τ indicates time constant, and f indicates frequency. The Bode amplitude plots in Figure 5. 4d show the change of resistance evolutions, which can be attributed to dynamics with different time constants during cycling.

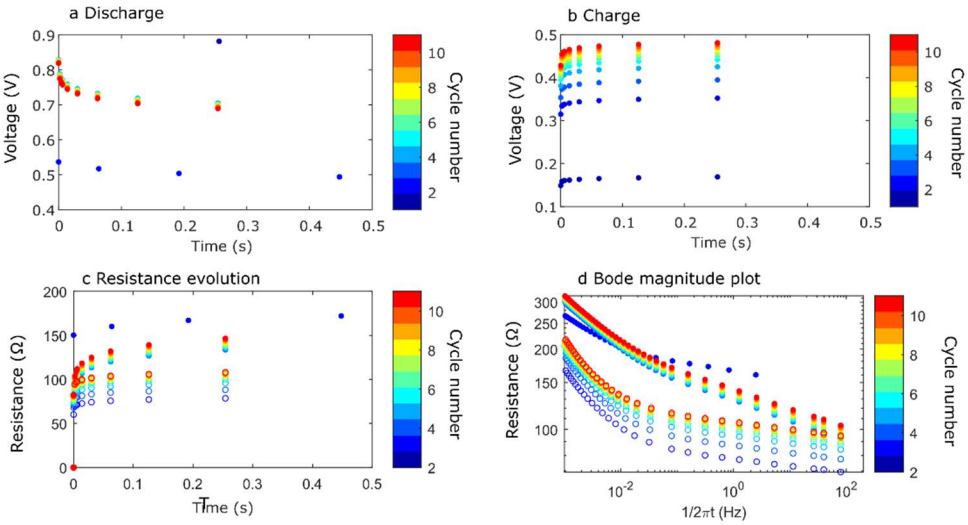

Figure 5. 4 Incorporation of the DCS technique in galvanostatic cycling at 50 mA/g for 1st cycle and 200 mA/g for the following 10 cycles with Li-3D carbon half cell. Voltage changes in (a) discharge cycle and (b) charge cycle over the time since the discharge/charge current applied, (c) resistance evolutions, calculated by dividing voltages by the magnitude of the applied current, and (d) Bode magnitude plots of (c). The closed and open circles show discharge and charge cycles, respectively, in (c) and (d). The color bars on the right in each figure show the cycle number.

To quantify evolving resistances associated with different time constants or frequencies, we distinguished the voltage responses into two kinetics [33]: (1) resistance contributed from SEI and contact, the measured resistance at 80 Hz, and (2) charge transfer resistance, the resistance evolved from 80 Hz to 0.8 Hz, the frequency around the inflection point in Figure 5. 4d. Figure 5. 5 shows these distinguished resistances for discharge and charge cycles. The "discharge" indicates the response to the discharge current (i.e. lithiation) at the delithiated state, and the "charge" indicates the response to the charge current (i.e. delithiation) at the lithiated state. The charge transfer resistance for lithiation increased up to the third cycle and then became stable with ~42 Ω. The SEI resistances for lithiation decreased to 92 Ω until the third cycle and increased by 12 Ω until the 11h cycle. The resistance of charge transfer and SEI for delithiation showed a similar trend with smaller values than the ones for lithiation. This trend indicates that stable SEI, which facilitates charge transfer reaction, was formed up to the third cycle and continuous SEI growth increased SEI resistance after the third cycle. The observed behavior agrees with capacity loss in Figure 5. 2e and f, negligible irreversible capacity at the third cycle, and continuous capacity loss ΔQ even after the third cycle.

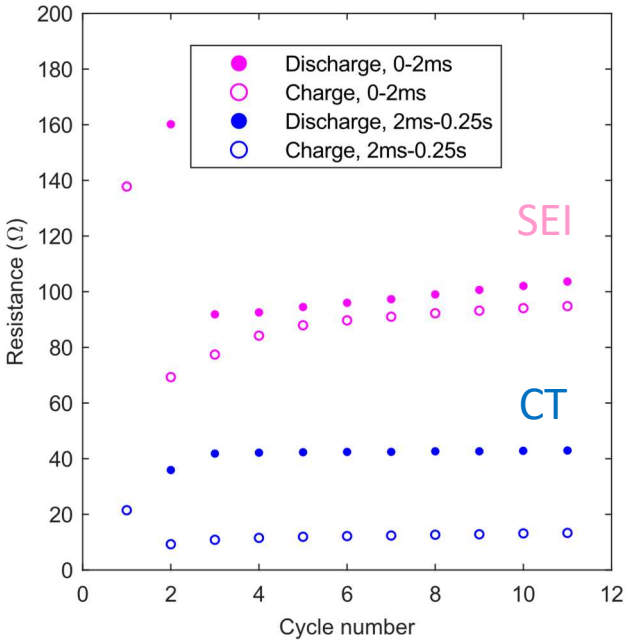

Figure 5. 5 Resistance changes over the cycle, measured from overpotential at 80 Hz (~0.2 ms), attributed to solid electrolyte interphase (SEI) resistance, and from overpotential evolution from 80 Hz (~0.2 ms) to 0.8 Hz (0.25 s), attributed to charge transfer (CT) resistance in Figure 5. 4d.

5.5. SIMS Structural Analysis for SEI

Depth profiles of SEI by SIMS

Figure 5. 6 shows depth profiles of SEI formed on the 3D architected carbon sample cycled with a washer and single assembly. Secondary ions of 7Li, 12C, 16O1H, 19F, 31P, and 197Au were collected simultaneously while Cs^+ primary ion beams sputtered the sample surface, which provided intensity profiles as a function of sputtering time. These depth profiles allowed us to distinguish SEI region and the carbon electrode region, as depicted above the depth profiles in Figure 5. 6. The depth profile of C shows a plateau after 8000 seconds of sputtering time, where the profiles of other secondary ions declined. These results indicate that the plateau region of C corresponds to the carbon electrode, and the profiles before the C plateau correspond to SEI. The exponential decrease of intensities in the carbon

electrode may be due to mixing into the carbon region [34]. The profiles of F and P showed a similar trend from the carbon electrode to the topmost surface. The F and P profiles showed the peak around the interface of SEI and the carbon electrode, followed by a low-intensity plateau to the sputtering of 5000 seconds and an intensity increase by x10. The profiles then decreased gradually up to ~1300 seconds and showed a gradual increase toward the surface. The profiles of Li and O showed plateau throughout SEI and a small bump closer to the surface. The profile of Au showed two plateaus with ~10^4 counts from the topmost to ~1100 seconds and with ~10^6 counts throughout the SEI region.

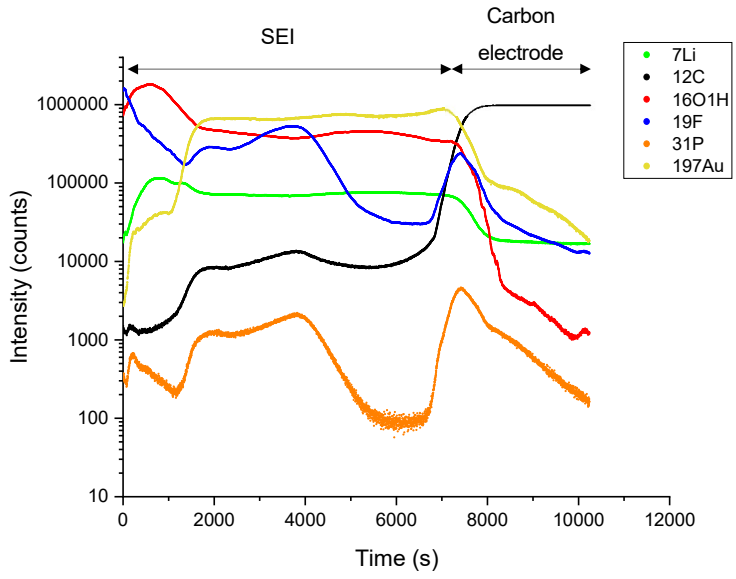

Figure 5. 6 Depth profiles of SEI on an architected carbon electrode.

Estimation of Li Concentrations in Carbon Electrodes and SEI

To quantify Li concentration in carbon and SEI, we estimated the amount of inserted Li in the carbon electrode from the discharge capacity and compared it with the intensity profile obtained from SIMS. One selected 3D architected carbon electrode was discharged at 20 mA g^{-1} after the 11 cycles. Assuming that all the discharge capacity, 1.18 mAh, was used for Li insertion, we calculated the amount of inserted Li, n (mol) with Faraday's law:

$$n = \frac{Q}{Fv} \tag{5.3}$$

where Q indicates the charge (mAh), F indicates Faraday constant (mAh mol^{-1}), and v indicates the valence. The obtained n is divided by a sample volume to calculate Li concentration (mol cm^{-3}) using the 1.8 g cm^{-3} of material density for pyrolytic carbon and mass of the sample. Separately, we calculated the concentration of Li in the carbon from the SIMS results. The amount of Li in carbon was obtained by an integral of SIMS intensity profile of Li in the carbon electrode region, and the sputtered volume was estimated from the collection area (1.4 × 1.4 μm^2) and sputtered depth, which was calculated from sputtering time and estimated sputtering rate in the carbon region (0.25 nm/s, detailed description for estimating sputtering rate in Appendix F). These calculations provide Li concentration in SEI with the unit of count·s cm^{-3}. By equating the concentration of the inserted Li in carbon calculated by independently electrochemical characterization and SIMS with the different units (i.e. mol cm^{-3} vs count·s cm^{-3}), we can obtain a conversion factor from count·s to mol for estimating Li concentration from the SIMS intensity profile. By assuming the sputtering yield of Li as 7Li is consistent in the matrices of carbon and SEI, we can use the obtained conversion factor to estimate Li concentration in SEI from the SIMS results.

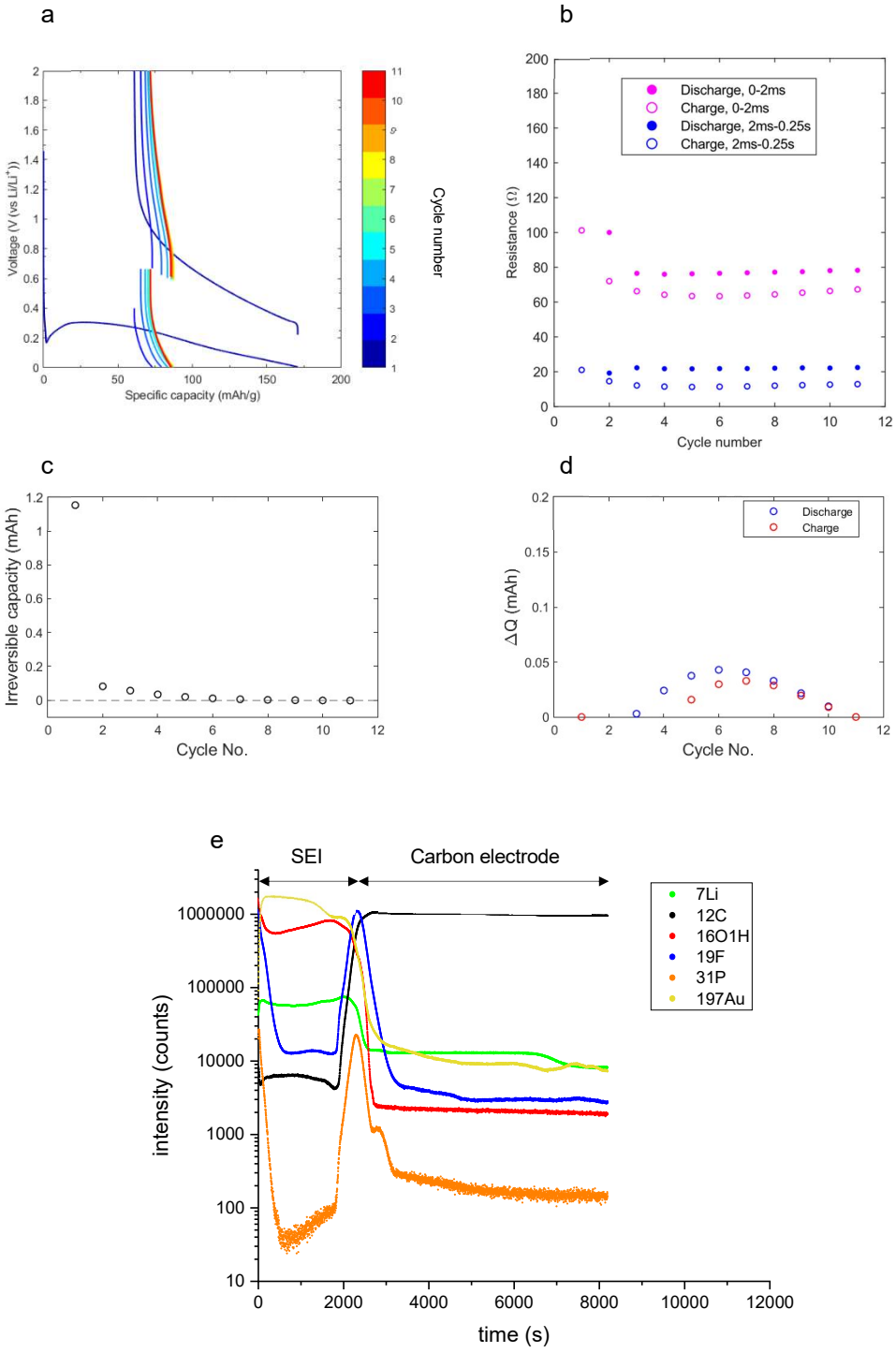

Figure 5. 7 Electrochemical and SIMS results representing cells reassembled with a washer. (a) Discharge and charge profiles of galvanostatic cycling, (b) resistance changes attributed to SEI and charge transfer over the cycle obtained from

DCS technique, (c) ΔQ vs cycle number, (d) Q_{irr} vs cycle number, (e) depth profiles at the position close to separator obtained by SIMS.

5.6. Electrochemical Estimation of SEI Growth and Resistance Evolutions

To investigate the relationship between cycling and SEI growth, we estimated Li concentrations in SEI with three different approaches. The SIMS depth profiles of 7Li with the conversion factor discussed in the previous section provide an estimation of Li concentration in SEI. Electrochemically, Li concentration in SEI can be estimated from the total irreversible capacity losses ΣQ_{irr} (Eq. 5.1) or the total capacity losses $\Sigma\Delta Q$ (Eq. 5.2) by using Faraday's law (Eq. 5.3). The total capacity losses $\Sigma\Delta Q$ were calculated by summing ΔQ from second to the tenth cycle plus $Q_{irr}^{1}$to take into account SEI formation in the first cycle. These independently estimated Li concentrations were compared in Figure 5. 8a and b. The Li concentration calculated using ΣQ_{irr} shows negligible correlation with Li concentration estimated from SIMS results with 0.0243 of the coefficient of determination, R^2. In contrast, the Li concentrations estimated from SIMS and the total capacity losses $\Sigma\Delta Q$ showed strong positive and linear correlation ($R^2 = 0.9669$) and same order of magnitude agreement (slope = 7.19).

Figure 5. 8c and d compare total irreversible capacity losses ΣQ_{irr}, total capacity losses $\Sigma\Delta Q$, and the resistance of SEI, R_{sei} obtained from EIS after the 11th cycle. Both capacities losses and resistances are normalized by a total surface area. Relationship between ΣQ_{irr} and R_{sei} was negative with R^2 = 0.6031. Without considering the sample with washer and reassembly, the correlation was slightly improved to R^2 = 0.7633. The correlation between $\Sigma\Delta Q$ and R_{sei} was not observed with considering all the samples (R^2 = 0.0266). The negligible correlation was due to the samples with washer and reassembly, which showed a capacity increase to four cycles and nonzero irreversible capacities up to six cycles, not observed in other types of samples (Figure 5. 7). The SIMS depth profiles also showed a one-layer SEI structure similar to the inner layer of SEI formed on the sample with a washer and single assembly (Figure 5. 6). By excluding the sample with a washer and reassembly, which

showed different SEI growth behavior than others, the correlation was remarkably improved to R^2 = 0.8178.

The interesting discovery in this work is that $\Sigma\Delta Q$, rather than ΣQ_{irr} shows a strong linear correlation with Li concentrations in SEI, which was estimated by the SIMS results. To the best of our knowledge, there is little experimental evidence in the literature that demonstrate any capacity losses, including irreversible capacity loss, Q_{irr} obtained from electrochemical measurements are correlated with SEI structure, including thickness obtained by non-electrochemical characterizations, especially for post-first-cycle. The recent study by Huang shows that ~5 nm-thick SEI formation on carbon black electrodes observed by cryo-TEM after 20 cycles at C/10 is consistent with a simple geometric estimate of SEI growth using cumulative irreversible capacities ΣQ_{irr} excluding the Q_{irr} at the first cycle. However, they observed ~2nm-thick SEI after the first cycle and heterogeneous SEI growth such as ~100 nm-thick SEI for the same sample [17]. This indicates that Q_{irr} may not capture ~3nm SEI growth and growth of extended SEI. Nevertheless, Q_{irr} is used as a common indicator for SEI growth, because Q_{irr} at the first cycle shows a good correlation with surface area of carbon electrodes [9], and cumulative irreversible capacities ΣQ_{irr} follows time$^{0.5}$ scaling [11,12], which represents transport-limited surface layer growth. In this work, the electrochemical characterizations using the sample with a single assembly and a washer showed that Q_{irr} reached almost zero (Figure 5. 2e) and the resistance of charge transfer decreased to the stable value at the third cycle (Figure 5. 5), indicating that ΣQ_{irr} is used to form SEI that facilitates charge transfer Li-insertion/deinsertion reactions. However, further increase of resistance SEI after the third cycle was not captured by Q_{irr}. where subscripts d and c indicate discharge and charge, t_d and t_c indicate the time that takes the discharge/charge process, and i^c and i^{sei} indicate a current that is used for intercalation/deintercalation and SEI formation.

In contrast, ΔQ considers the SEI formation during both discharge and charge (Eq. (5.2)). The 3D architected carbon electrodes showed similar ΔQ between discharge and charge at each cycle (Figure 5. 2f). Attia found that SEI growth on carbon black electrodes is

significantly higher on lithiation (discharge) than on delithiation (charge) for the second cycle [31,35]. They attribute the observed asymmetry in SEI growth to the change of electronic conductivity of the SEI as a mixed ion-electron conductor that varies electronic conductivity with the square of the local lithium concentration in SEI. They observed SEI thickness by cyro-TEM, which ranged 2-5 nm, within the range of electron-tunneling length [17]. The SEI thickness on the 3D architected carbon electrodes after 11 cycles ranged from ~200 nm to ~1000 nm (Figure 5. 9c, discussed later), which is unlikely limited by electron transport. In addition, the depth profiles of Li at different positions in 3D architected carbon electrodes along electrode-thickness direction revealed that Li remained more in the carbon electrode as closer to the separator side, which may result from polarization in an electrolyte and electrode diffusion-limited rate performance of the 3D carbon electrodes. The gradation of local potentials or state of charge in electrodes was proposed by 3D simulations for thick electrodes [36]. The remained Li in the carbon electrode after the last charge process indicates that local potentials closer to the separator side may be maintained below the stability window of the electrolyte during charge, which leads to continuous SEI growth in both discharge and charge cycles [37].

Other factors that have an influence on the estimation of SEI growth by ΔQ include storage capability change as distinctly seen by revisiting the definition of ΔQ:

$$\Delta Q_\alpha^x = Q_\alpha^x - Q_\alpha^{last}$$
$$= \left(\int_0^{t_{\alpha,x}} |i_\alpha^{c,x}|dt + \int_0^{t_{\alpha,x}} \left|i_\alpha^{sei,x}\right|dt\right) - \left(\int_0^{t_{\alpha,last}} \left|i_\alpha^{c,last}\right|dt + \int_0^{t_{\alpha,last}} \left|i_\alpha^{sei,last}\right|dt\right)$$
$$= \left(\int_0^{t_{\alpha,x}} |i_\alpha^{c,x}|dt - \int_0^{t_{\alpha,last}} \left|i_\alpha^{c,last}\right|dt\right) + \left(\int_0^{t_{\alpha,x}} \left|i_\alpha^{sei,x}\right|dt - \int_0^{t_{\alpha,last}} \left|i_\alpha^{sei,last}\right|dt\right) \quad (5.4)$$

where t_α indicates the time that takes the discharge/charge process, and $i^{c,x}$ and $i^{sei,x}$ indicate a current that is used for intercalation/deintercalation and SEI formation x-th cycle. As we discussed, the concept of ΔQ is built on the assumptions that storage mechanism and capabilities are consistent over cycles (the first and second term are equal in Eq. (5.4)), and

the SEI growth approaches zero as the cycle goes (i.e. $\int_0^{t_{\alpha,last}} \left| i_\alpha^{sei,last} \right| dt = 0$). Possible storage capability loss of carbon electrodes includes contact loss of active materials [38], decreased porosity of electrodes by SEI growth, which limits Li-ion transport in an electrolyte [8], and overpotential increase due to transport through a grown SEI. The contact loss of active materials can be ruled out in this work because the 3D architected carbon electrodes are interconnected and mechanically resilient, unlike slurry electrodes, whose electrical connections are supported by conductive additives and physical contacts by binders. If the contact loss of active materials happened, we would expect a decrease in dQ/dV at all potentials, which was not seen for 3D architected carbon electrodes (Figure 5. 2b and c). The decrease of porosity is also unlikely to affect capacity because the rate performance of the 3D architected carbon electrode is limited by diffusion in electrode rather than in electrolyte (see Chapter 4 for detailed discussion). The influence of SEI growth on overpotential and capacity cannot be ruled out in this work. If the capacity decay occurs due to the overpotential increase by SEI growth, we overestimate SEI growth (i.e. $\int_0^{t_{\alpha,x}} |i_\alpha^{c,x}| dt - \int_0^{t_{\alpha,last}} \left| i_\alpha^{c,last} \right| dt > 0$). Future study with reduced currents, which minimizes overpotential effects on capacities, is necessary for further understanding of the relationship between ΔQ and SEI growth.

The correlations between R_{sei} vs ΣQ_{irr}, and R_{sei} vs $\Sigma \Delta Q$ in Figure 5. 8c and d also provide new insight on an estimation of SEI growth and influence on resistance. ΣQ_{irr} was contributed mostly from the first 3 cycles, in which the charge transfer resistance decreased to the stable value. This result and the weak negative correlation between R_{sei} and ΣQ_{irr} may indicate that the initial SEI formation cycles are important to form "good" SEI that facilitates lithiation/delitation reactions and suppresses the resistance of SEI. Carefully controlled cycling protocol and structure characterization of SEI for the initial cycles may elucidate factors to form "good" SEI.

The strong correlation of $\Sigma \Delta Q$ and SEI resistance if we exclude the sample with washer and reassembly suggests that ΔQ can be a good indicator to estimate the influence of SEI growth

on resistance if we can confirm similar SEI growth behaviors. The depth profiles of the excluded sample were distinct from the others; for instance, SEI was composed of single-layer and thinner than other characterized SEIs. In other words, the structure of SEI may have significant influences on resistance. To understand the structure-property relationship of SEI, we discuss SIMS depth profiles and SEI resistance evolutions in the next section.

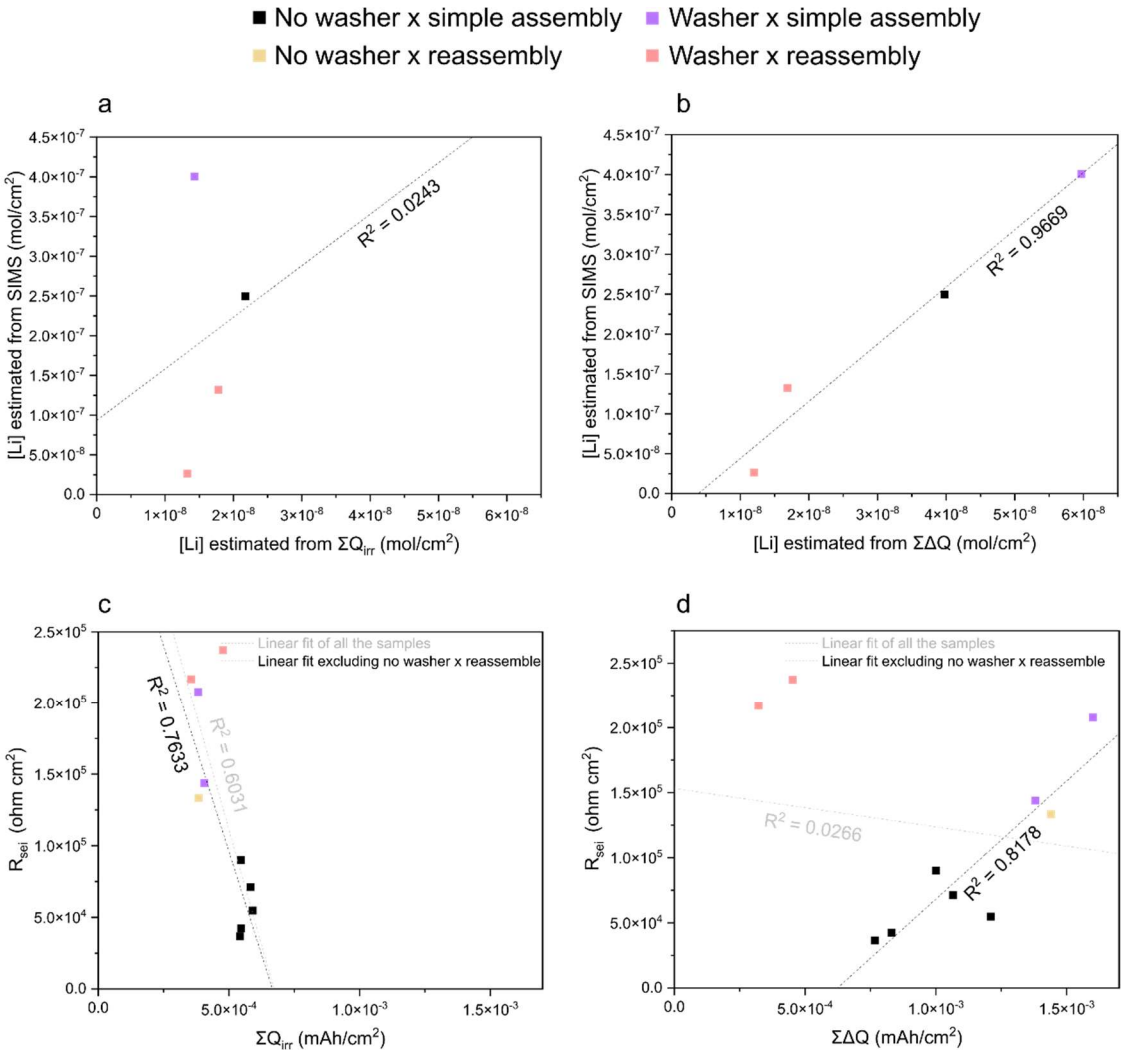

Figure 5. 8 Correlations of Li concentration in SEI estimated from SIMS and cycling, and resistance of SEI obtained from EIS. The Li concentration obtained from SIMS is compared with (a) Li concentration estimated from total

irreversible capacity loss ΣQ_{irr}, and (b) Li concentration estimated from total capacity loss $\Sigma \Delta Q$. The resistance of SEI is compared with (c) total irreversible capacity loss ΣQ_{irr}, and (d) total capacity loss $\Sigma \Delta Q$.

5.7. Structure of SEI and Influences on Resistance

To understand the structure and property relationship of SEI, we compared the SEI thickness, the amount of Li, and the amount of F in SEI with SEI resistance in Figure 5. 9. We chose the amount of F for comparison because F intensities may represent the amount of LiF, which is a major component in SEI [39] and may limit Li-ion transport in SEI because LiF is an ionic insulator as its intrinsic property ($\sim 10^{-13}$ to 10^{-14} S cm^{-1}) [15,16]. A strong correlation was not observed in all comparisons. Resistance of SEI shows weak negative correlation with thickness and positive correlation with F amount and negligible correlation with Li amount. The complexity of SEI in compositions and geometrical structures such as porous outer layer and compact inner layer [40] may be responsible for the observed weak or negligible correlations between resistance and structure "averaged" over through the complex SEI structure.

We calculated the conductivity of SEI from the results of EIS and SIMS, which ranged between 9.8×10^{-11} and 1.4×10^{-9} S cm^{-1}. The accurate conductivity measurement or thickness measurement of SEI is challenging, especially for porous electrodes, because SEI is air-sensitive thin film [19] and forms/grows heterogeneously [17]. Still, the reported conductivity of SEI formed in a cell using liquid electrolyte is within the order of 10^{-7} to 10^{-10} S cm^{-1} [2,13,16], which is consistent with this study.

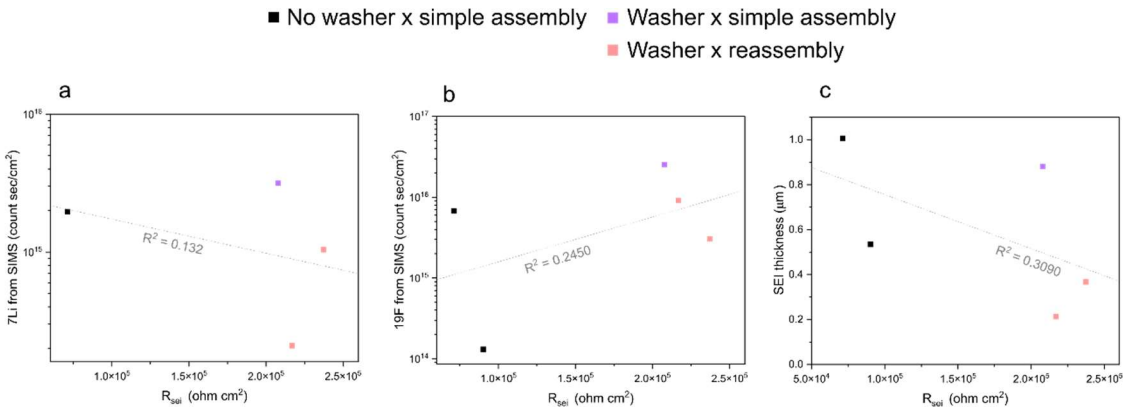

Figure 5. 9 Correlation of the resistance of SEI with total intensities in SEI for (a) 7Li and (b) 19F, and (c) thickness of SEI.

To investigate SEI formation, structure, and resistance in more depth, we compared ΔQ and the change of the SEI resistance at each cycle. Figure 5. 10a plots SEI resistance change obtained by the DCS technique and ΔQ from 3 to 10 cycles. The SEI resistance change linearly decreased with ΔQ up to 4th cycle, close to the cycle number showing the charge transfer resistance become stable (Figure 5. 5). From the 8th cycle, the SEI resistance started increasing despite a decrease of ΔQ. The linear correlation between ΔQ and the SEI resistance change indicates that SEI grows with consistent conductivity (S cm^{-1}), which is often assumed in various battery models, especially the Multiphysics model that aims at simulating overall battery cycling (e.g. Newman's model) [26–28]. Differing from the positive linear relation suggests that SEI growth mechanism or SEI structure changes. This "multi-layer" SEI structure or "multi-mechanism" of transport through SEI has been suggested by modeling [32,41] and demonstrated by experiments, especially for the SEI growth at the first cycle [13,14].

To elucidate potential causes of the accelerated SEI resistance increase after the eighth cycle, we distinguished an integral of the Li depth profile by $\Delta Q^x/\Sigma\Delta Q$ at each cycle from the interface between SEI and the carbon electrode. For $x = 1$, we used $Q_{irr}^1/\Sigma\Delta Q$. We assumed that SEI grows from the topmost surface (i.e. interface between SEI and electrolyte), and ΔQ represents the amount of Li (or electron) used for SEI growth. Figure 5. 10b shows that the Li depth profile is distinguished by each cycle growth. The F depth profile is plotted as well.

The F intensity showed a peak and decreased for the growth at the first cycle. Then, the F intensity rapidly increased, which corresponds to the second cycle, followed by intensity fluctuation, which distinctly divided by the $\Delta Q^x/\Sigma\Delta Q$ for its local maximum and minimum. The last rapid increase of the intensity appeared on the eighth cycle, which agrees with the cycle that started showing accelerated SEI resistance increase despite a decrease of ΔQ (Figure 5. 10a).

The F depth profile distinguished by cycle number and the SEI resistance evolutions may be explained by the current understanding of SEI formation. LiF is formed as a component of SEI on carbon electrodes for the first cycle [10,18,42]. Simultaneously, lithium ethylene dicarbonate (LEDC) and Li_2CO_3 are formed [10,17,18], which agrees with high intensities in the O depth profile (Figure 5. 6). The LEDC is decomposed into various components such as Li_2CO_3 and lithium alkoxide, which may correspond to the low F region. Then, further decomposition of electrolyte happens to form LiF, which is observed as the increase of F in the SIMS depth profile at the growth of the eighth cycle. This suggests that the accelerated SEI resistance increase may be due to LiF formation, which is an intrinsic ionic insulator.

To test the hypothesis that LiF formation during SEI growth has a significant influence on SEI resistance, we compared F concentration in SEI and the SEI resistance increase from the cycle when charge transfer resistance is stabilized to the last cycle (11th cycle). Figure 5. 12 shows that the correlation between an integral of the F depth profile in the SEI region and SEI resistance increase from the cycle that showed stable charge transfer resistance. We averaged the integrals of F intensities obtained at 3 or 5 different positions throughout porous electrodes. The total intensities of F and SEI resistance increase showed a strong linear correlation with $R^2 = 0.999$. In addition, the two samples with washer and reassembly did not show the F plateau in the depth profile (Figure 5. 7). These results agree with our hypothesis, which is LiF formation during SEI growth after achieving stable charge transfer resistance has a significant influence on SEI resistance. Although we found a strong correlation between F intensities and SEI resistance increase, an additional study should be conducted to verify this hypothesis, such as depth analysis by X-ray photoelectron

spectroscopy (XPS) to confirm the presence of LiF. Another possibility of the SEI resistance increase is that tortuous porous SEI structure formation is associated with $LiPF_6$ reduction [21], limiting transport in an electrolyte penetrated in porous SEI.

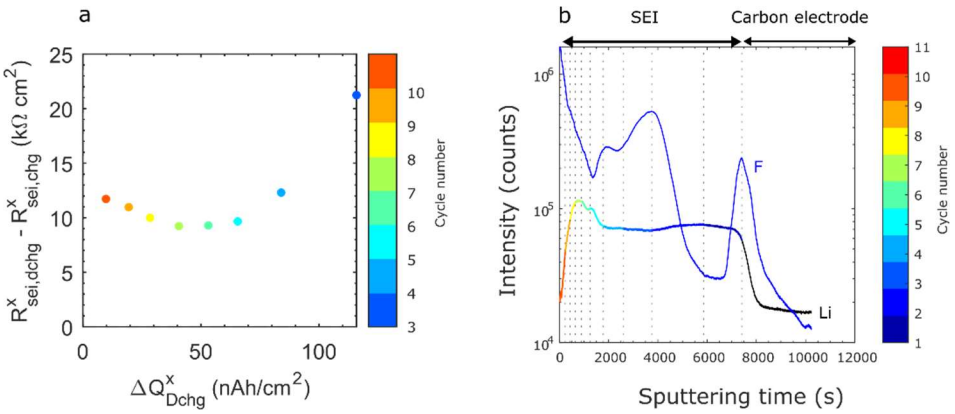

Figure 5. 10 SEI resistance evolutions vs ΔQ for each cycle. (a) SEI resistance evolutions before and after ΔQ_{chg} for each cycle. (b) The representative Li depth profile was distinguished to SEI growth at each cycle by $\Delta Q^x/\Sigma\Delta Q$. F depth profile was plotted together.

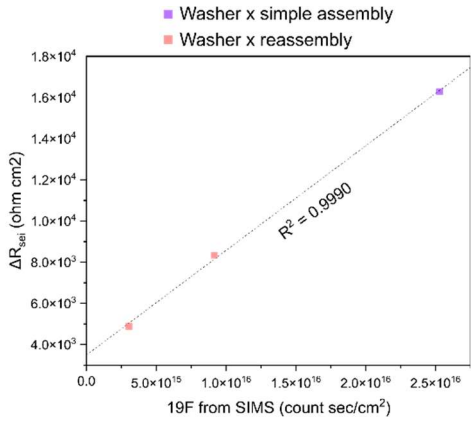

Figure 5. 11 Correlation of the total counts of 19F in SEI from SIMS and resistance increase of SEI after charge transfer resistance is stabilized.

5.8. Position-Dependent SEI Growth

Figure 5. 12 shows the integral of intensities of Li and F in SEI at three sites along the electrode thickness direction from a current collector to a separator. Comparison of these integrals of intensities represents the amount of Li and F in SEI at different positions. The amount of Li in SEI becomes higher toward the separator side, whereas the amount of F in SEI increased toward the current collector side.

Position-dependent SEI growth in porous electrodes has been proposed by numerical simulations using modified Newman's model [26–28]. Previous studies in literature employed the Butler-Volmer equation for a reaction to form SEI with concentrations of solvent (e.g. EC) and Li-ions in an electrolyte, and linear resistance increase of SEI with increasing the thickness [26–28]. The common outcome is that the SEI growth rate is higher toward the separator side because of the concentration gradient in an electrolyte, which leads to uneven resistance increase. In this study, we experimentally confirmed that the amount of Li in SEI, representing the outcome of SEI growth rate, increased toward the separator side, which agreed with the numerical simulation results. In addition, this study shows the opposite tendency of the F amount, which was higher toward the current collector side. As we discussed in the previous section, the amount of F in SEI may significantly influence SEI resistance, which implies that position-dependent SEI resistance may increase toward the current collector side. This implication contradicts the numerical model results about position-dependent SEI growth and influence [26–28] because these models do not take into account the structure-property relationship of multi-layer SEI (i.e. assuming consistent conductivity of SEI.) Overall, this study suggests that position-dependent SEI growth and influence may not be estimated precisely or even estimated in a mistaken way if it does not consider the structure-property relationship of multi-layer SEI.

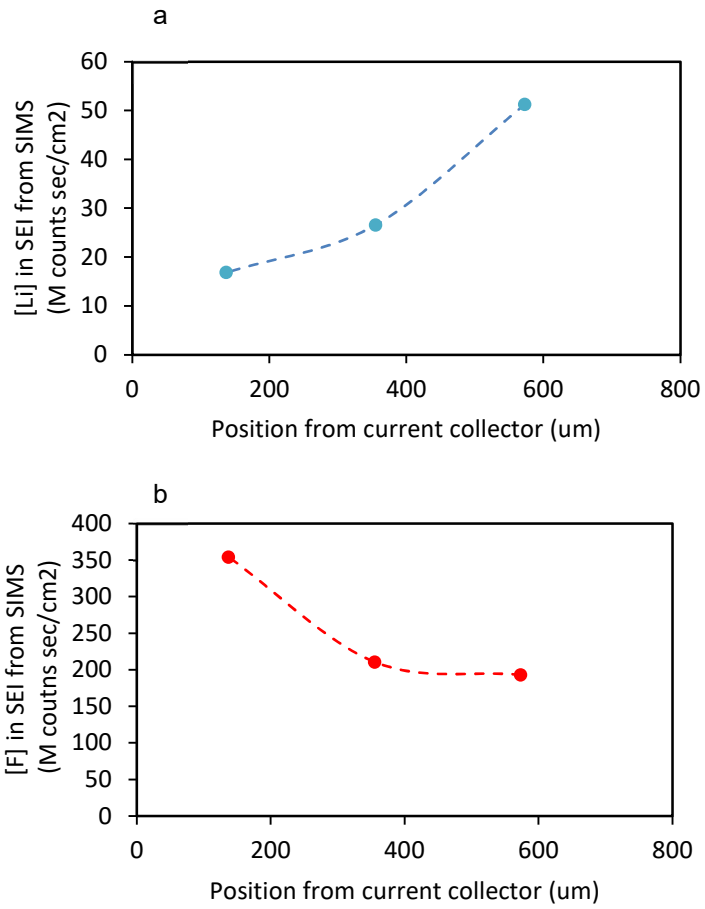

Figure 5. 12 Position-dependent SEI growth with the compositions of Li and F. The integrals of intensities of (a) Li and (b) F in SEI, at different positions on the cross-section of 3D architected carbon electrode. The dot lines are for visual guidance. The sample was made by a single assembly with a washer.

5.9. Summary and Outlook

The thick 3D architected carbon electrodes were used to study the formation and growth, structure-property relationship, and position-dependent growth of SEI through porous electrode with *in operando* DCS technique to evaluate resistance evolutions and Nano-SIMS to acquire depth profiles. We discovered that Li consumption estimation using ΔQ showed a stronger linear correlation than Q_{irr} with the Li amount in SEI obtained by SIMS. ΔQ shows similar values between discharge and charge because the remained Li in the carbon electrode

due to polarization in the electrolyte may result in maintaining local potentials low enough to cause electrolyte reduction during charge. The sum of ΔQ showed a good correlation with the SEI resistance. Distinguishing Li depth profiles by SIMS by $\Delta Q^x/\Sigma\Delta Q$ SEI to estimate SEI growth at each cycle showed a good agreement of the accelerated SEI resistance and F intensity rapid increase. The total F intensities in SEI and the resistance increase from the cycle that showed stable charge transfer resistance showed a strong linear correlation. These results indicate that F increase, which may be attributed to LiF, an intrinsic Li-ion insulator, significantly influences SEI resistance increase. The position-dependent SEI growth, higher Li amount toward the separator side was confirmed in this study. In addition, the total counts of F in SEI showed the opposite trend to the Li intensities, which implies that local SEI resistance may be higher toward the current collector side, with the consideration of the strong correlation of F intensity and SEI resistance. This implication contradicts the estimation of SEI resistance distribution by Newman's model if the multi-layer SEI model is not considered for the concentration.

This study provides a couple of arguments: the concept of ΔQ, LiF influence on SEI resistance increase, and position-dependent SEI resistance with the consideration of LiF formation. Each argument must be tested with rigorous experiments. The difference in SEI growth, structure, and resistance on 3D architected carbon samples manufactured under the same conditions in this study was attributed to coin cell assembly methods: the presence/absence of a washer and the single assembly/reassembling process. The washer may release adsorbed water in a coin cell, potentially resulting in more F intensities than other types of samples [21]. Similar observations of the suggested aging mechanism in this study may emerge more often when thick electrodes with high currents are investigated for their cycle life – current investigations on SEI and aging are focused on commercial thin slurry electrodes and thin film electrodes.

5.10. Detailed Experimental Procedures

Electrode preparation and galvanostatic cycling

The fabrication and coin cell making procedures for 3D architected carbon electrodes were described in Chapter 2 and Chapter 3. Disk-shaped structures composed of cubic unit cells with a diameter of 37 mm and porosity of 70% are printed. The printing direction was parallel to the diameter of the disk, which allows characterizing a flat surface of cross-section without wave features attributed to printing layers. The pyrolyzed 3D carbon and Li metal half cells with 1M $LiPF_6$ in 1:1 (v/v) ratio of EC: DEC were assembled using a 2032 coin cell. Galvanostatic cycling tests were conducted using the assembled coin cells by a battery cycling system (BCS-805, Biologic) at room temperature. Open-circuit voltage was applied for more than four hours before starting cycling tests to obtain equilibrium. The first galvanostatic cycling was conducted at 50 mA g^{-1} with a 10-second open-circuit voltage interval, followed by a 12-hour open-circuit voltage. Then, potentiostatic electrochemical impedance spectroscopy was conducted with 5 mV of potential perturbation from 10 kHz to 3mHz. After another 12-hour open-circuit voltage, galvanostatic cycling was conducted for ten cycles at 200 mA g^{-1} with a 10-second open-circuit voltage interval before switching current directions. Another 12-hour open-circuit voltage is then applied, and PEIS was conducted with the same conditions described before. For all galvanostatic cycling tests, cut-off voltages were set at 2 V and 0.005 V. The potential was recorded with a geometric time resolution starting from 2 ms unless otherwise noted. The overpotential was measured as the voltage change from the open-circuit potential right before the cycle. To investigate overpotential change, we set the time when an applied current was first recorded as $t = 0$.

One 3D architected carbon electrode underwent a half discharge cycle at 20 mA g^{-1} after all the cycling and EIS processes to fully lithiate the carbon electrode for estimating Li-ion concentrations in carbon.

Equivalent circuit models as illustrated in Figure 5. 13 were used to fit Nyquist plots and extract resistance and capacitance values. The fitting was conducted with Simplex algorithm

using EC-Lab Software (Biologic). The model of Figure 5. 13b is used for some samples that showed the small semi-circle at high-frequency in the Nyquist plot. To normalize resistance, capacitance, and capacity, we used a total surface area calculated by the BET specific surface area (15 m^2 g^{-1}) and a measured mass of 3D architected carbon.

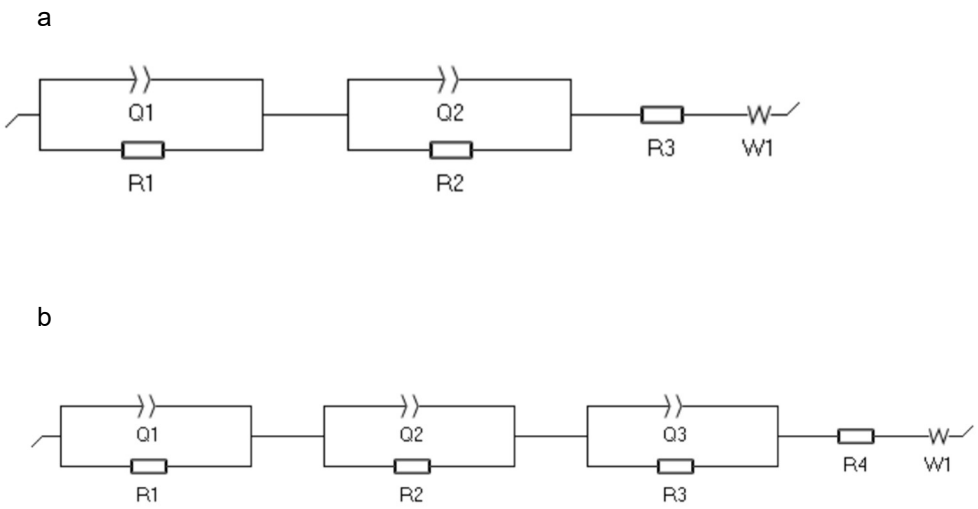

Figure 5. 13 Equivalent circuits models used for half-cell of 3D carbon and Li, used for (a) the Nyquist plot without high-frequency semi-circle, and (b) the Nyquist plot with a high-frequency semi-circle.

Sample preparation for SIMS analysis

After the galvanostatic cycling, we disassembled a coin cell in the Ar-filled glovebox with the caution not to deform the 3D architected carbon electrodes. The cycled 3D architected carbon was rinsed in 200 μL of dimethyl carbonate (DMC) for less than 10 s to remove residual electrolyte [43], and then dried at room temperature inside the glovebox overnight. The dried sample was cut into a semi-circle shape by a razor blade. The cross-section was coated with gold using a sputter coater (108Auto, Cressington) using a gold target to prevent direct air exposure during transferring from the glovebox to a SIMS instrument (NanoSIMS 50L, CAMECA). The Au-coated samples were mounted on a custom-holder that allows facing the cross-section of the semi-circle sample top, the orientation to an ion detector in

SIMS. The transferring time from an air-tight container (SampleSaver, South Bay Technology) to the SIMS instrument was minimized up to 10 seconds.

SIMS analysis and EDS

The depth profiles were acquired with a Cameca NanoSIMS 50L ion microprobe. An 8 keV Cs^+ primary beam of ~ 100-200 nm was used to sputter the sample in a rastering mode. The primary beam current and rastered area were 15 pA in 5x5 mm or 4pA in 3x3 mm. Secondary ions (7Li, 12C, 16O1H, 19F, 31P, and 197Au) of -8 keV were simultaneously collected with electron multipliers (EMs). To avoid the edge effect during the sputtering, secondary signals were only collected from the center 2.3x2.3 mm of the 5x5 mm or 1.4x1.4 mm of the 3x3 mm crater with electronic gating. The total data acquisition time on each profile lasted from about 1 to 3 hours. The mass spectrometer was set at high mass resolution conditions to remove possible interferences for the masses of interest.

Depth analysis was conducted for the Au-coated 3D architected carbon without cycling to investigate Au-mixing effects during sputtering and estimate the sputtering rate in carbon. After the SIMS analysis, the sputtered regions were analyzed by SEM (Versa 3D Dual Beam, FEI) equipped with energy-dispersive spectroscopy (Quantax EDS, Bruker). Line analysis was conducted on the cross-section of sputtered regions to measure the depth of sputtered SEI and a carbon electrode.

REFERENCES

1. Edge, J.S.; O'Kane, S.; Prosser, R.; Kirkaldy, N.D.; Patel, A.N.; Hales, A.; Ghosh, A.; Ai, W.; Chen, J.; Yang, J.; et al. Lithium ion battery degradation: What you need to know. *Phys. Chem. Chem. Phys.* **2021**, doi:10.1039/D1CP00359C.

2. Peled, E.; Menkin, S. Review—SEI: Past, present and future. *J. Electrochem. Soc.* **2017**, *164*, A1703–A1719, doi:10.1149/2.1441707jes.

3. Guo, J.; Sun, A.; Chen, X.; Wang, C.; Manivannan, A. Cyclability study of silicon-carbon composite anodes for lithium-ion batteries using electrochemical impedance spectroscopy. *Electrochim. Acta* **2011**, *56*, 3981–3987, doi:10.1016/j.electacta.2011.02.014.

4. Xu, J.; Deshpande, R.D.; Pan, J.; Cheng, Y.-T.; Battaglia, V.S. Electrode side reactions, capacity loss and mechanical degradation in lithium-ion batteries. *J. Electrochem. Soc.* **2015**, *162*, A2026–A2035, doi:10.1149/2.0291510jes.

5. Vetter, J.; Novák, P.; Wagner, M.R.; Veit, C.; Möller, K.C.; Besenhard, J.O.; Winter, M.; Wohlfahrt-Mehrens, M.; Vogler, C.; Hammouche, A. Ageing mechanisms in lithium-ion batteries. *J. Power Sources* **2005**, *147*, 269–281, doi:10.1016/j.jpowsour.2005.01.006.

6. Keil, P.; Jossen, A. Calendar aging of NCA lithium-ion batteries investigated by differential voltage analysis and Coulomb tracking. *J. Electrochem. Soc.* **2017**, *164*, A6066–A6074, doi:10.1149/2.0091701jes.

7. Waldmann, T.; Wilka, M.; Kasper, M.; Fleischhammer, M.; Wohlfahrt-Mehrens, M. Temperature dependent ageing mechanisms in Lithium-ion batteries - A Post-Mortem study. *J. Power Sources* **2014**, *262*, 129–135, doi:10.1016/j.jpowsour.2014.03.112.

8. Atalay, S.; Sheikh, M.; Mariani, A.; Merla, Y.; Bower, E.; Widanage, W.D. Theory of battery ageing in a lithium-ion battery: Capacity fade, nonlinear ageing and lifetime prediction. *J. Power Sources* **2020**, *478*, 229026, doi:10.1016/j.jpowsour.2020.229026.

9. Placke, T.; Siozios, V.; Rothermel, S.; Meister, P.; Colle, C.; Winter, M. Assessment of surface heterogeneity: A route to correlate and quantify the 1st cycle irreversible capacity caused by sei formation to the various surfaces of graphite anodes for lithium ion cells. *Zeitschrift fur Phys. Chemie* **2015**, *229*, 1451–1469, doi:10.1515/zpch-2015-0584.

10. Naoi, K.; Ogihara, N.; Igarashi, Y.; Kamakura, A.; Kusachi, Y.; Utsugi, K. Disordered carbon anode for lithium-ion battery I. An interfacial reversible redox action and anomalous topology changes. *J. Electrochem. Soc.* **2005**, *152*, A1047, doi:10.1149/1.1896531.

11. Smith, A.J.; Burns, J.C.; Zhao, X.; Xiong, D.; Dahn, J.R. A high precision coulometry study of the sei growth in Li/graphite cells. *J. Electrochem. Soc.* **2011**, *158*, A447, doi:10.1149/1.3557892.

12. Attia, P.M.; Chueh, W.C.; Harris, S.J. Revisiting the $t^{0.5}$ dependence of SEI growth. *J. Electrochem. Soc.* **2020**, *167*, 090535, doi:10.1149/1945-7111/ab8ce4.

13. Lu, P.; Li, C.; Schneider, E.W.; Harris, S.J. Chemistry, impedance, and morphology evolution in solid electrolyte interphase films during formation in lithium ion batteries. *J. Phys. Chem. C* **2014**, *118*, 896–903, doi:10.1021/jp4111019.

14. Shi, S.; Lu, P.; Liu, Z.; Qi, Y.; Hector, L.G.; Li, H.; Harris, S.J. Direct calculation of Li-ion transport in the solid electrolyte interphase. *J. Am. Chem. Soc.* **2012**, *134*, 15476–15487, doi:10.1021/ja305366r.

15. He, M.; Guo, R.; Hobold, G.M.; Gao, H.; Gallant, B.M. The intrinsic behavior of lithium fluoride in solid electrolyte interphases on lithium. *Proc. Natl. Acad. Sci. U. S. A.* **2020**, *117*, 73–79, doi:10.1073/pnas.1911017116.

16. Guo, R.; Gallant, B.M. Li2O Solid electrolyte interphase: Probing transport properties at the chemical potential of lithium. *Chem. Mater.* **2020**, *32*, 5525–5533,

doi:10.1021/acs.chemmater.0c00333.

17. Huang, W.; Attia, P.M.; Wang, H.; Renfrew, S.E.; Jin, N.; Das, S.; Zhang, Z.; Boyle, D.T.; Li, Y.; Bazant, M.Z.; et al. Evolution of the solid-electrolyte interphase on carbonaceous anodes visualized by atomic-resolution cryogenic electron microscopy. *Nano Lett.* **2019**, *19*, 5140–5148, doi:10.1021/acs.nanolett.9b01515.

18. Heiskanen, S.K.; Kim, J.; Lucht, B.L. Generation and evolution of the solid electrolyte interphase of lithium-ion batteries. *Joule* **2019**, *3*, 2322–2333, doi:10.1016/j.joule.2019.08.018.

19. Oswald, S.; Hoffmann, M.; Zier, M. Peak position differences observed during XPS sputter depth profiling of the SEI on lithiated and delithiated carbon-based anode material for Li-ion batteries. *Appl. Surf. Sci.* **2017**, *401*, 408–413, doi:10.1016/j.apsusc.2016.12.223.

20. Horstmann, B.; Single, F.; Latz, A. Review on multi-scale models of solid-electrolyte interphase formation. C*urr. Opin. Electrochem.* **2019**, *13*, 61–69, doi:10.1016/j.coelec.2018.10.013.

21. An, S.J.; Li, J.; Daniel, C.; Mohanty, D.; Nagpure, S.; Wood, D.L. The state of understanding of the lithium-ion-battery graphite solid electrolyte interphase (SEI) and its relationship to formation cycling. *Carbon N. Y.* **2016**, *105*, 52–76, doi:10.1016/j.carbon.2016.04.008.

22. Ogihara, N.; Igarashi, Y.; Kamakura, A.; Naoi, K.; Kusachi, Y.; Utsugi, K. Disordered carbon negative electrode for electrochemical capacitors and high-rate batteries. *Electrochim. Acta* **2006**, *52*, 1713–1720, doi:10.1016/j.electacta.2006.01.082.

23. Du Pasquier, A.; Disma, F.; Bowmer, T.; Gozdz, A.S.; Amatucci, G.; Tarascon, J. -M. Erratum: "Differential scanning calorimetry study of the reactivity of carbon anodes in plastic Li-ion batteries" *J. Electrochem. Soc.* **1998**, *145*, 1413–1413, doi:10.1149/1.1838474.

24. Spotnitz, R.; Franklin, J. Abuse behavior of high-power, lithium-ion cells. *J. Power Sources* **2003**, *113*, 81–100, doi:10.1016/S0378-7753(02)00488-3.

25. Harris, O.C.; Tang, M.H. Molecular probes reveal chemical selectivity of the solid-electrolyte interphase. *J. Phys. Chem. C* **2018**, *122*, 20632–20641, doi:10.1021/acs.jpcc.8b06564.

26. Pinsona, M.B.; Bazant, M.Z. Theory of SEI formation in rechargeable batteries: Capacity fade, accelerated aging and lifetime prediction. *J. Electrochem. Soc.* **2013**, *160*, doi:10.1149/2.044302jes.

27. Liu, L.; Park, J.; Lin, X.; Sastry, A.M.; Lu, W. A thermal-electrochemical model that gives spatial-dependent growth of solid electrolyte interphase in a Li-ion battery. *J. Power Sources* **2014**, *268*, 482–490, doi:10.1016/j.jpowsour.2014.06.050.

28. Kindermann, F.M.; Keil, J.; Frank, A.; Jossen, A. A SEI modeling approach distinguishing between capacity and power fade. *J. Electrochem. Soc.* **2017**, *164*, E287–E294, doi:10.1149/2.0321712jes.

29. Alvin, S.; Cahyadi, H.S.; Hwang, J.; Chang, W.; Kwak, S.K.; Kim, J. Revealing the intercalation mechanisms of lithium, sodium, and potassium in hard carbon. *Adv. Energy Mater.* **2020**, *10*, 1–16, doi:10.1002/aenm.202000283.

30. Dahn, J.R.; Zheng, T.; Liu, Y.; Xue, J.S. Mechanisms for lithium insertion in carbonaceous materials. *Science* **1995**, *270*, 590–593, doi:10.1126/science.270.5236.590.

31. Attia, P.M.; Das, S.; Harris, S.J.; Bazant, M.Z.; Chueh, W.C. Electrochemical kinetics of SEI growth on Carbon Black: Part I. Experiments. *J. Electrochem. Soc.* **2019**, *166*, E97–E106, doi:10.1149/2.0231904jes.

32. Single, F.; Horstmann, B.; Latz, A. Revealing SEI morphology: In-depth analysis of a modeling approach. *J. Electrochem. Soc.* **2017**, *164*, E3132–E3145,

doi:10.1149/2.0121711jes.

33. Steinhauer, M.; Risse, S.; Wagner, N.; Friedrich, K.A. Investigation of the solid electrolyte interphase formation at graphite anodes in lithium-ion batteries with electrochemical impedance spectroscopy. *Electrochim. Acta* **2017**, *228*, 652–658, doi:10.1016/j.electacta.2017.01.128.

34. Noël, C.; Houssiau, L. Hybrid organic/inorganic materials depth profiling using low energy cesium ions. *J. Am. Soc. Mass Spectrom.* **2016**, *27*, 908–916, doi:10.1007/s13361-016-1353-9.

35. Das, S.; Attia, P.M.; Chueh, W.C.; Bazant, M.Z. Electrochemical kinetics of sei growth on carbon black: Part II. Modeling. *J. Electrochem. Soc.* **2019**, *166*, E107–E118, doi:10.1149/2.0241904jes.

36. Danner, T.; Singh, M.; Hein, S.; Kaiser, J.; Hahn, H.; Latz, A. Thick electrodes for Li-ion batteries: A model based analysis. *J. Power Sources* **2016**, *334*, 191–201, doi:10.1016/j.jpowsour.2016.09.143.

37. Colclasure, A.M.; Smith, K.A.; Kee, R.J. Modeling detailed chemistry and transport for solid-electrolyte-interface (SEI) films in Li-ion batteries. *Electrochim. Acta* **2011**, *58*, 33–43, doi:10.1016/j.electacta.2011.08.067.

38. Safari, M.; Delacourt, C. Aging of a commercial graphite/LiFePO4 cell. *J. Electrochem. Soc.* **2011**, *158*, A1123, doi:10.1149/1.3614529.

39. Tan, J.; Matz, J.; Dong, P.; Shen, J.; Ye, M. A Growing appreciation for the role of lif in the solid electrolyte interphase. *Adv. Energy Mater.* **2021**, doi:10.1002/aenm.202100046.

40. Guan, P.; Liu, L.; Lin, X. Simulation and experiment on solid electrolyte interphase (SEI) morphology evolution and lithium-ion diffusion. *J. Electrochem. Soc.* **2015**,

162, A1798–A1808, doi:10.1149/2.0521509jes.

41. Wang, A.; Kadam, S.; Li, H.; Shi, S.; Qi, Y. Review on modeling of the anode solid electrolyte interphase (SEI) for lithium-ion batteries. *npj Comput. Mater.* **2018**, *4*, doi:10.1038/s41524-018-0064-0.

42. Chattopadhyay, S.; Lipson, A.L.; Karmel, H.J.; Emery, J.D.; Fister, T.T.; Fenter, P.A.; Hersam, M.C.; Bedzyk, M.J. In situ X-ray study of the solid electrolyte interphase (SEI) formation on graphene as a model Li-ion battery anode. *Chem. Mater.* **2012**, *24*, 3038–3043, doi:10.1021/cm301584r.

43. Hasa, I.; Haregewoin, A.M.; Zhang, L.; Tsai, W.Y.; Guo, J.; Veith, G.M.; Ross, P.N.; Kostecki, R. Electrochemical reactivity and passivation of silicon thin-film electrodes in organic carbonate electrolytes. *ACS Appl. Mater. Interfaces* **2020**, *12*, 40879–40890, doi:10.1021/acsami.0c09384.

Chapter 6

SUMMARY AND OUTLOOK

6.1. Summary

The objective of this thesis was to develop 3D architected carbon electrodes with independently controllable micron-to-centimeter form factors and employ them as a model system to investigate battery kinetics at multiple length scales: transport in an electrolyte (sub-millimeter scale), transport in an electrode (micrometer scale), and kinetics related to SEI (nanometer scale), their competitions, and influences on battery performance.

First, we developed a simple method to manufacture 3D architected carbon electrodes for Li-ion batteries by combining DLP 3D printing and post-exposure pyrolysis. Microstructural characterizations revealed that 3D architected carbon had a disordered graphitic microstructure composed of several stacked graphitic layers, a characteristic microstructure of hard carbon. Uniaxial compression experiments demonstrate that structured carbon electrodes attained the maximum collapse stress of 27.1 MPa, corresponding to 101 kN m kg^{-1} of specific strength, comparable to the 6061 aluminum alloy used in aircraft. This suggests that the 3D architected carbon electrodes are promising as structural batteries for UAVs and eVTOLs, whose endurance time is more effectively improved by reducing the weight of structural and battery components than by increasing battery energy density.

The 3D architected carbon was demonstrated as a Li-ion battery anode with a liquid electrolyte and used as a model system to investigate structural factors and their influences on transports and battery performance. The combination of structural integrity and independent control capabilities from micrometer to millimeter, not feasible by other battery structural engineering methods, allowed us to investigate influences of independent control of electrode thickness, porosity, feature size, and surface morphology on battery performance in the framework of overpotential and ion transport kinetics in the electrode vs. electrolyte. The rate-limiting process of the 3D architected carbon electrodes tested under these parameter variations was estimated to be the diffusion in an electrode by characteristic

diffusion time calculations, which was experimentally verified. We discussed the rational design of battery electrodes and the limitations of the DLP-based method (i.e. long diffusion length in an electrode and high porosity).

Finally, the formation, structure, and resistance of SEI, and their position-dependency were investigated using the 3D architected carbon electrodes with the newly developed *in operando* DCS (Direct Current Spectroscopy) technique and post-characterization using SIMS. We introduced a new concept of ΔQ, which captures SEI growth during both discharge and charge, for estimating Li-ion consumptions to form SEI. We also proposed an influence of LiF on SEI resistance evolutions over cycling. We revealed that the SEI had increased F amount and decreased Li amount toward the side of the current collector. The composition distribution throughout the thick electrode implies that local SEI resistance distribution may contradict the previous estimation, which employed Newman's model with only Li-ions and solvents in an electrolyte as reactants for SEI formation. These experimental findings facilitate understanding of SEI at multiscale and developing aging models to precisely simulate battery degradations.

6.2. Outlook

Graphitization of 3D architected carbon electrodes

The 3D architected carbon used throughout this thesis is hard carbon, or non-graphitizable carbon, which does not transform into graphite by a simple annealing process at any temperatures [1]. Graphite is a standard anode of current commercial Li-ion batteries, and systematic study using 3D architected "graphite" electrodes will be of broad interest. One strategy to make 3D architected graphite is catalytic graphitization using a transition metal such as nickel. The nickel-containing resin can be made by dissolving nickel nitrate salt in ethanol and mixing it with a commercial photoresin (e.g. PR-48). During the pyrolysis process, nickel nitrate in the resin undergoes a solution combustion reaction to form Ni and NiO nanoparticles trapped in the carbon lattice matrix and facilitate graphitization (Figure 6. 1). Another strategy for graphitization is molten salt electrolysis, which removes oxygen in

the carbon and facilitates the realignment of graphitic layers in the molten $CaCl_2$ salt at ~1000°C [2,3].

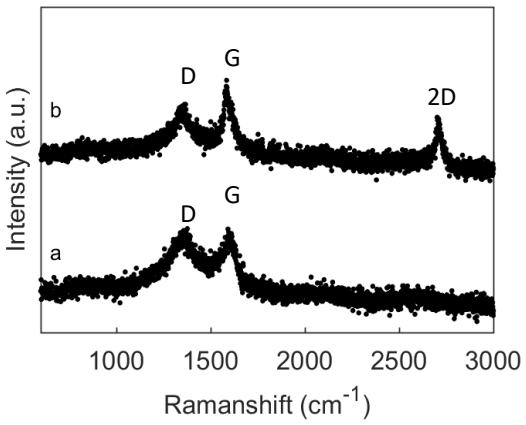

Figure 6. 1 Raman profiles of (a) photoresin-derived carbon pyrolyzed at 1000°C, and (b) Ni nitrate-containing photoresin-derived carbon pyrolyzed at 1000 °C.

3D architected carbon electrodes for engineering exploration

The 3D architected carbon has a potential for future studies in both engineering and science. From the viewpoint of engineering, the interconnected architecture, structural integrity, and flexible form-factors of 3D architected carbon enable 3D interdigitated full batteries, maximizing energy density and power densities by having short transport length between interdigitated anodes and cathodes, not available for planar cells-based batteries[4–6]. To create 3D interdigitated batteries, cathode and electrolyte materials can be filled into the porous structure of solid electrolyte coated architected carbon, which would withstand pressure during the infilling process. For instance, analytical calculations indicate that the volumetric capacity of 65%-porosity 3D architected carbon with lithium iron phosphate slurry infilled is comparable to that of planer electrodes composed of slurry electrodes with 70% of volume fraction of active materials (Figure 6. 2). Detailed calculations and assumptions are provided in Appendix.

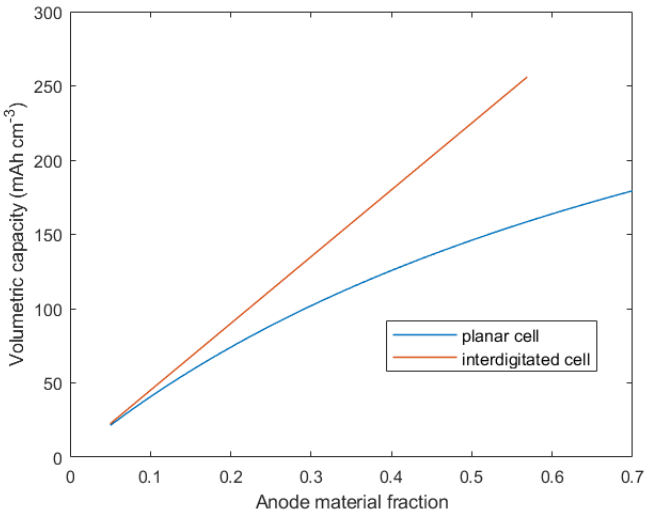

Figure 6. 2 Volumetric capacity change upon anode materials fraction for planar cell and interdigitated cell composed of pyrolytic carbon anode and lithium iron phosphate cathode materials

3D architected electrodes for scientific exploration

Scientifically, a deterministic porous structure with independently controlled electrode engineering factors can be used as a model system to investigate unexpected and undesired battery failure modes such as Li plating on carbon electrodes. The deterministic and prescribed structure allows us to precisely link monitored voltages and local potential distributions attributed to Li transport in porous electrode structures. For instance, electrochemical monitoring and in-situ optical microscopic observation with prescribed architectures that artificially induce high overpotential at specified positions may provide insights of Li-dendrite formation unexpected by monitored voltages. The understanding of local potentials and unexpected Li plating enables rational strategies for improving battery life and energy density by expanding the depth of discharge at high currents, which is often limited to avoid lithium metal plating and battery failure [7].

The recent development of additive manufacturing techniques enables 3D architected electrodes with different materials, including silicon [8], lithium cobalt oxide [9], and lithium sulfide [10]. The battery kinetics exploration using 3D pyrolytic carbon in this thesis does not require examinations of electrode volume change and electron transport due to near-zero

volume change during lithiation/delithiation and high electric conductivity of pyrolytic carbon. The electro-chemo-mechanical coupled battery dynamics and battery kinetics associated with electron and ion ambipolar diffusion [11] with prescribed 3D architected electrodes will be interesting to pursue as future explorations.

REFERENCES

1. Franklin, R.E. Crystallite growth in graphitizing and non-graphitizing carbons. *Proc. R. Soc. A Math. Phys. Eng. Sci.* **1951**, *209*, 196–218, doi:10.1098/rspa.1951.0197.

2. Peng, J.; Chen, N.; He, R.; Wang, Z.; Dai, S.; Jin, X. Electrochemically driven transformation of amorphous carbons to crystalline graphite nanoflakes: A facile and mild graphitization method. *Angew. Chemie - Int. Ed.* **2017**, *56*, 1751–1755, doi:10.1002/anie.201609565.

3. Zhu, Z.; Zuo, H.; Li, S.; Tu, J.; Guan, W.; Song, W.L.; Zhao, J.; Tian, D.; Jiao, S. A green electrochemical transformation of inferior coals to crystalline graphite for stable Li-ion storage. *J. Mater. Chem. A* **2019**, *7*, 7533–7540, doi:10.1039/C8TA12412D.

4. Hur, J.I.; Smith, L.C.; Dunn, B. High areal energy density 3D lithium-ion microbatteries. *Joule* **2018**, 1–15, doi:10.1016/j.joule.2018.04.002.

5. Werner, J.G.; Rodríguez-Calero, G.G.; Abruña, H.D.; Wiesner, U. Block copolymer derived 3-D interpenetrating multifunctional gyroidal nanohybrids for electrical energy storage. *Energy Environ. Sci.* **2018**, *11*, 1261–1270, doi:10.1039/c7ee03571c.

6. Pearse, A.; Schmitt, T.; Sahadeo, E.; Stewart, D.M.; Kozen, A.; Gerasopoulos, K.; Talin, A.A.; Lee, S.B.; Rubloff, G.W.; Gregorczyk, K.E. Three-dimensional solid-state lithium-ion batteries fabricated by conformal vapor-phase chemistry. *ACS Nano* **2018**, *12*, 4286–4294, doi:10.1021/acsnano.7b08751.

7. Gallagher, K.G.; Trask, S.E.; Bauer, C.; Woehrle, T.; Lux, S.F.; Tschech, M.; Lamp, P.; Polzin, B.J.; Ha, S.; Long, B.; et al. Optimizing areal capacities through understanding the limitations of lithium-ion electrodes. *J. Electrochem. Soc.* **2016**, *163*, A138–A149, doi:10.1149/2.0321602jes.

8. Xia, X.; Afshar, A.; Yang, H.; Portela, C.M.; Kochmann, D.M.; Di Leo, C. V.; Greer, J.R. Electrochemically reconfigurable architected materials. *Nature* **2019**, *573*, 205–

213, doi:10.1038/s41586-019-1538-z.

9. Yee, D.W.; Citrin, M.A.; Taylor, Z.W.; Saccone, M.A.; Tovmasyan, V.L.; Greer, J.R. Hydrogel-based additive manufacturing of lithium cobalt oxide. *Adv. Mater. Technol.* **2020**, *2000791*, 1–8, doi:10.1002/admt.202000791.

10. Saccone, M.A.; Greer, J.R. Understanding and mitigating mechanical degradation in lithium–sulfur batteries: additive manufacturing of Li_2S composites and nanomechanical particle compressions. *J. Mater. Res.* **2021**, 1–11, doi:10.1557/s43578-021-00182-w.

11. Usiskin, R.E.; Maier, J. Guidelines for optimizing the architecture of battery insertion electrodes based on the concept of wiring lengths. *Phys. Chem. Chem. Phys.* **2018**, *20*, 16449–16462, doi:10.1039/c8cp01946k.

A p p e n d i x

Appendix A: Estimation of Diffusion Length and Time

The porosity, ε for 3D architected carbon, was set to be the porosity of the designed 3D model in CAD: 10%. The porosities, ε for slurry, were calculated by

$$\varepsilon = \frac{mass\ loading}{electrode\ thickness * \rho_b}, \quad (A.1)$$

where ρ_b is a density of bulk materials. The mass loadings and electrode thickness were measured. 2.09 g cm^{-3} is used for the bulk density of graphite, and 1.8 g cm^{-3} for pulverized pyrolytic carbon. The bulk density of the pyrolytic carbon was obtained by making a circular plate made of pyrolytic carbon and measuring dimensions and weight. The intrinsic diffusion coefficient used for calculations in Equation (4.3) are 1.4×10^{-10} $cm^2\ s^{-1}$ for the electrode [1] and 3.2×10^{-6} $cm^2\ s^{-1}$ for the electrolyte [2].

Appendix B: Detailed Descriptions for Table 4. 1

The detailed explanations and the reasons for categories in the electrode engineering factors for each method of structural engineering are described here.

Conventional slurry:

The slurry electrode is the most conventional and commercially employed method. Its components are usually binders and conductive additives in addition to active materials, which are randomly stacked. The solid-diffusion length in an electrode corresponds to particle size and can be controlled independently by adjusting it. Tortuosity depends on the calendaring load and resultant porosity because of its randomly stacked geometry. Since the overall structure of stacked particles relies substantially on a calendaring load and the resultant structure is random and not designed, the structural integrity is not evaluated.

Slurry with anisotropic pores:

Anisotropic pore structures in slurry electrodes can be created by aligning active materials particles with external fields [3,4] or ice-templating methods [5,6] in the slurry making process. Laser ablating (cutting grooves) into the calendared slurry electrode is also included in this method. These methods can improve tortuosity compared with conventional slurry electrode structures at the same porosity. Billaud et al. used a magnetic field to align iron oxide nanoparticles-loaded graphite flakes along the though-thickness direction [3]. Park et al. demonstrated in 2019 that laser structured electrodes enhanced the rate capability of the electrode and specific energy while improving or retaining the power density, due to increased diffusion homogeneity and electrolyte wettability [7].

In this method, tortuosity is not coupled with a fraction of active materials, indicating the independent control capability of the fraction of the active material. However, since tortuosity can be controlled only into a specific range, it is evaluated as a “restricted factor.” Billaud et al. reported that the aligned structure was reorganized by calendaring load [3]; thus, the structural integrity is evaluated as “moderate.”

Slurry filled in 3D conductive framework:

The 3D conductive framework or 3D current collector is used to support slurry electrodes. It can increase a total electrode thickness and areal mass loading with a short distance of electron transport between the current collector and active material compared to conventional slurry electrodes cast on metallic sheets. This method still requires slurry electrodes composed of randomly packed active particles, binders, and conductive additives; the controllable factors are considered the same way as the conventional slurry electrode. The porous structure of slurry in the 3D current collector is random and not designed like conventional slurry. Therefore, structural integrity is not evaluated.

Planar thin film:

In planer thin film, solid-diffusion length in the electrode can be controlled by simply adjusting the thickness of the film of the active materials. Since there are almost no pores or spaces where electrolyte can be filled in, factors about tortuosity are not evaluated in this method. The structure is a solid film grown on a substrate, which is not designed as a complex 3D structure. Therefore, the structural integrity is not evaluated.

Thick monolith:

Thick monolith has been developed recently by Lai et al. using lithium cobalt oxide [8]. Since this method relies on necking formation between the polydispersed active material particles via sintering, which changes solid-diffusion length, tortuosity, and porosity simultaneously, all electrode engineering factors are in a dependent relationship. The monolith structure had a high relative density and a well-necked structure. Therefore, based on other studies of sintered ceramics [9], we assumed that this structure has good structural integrity even though mechanical properties have not been evaluated for the thick porous monolith made of battery materials.

Tortuosity value is taken from the report about calendared slurry electrodes [10] with a similar fraction of active materials to that of the thick monolith electrode demonstrated by Lai et al. [8].

Film on 3D conductive framework:

Another way to use the 3D current collector is by coating active materials on it. The morphology of the 3D current collector ranges from stochastic to periodic structure. Zhang et al. coated a thin film of active material on the 3D current collector-having an inverse opal structure-which enabled the very short diffusion path of ions in the electrode and good electron transport due to the 3D current collector [11]. In a similar manner to planar thin film, the solid-diffusion length in the electrode can be controlled independently by adjusting the film thickness, and a fraction of active materials can be controlled by changing the 3D current collector structure such as unit structure size for a periodic structure. Zhang et al. showed no structural change of NiOOH on nickel even after 100 cycles at a 6C rate; thus, structural integrity is evaluated as “good” [11].

Reference of reported values: solid-diffusion length in electrode and fraction of active materials are from [11,12]. Tortuosity is evaluated as nearly one from the report about tortuosity of periodic inverse opal structure [13].

3D monolith by sacrificial template:

3D porous monolith structures using sacrificial templates have been developed in various template methods, including but not limited to the usage of monodisperse particles (i.e. inverse opal) [14], bio-template [15], bicontinuous nanoporous alloy [16], and salt-template [17]. Inverse opal structure has determined tortuosity and active materials fraction (< 26 %), but can control solid-diffusion length by adjusting the wall thickness. Bio-template methods can hardly control all factors because the structure relies on the individuals which could be different. Solid-diffusion length and fraction of active materials are controllable using the method combining bicontinuous nanoporous alloy and selective etching [16]. The usage of the salt particles as a space holder can only control pore size distribution and porosity, but

not tortuosity or solid-diffusion length. Applying an external field to align the space holders can allow for low tortuosity (~1) for macro-pores [18]. However, the fabricated monolith had nano/micro-pores, which may have high and uncontrollable tortuosity for ion transport in the filled-in electrolyte. Since there are different methods to fabricate 3D monolith by sacrificial templates with different control capabilities in electrode engineering factors, we adopt the best categories: "independent factor" in solid-diffusion length in electrode from inverse opal structure, "restricted factor" in tortuosity from inverse opal structure, and "independent factor" in the fraction of active materials from the usage of space holders. Structural integrity is evaluated as "excellent" from the results of excellent mechanical properties of inverse opal structure [19,20].

Extrusion-based 3D printing:

Three electrode engineering factors in extrusion-based 3D printing were categorized into the correlated factor regardless of its macro/micro-control of depositing electrodes because precise control of its nano/microporous structure of active materials in a wide range has not been demonstrated. The active materials particles' size and fraction are limited to obtain suitable rheological properties to be extruded in a precise manner. The 3D architected silver electrode with a thickness of 400um showed cracks after cycling for 40 times due to volume expansion by 20%, although a 200um thick electrode retained the overall structure. Therefore, we evaluated the structural integrity as "moderate."

Reference of reported values is from [4,21–26]. There have not been reported tortuosity values for battery electrodes fabricated by extrusion-based 3D printing.

Lithography-based:

The lithography-based method has been actively investigated toward 3D interdigitated structure. Although reported battery electrodes fabricated by lithography-based techniques showed only 2.5D structure (the structure is only above its substrate geometry), all electrode engineering factors are controllable. This technique is often combined with other methods such as thin-film coating [27] and slurry inclusion [28]. Since each beam array is not

connected, and mechanical load must be supported by individual beams, especially for share stress, we evaluated its structural integrity as moderate. Full cells using silicon and lithium cobalt oxide showed cracks after cycling due to a significant expansion of silicon upon lithiation [28].

Table A.1 Parameter reported for each method for engineering electrode structures with reference numbers

	Solid-diffusion length in electrode (mm)		Tortuosity of diffusion path in electrolyte		Fraction of active materials (v/v)		Structural integrity
Method	min	max	min	max	min	max	
Conventional slurry	0.03[29]	25[30]	1[31]	12[31]	0.3[32]	0.75[32]	-
Slurry with anisotropic pores	0.05[33]	10 [4]	1.3 [33]	6.5[34]	0.24[4]	0.59[35]	Moderate[3]
Slurry filled in 3D conductive framework	0.05[36]	10[37]	1 [38]		0.20[36]	0.35[39]	-
Planar thin film	0.1[40]	15[41]	-	-	-	~1	-
Thick monolith	0.05[42]	2[43]	2[10]	3[10]	0.4[42]	0.87[8]	Good[9]
Film on 3D conductive framework	0.02[12]	0.2[11]	1[13]		0.14[12]	0.69[14]	Good[11]
3D monolith by sacrificial template	0.005[14]	10[17]	1[15]	3.3[17]	0.26[14]	0.68	Excellent[19]
Extrusion-based 3D print	0.1[21]	25[23]			0.06[44]	0.43[4]	Moderate[24]
Lithography-based	0.07[27]	50[45]	1[46]	3[27]	0.08[27]	0.2[28]	Moderate
DLP 3D printing-based (this work)	8	30	1		0.12	0.35	Excellent

Materials:

Conventional slurry: versatile

Particle alignment: LMO [4], LFP [5], Graphite [3], LCO [47], NMC [48]

Slurry filled in 3D current collector: versatile

Planar thin film: versatile

Thick monolith: LTO [49], LCO [8], LFP [42]

Film on 3D current collector: versatile

3D monolith by sacrificial template: versatile

Extrusion-based 3D print: C [50], LMFP [51], LTO [21], LFP [21], LMO [4], Ag [24], S [26]

Lithography-based: C [45], Si [28], Sn [27], LMO [27], LTO [52], LFP [52], LCO [28].

Appendix C: Analytical Calculations of Required Diffusion Length in the Electrode to Shift the Rate-Limiting Process

We analytically calculated the required diffusion length in the electrode to shift the rate-limiting process between diffusion in the electrode vs electrolyte. Electrode thickness, x_{th} can be related to the volume fraction of active material, RD, material density, ρ, and mass loading, ML:

$$x_{th} = \frac{ML}{RD \times \rho}. \quad \text{(A. 2)}$$

The rate-limiting process may be shifted when characteristic diffusion times in electrode and electrolyte are equivalent:

$$\frac{x_{rad}^2}{D^s} = \frac{x_{th}^2}{D_{eff}^l} \quad \text{(A. 3)}$$

where $x_{rad}$is the beam radius of architected carbon, D^s is the intrinsic diffusivity in carbon electrode, and D_{eff}^l is the effective diffusivity in the electrolyte filled in the porous electrode. Using Eqs. (A.2), (A.3), and Equation (4.2) in the main manuscript, we can obtain the required beam radius, x_{rad} to shift the rate-limiting process between transport within electrolyte vs. electrode, expressed by mass loading, ML and active material fraction, RD

$$x_{rad} = \sqrt{\frac{D^s}{D^l} \times \frac{1}{1-RD} \times \left(\frac{ML}{RD \times \rho}\right)^2} \quad \text{(A. 4)}$$

where D^s is the intrinsic diffusivity in the electrolyte. Here we assume that the tortuosity of architected carbon is unity due to its straight pore structure.

Appendix D: Analytical Calculations of Volumetric Capacity of a Planar Cell and 3D Interdigitated Cell

We analytically calculated the attainable volumetric capacity of a conventional planar full cell and 3D interdigitated full cell composed of pyrolytic carbon (250 mAh g^{-1}, 1.8 g cm^{-3}) and lithium iron phosphate (170 mAh g^{-1}, 3.5 g cm^{-3}). In a planar cell, we determined the cathode electrode thickness, L_c by matching capacities between the anode and cathode:

$$L_c = \frac{q_a \rho_a L_a \theta_a}{q_c \rho_c \theta_c} \quad \text{(A. 5)}$$

where L is the electrode thickness, ρ is the material density, θ is the volume fraction of active materials, and subscripts a and c denote the anode electrode and cathode electrode, respectively. We assume 70 vol.% of active materials in the cathode electrode. Volumetric capacity, Q_v is calculated by dividing areal capacity by cell thickness composed of anode and cathode electrodes, and simplified:

$$Q_v^{planar} = \frac{q_a \rho_a \theta_a \times q_c \rho_c \theta_c}{q_a \rho_a \theta_a + q_c \rho_c \theta_c}. \quad \text{(A. 7)}$$

We do not consider a separator and current collector to calculate volumetric capacity.

For an interdigitated electrode cell, since the anode thickness and cathode thickness are equivalent, the volumetric capacity of an interdigitated cell, Q_v^{id} can be expressed by

$$Q_v^{id} = q_a \rho_a \theta_a = q_c \rho_c \theta_c \quad \text{(A. 8)}$$

with feasible volume fractions of active materials (i.e. $\theta_a + \theta_c < 1$) in the capacity-matched anode and cathode.

Appendix E: Direct Current Spectroscopy (DCS) Technique for in-operando Cell Diagnostics and Anisotropic Resistance Monitoring

We demonstrate a new direct current (DC)-based technique that can measure resistance attributed to the dynamic response at different time constants. This technique, which we coin as *DCS (direct current spectroscopy)*, is capable of detecting the resistance anisotropy that emerges when the direction of applied current is reversed, distinguishing between the forward and reverse applied currents. Neither the EIS techniques nor other electrochemical techniques that use DC are capable of detecting these details. In this technique, a positive/negative direct current (DC) is applied to an electrochemical cell, and voltage evolution is measured and analyzed until the time constant of the dynamic process of interest is reached. The resistance evolution is obtained by dividing the overpotential at each given time by the applied current, analogous to the impedance evolution obtained by EIS. This DCS technique acquires data up to the time constant of the dynamic process of interest, which renders it significantly more efficient compared with, for example, EIS, which requires measurements at different frequencies separately. The DCS can be implemented by using a conventional DC supply/detector and can be easily integrated in other electrochemical tests such as galvanostatic cycling.

We investigated potential causes of the resistance difference that could emerge as a result of the opposite current directions in the DCS. We used a graphite-Li half cell discharged up to 0.09 V as the initial voltage, E_0. We first applied a positive pulse current over 0.3 s, relaxed the cell for 5 s, then applied the negative pulse current. The second DCS measurement was conducted in the opposite order of current directions; we first applied a negative current for 0.3 s, relaxed the cell for 5 s, and then applied the positive currents. The magnitude of the applied pulse currents was 100 mA. Figure A. 1 shows Bode magnitude plots obtained by DCS conducted at different current directions and in sequence steps. The voltages measured after each cell relaxation were self-consistent, indicating no observable SoC change due to the pulse currents. The difference in resistance caused by the reversal in the current direction was >10 ohm (Figure A. 1 (b)), which is 2x larger than the < 5 ohms difference in resistance caused by switching the sequential order of the applied current directions. These results suggest that the observed difference of resistances with opposite current directions is

attributed not to the history of applied currents, but to the directionality of resistances in the probed system.

We conducted the GEIS and PEIS measurements after the DCS techniques, with 100 mA of the magnitude of current perturbation in GEIS and 5 mV of the magnitude of potential perturbation in PEIS. Figure A. 1 includes Bode magnitude plots obtained by the DCS method, PEIS, and GEIS. The DCS method and GEIS measurement, both of which use currents as inputs and voltages as outputs, showed similar frequency-dependent resistances (or impedances). At lower frequencies than 30 Hz, GEIS showed close resistances within < 35 ohm difference to the ones obtained by the DCS method, whereas at the highest frequency of 80Hz, the difference of resistances was ~60 ohms between the DCS method and EIS methods.

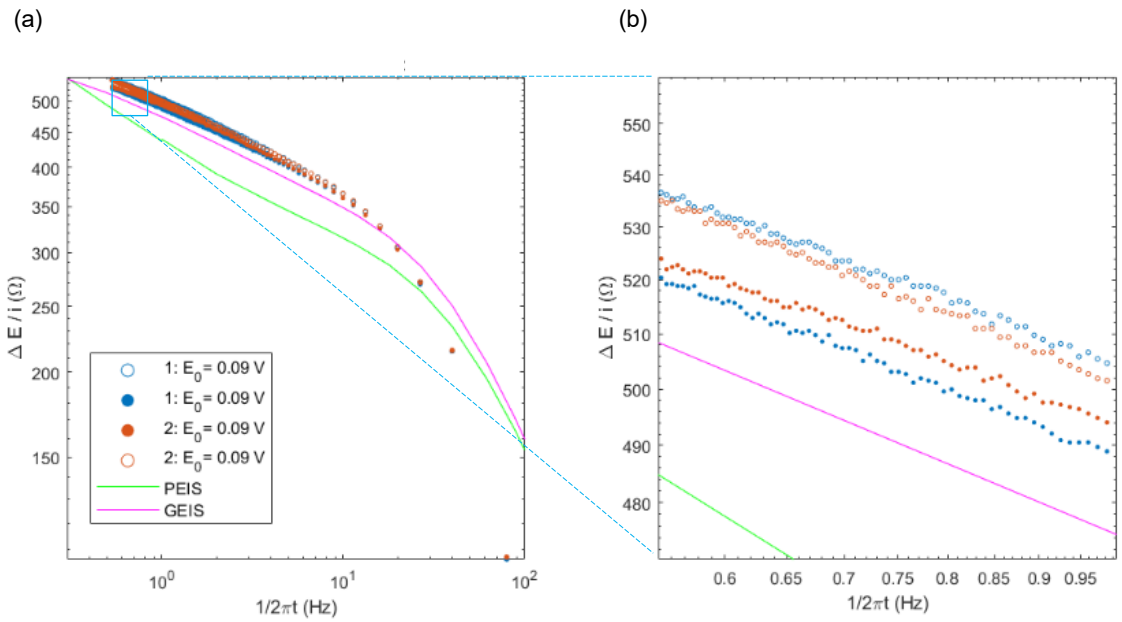

Figure A. 1 Comparison of the DCS method, PEIS and GEIS for Bode magnitude plots, (a) in the range of 3×10^{-1} to 10^{2} Hz, and (b) a close look of the square region in (a). DCS methods were conducted first with the order of positive (blue open circles) and negative (blue filled circles) currents, and then the order was switched in the second measurement to the order of negative (orange filled circles) and positive (orange open circles) currents.

Appendix F: Quantifying Sputtering Rates in SIMS

To quantify sputtering rates during SIMS analysis, we conducted line analysis by EDS on the cross-section of the sputtered area after the SIMS analysis. Figure A. 2 shows the comparison of depth profiles of 12C and 16O1H by SIMS and line analysis of C and O along the cross-section by EDS. Assuming a uniform sputtering rate in the SEI regardless of the SEI composition and porosity, the comparison of two sputtered regions provided 0.17 nm/s as a sputtering rate in the SEI region. To quantify the sputtering rate of the carbon electrode, we compared SIMS depth profiles and SEM images of Au-coated 3D architected carbon without battery cycling, which provided 0.25 nm/s as a sputtering rate in the carbon electrode.

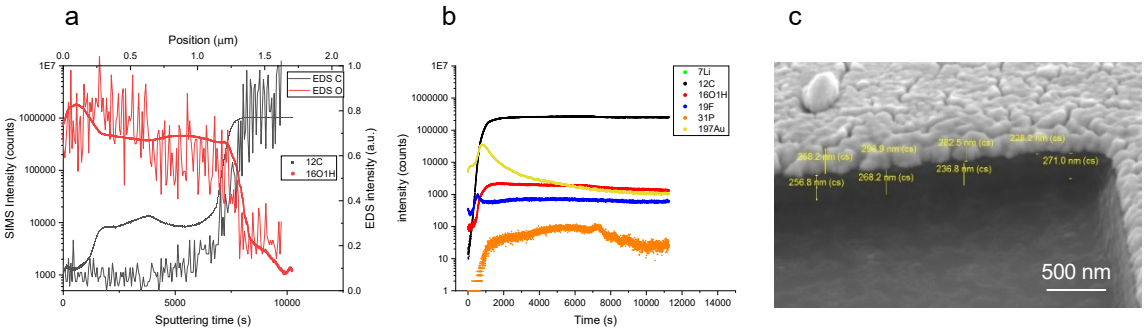

Figure A. 2 Comparison of SIMS depth profiles and ESD line scans. (a) 12C and 16O1H depth profiles by SIMS and line analysis of C and O by EDS to quantify sputtering rate during the SIMS analysis. (b) depth profiles of Au-coated 3D carbon without battery cycling, and (c) SEM image on the cross-section of the sputtered region of the Au-coated 3D carbon for SIMS depth analysis.

REFERENCES

1. Guo, H. Jun; LI, X. Hai; Zhang, X. Ming; Wang, H. Qiang; Wang, Z. Xing; Peng, W. Jie Diffusion coefficient of lithium in artificial graphite, mesocarbon microbeads, and disordered carbon. *New Carbon Mater.* **2007**, *22*, 7–10, doi:10.1016/S1872-5805(07)60006-7.

2. Valøen, L.O.; Reimers, J.N. Transport properties of $LiPF_6$-based Li-ion battery electrolytes. *J. Electrochem. Soc.* **2005**, *152*, A882, doi:10.1149/1.1872737.

3. Billaud, J.; Bouville, F.; Magrini, T.; Villevieille, C.; Studart, A.R. Magnetically aligned graphite electrodes for high-rate performance Li-ion batteries. *Nat. Energy* **2016**, *1*, 1–6, doi:10.1038/nenergy.2016.97.

4. Li, J.; Liang, X.; Liou, F.; Park, J. Macro-/micro-controlled 3D lithium-ion batteries via additive manufacturing and electric field processing. *Sci. Rep.* **2018**, *8*, 1–11, doi:10.1038/s41598-018-20329-w.

5. Huang, C.; Dontigny, M.; Zaghib, K.; Grant, P.S. Low-tortuosity and graded lithium ion battery cathodes by ice templating. *J. Mater. Chem. A* **2019**, *7*, 21421–21431, doi:10.1039/c9ta07269a.

6. Huang, C.; Grant, P.S. Coral-like directional porosity lithium ion battery cathodes by ice templating. *J. Mater. Chem. A* **2018**, *6*, 14689–14699, doi:10.1039/c8ta05049j.

7. Park, J.; Hyeon, S.; Jeong, S.; Kim, H.J. Performance enhancement of Li-ion battery by laser structuring of thick electrode with low porosity. *J. Ind. Eng. Chem.* **2019**, *70*, 178–185, doi:10.1016/j.jiec.2018.10.012.

8. Lai, W.; Erdonmez, C.K.; Marinis, T.F.; Bjune, C.K.; Dudney, N.J.; Xu, F.; Wartena, R.; Chiang, Y.M. Ultrahigh-energy-density microbatteries enabled by new electrode

architecture and micropackaging design. *Adv. Mater.* **2010**, *22*, 139–144, doi:10.1002/adma.200903650.

9. Munro, M. Evaluated material properties for a sintered alpha-alumina. *J. Am. Ceram. Soc.* **2005**, *80*, 1919–1928, doi:10.1111/j.1151-2916.1997.tb03074.x.

10. Lim, C.; Yan, B.; Kang, H.; Song, Z.; Lee, W.C.; De Andrade, V.; De Carlo, F.; Yin, L.; Kim, Y.; Zhu, L. Analysis of geometric and electrochemical characteristics of lithium cobalt oxide electrode with different packing densities. *J. Power Sources* **2016**, *328*, 46–55, doi:10.1016/j.jpowsour.2016.07.119.

11. Zhang, H.; Yu, X.; Braun, P. V Three-dimensional bicontinuous ultrafast-charge and -discharge bulk battery electrodes. *Nat. Nanotechnol.* **2011**, *6*, 277–281, doi:10.1038/nnano.2011.38.

12. Pikul, J.H.; Gang Zhang, H.; Cho, J.; Braun, P. V.; King, W.P. High-power lithium ion microbatteries from interdigitated three-dimensional bicontinuous nanoporous electrodes. *Nat. Commun.* **2013**, *4*, 1732–1735, doi:10.1038/ncomms2747.

13. Suter, S.; Haussener, S. Optimizing mesostructured silver catalysts for selective carbon dioxide conversion into fuels. *Energy Environ. Sci.* **2019**, *12*, 1668–1678, doi:10.1039/c9ee00656g.

14. Lee, K.T.; Lytle, J.C.; Ergang, N.S.; Oh, S.M.; Stein, A. Synthesis and rate performance of monolithic macroporous carbon electrodes for lithium-ion secondary batteries. *Adv. Funct. Mater.* **2005**, *15*, 547–556, doi:10.1002/adfm.200400186.

15. Lu, L.L.; Lu, Y.Y.; Xiao, Z.J.; Zhang, T.W.; Zhou, F.; Ma, T.; Ni, Y.; Yao, H. Bin; Yu, S.H.; Cui, Y. Wood-inspired high-performance ultrathick bulk battery electrodes. *Adv. Mater.* **2018**, *30*, 1–9, doi:10.1002/adma.201706745.

16. Wang, C.; Chen, Q. Reduction-induced decomposition: spontaneous formation of monolithic nanoporous metals of tunable structural hierarchy and porosity. **2018**,

doi:10.1021/acs.chemmater.8b01431.

17. Elango, R.; Demortière, A.; De Andrade, V.; Morcrette, M.; Seznec, V. Thick Binder-Free Electrodes for Li-Ion Battery Fabricated Using Templating Approach and Spark Plasma Sintering Reveals High Areal Capacity. *Adv. Energy Mater.* **2018**, *1703031*, 1–8, doi:10.1002/aenm.201703031.

18. Sander, J.S.; Erb, R.M.; Li, L.; Gurijala, A.; Chiang, Y.M. High-performance battery electrodes via magnetic templating. *Nat. Energy* **2016**, *1*, 1–7, doi:10.1038/nenergy.2016.99.

19. Lee, J.-H.; Wang, L.; Boyce, M.C.; Thomas, E.L. Periodic Bicontinuous Composites for High Specific Energy Absorption. *Nano Lett.* **2012**, *12*, 4392–4396, doi:10.1021/nl302234f.

20. Pikul, J.H.; Özerinç, S.; Liu, B.; Zhang, R.; Braun, P. V.; Deshpande, V.S.; King, W.P. High strength metallic wood from nanostructured nickel inverse opal materials. *Sci. Rep.* **2019**, *9*, 1–12, doi:10.1038/s41598-018-36901-3.

21. Sun, K.; Wei, T.S.; Ahn, B.Y.; Seo, J.Y.; Dillon, S.J.; Lewis, J.A. 3D printing of interdigitated Li-ion microbattery architectures. *Adv. Mater.* **2013**, *25*, 4539–4543, doi:10.1002/adma.201301036.

22. Fu, K.; Wang, Y.; Yan, C.; Yao, Y.; Chen, Y.; Dai, J.; Lacey, S.; Wang, Y.; Wan, J.; Li, T.; et al. Graphene oxide-based electrode inks for 3D-printed lithium-ion batteries. *Adv. Mater.* **2016**, *28*, 2587–2594, doi:10.1002/adma.201505391.

23. Li, J.; Leu, M.C.; Panat, R.; Park, J. A hybrid three-dimensionally structured electrode for lithium-ion batteries via 3D printing. *Mater. Des.* **2017**, *119*, 417–424, doi:10.1016/j.matdes.2017.01.088.

24. Saleh, M.S.; Li, J.; Park, J.; Panat, R. 3D printed hierarchically-porous microlattice electrode materials for exceptionally high specific capacity and areal capacity lithium

ion batteries. *Addit. Manuf.* **2018**, *23*, 70–78, doi:10.1016/j.addma.2018.07.006.

25. Wei, T.-S.; Ahn, B.Y.; Grotto, J.; Lewis, J.A. 3D printing of customized li-ion batteries with thick electrodes. *Adv. Mater.* **2018**, *1703027*, 1703027, doi:10.1002/adma.201703027.

26. Shen, K.; Mei, H.; Li, B.; Ding, J.; Yang, S. 3D printing sulfur copolymer-graphene architectures for Li-S batteries. *Adv. Energy Mater.* **2018**, *8*, 1–6, doi:10.1002/aenm.201701527.

27. Ning, H.; Pikul, J.H.; Zhang, R.; Li, X.; Xu, S.; Wang, J.; Rogers, J.A.; King, W.P.; Braun, P. V. Holographic patterning of high-performance on-chip 3D lithium-ion microbatteries. *Proc. Natl. Acad. Sci. U. S. A.* **2015**, *112*, 6573–6578, doi:10.1073/pnas.1423889112.

28. Hur, J.I.; Smith, L.C.; Dunn, B. High areal energy density 3D lithium-ion microbatteries. *Joule* **2018**, 1–15, doi:10.1016/j.joule.2018.04.002.

29. Kang, B.; Ceder, G. Battery materials for ultrafast charging and discharging. *Nature* **2009**, *458*, 190–193, doi:10.1038/nature07853.

30. Bitsch, B.; Dittmann, J.; Schmitt, M.; Scharfer, P.; Schabel, W.; Willenbacher, N. A novel slurry concept for the fabrication of lithium-ion battery electrodes with beneficial properties. *J. Power Sources* **2014**, *265*, 81–90, doi:10.1016/j.jpowsour.2014.04.115.

31. Ebner, M.; Chung, D.W.; García, R.E.; Wood, V. Tortuosity anisotropy in lithium-ion battery electrodes. *Adv. Energy Mater.* **2014**, *4*, 1–6, doi:10.1002/aenm.201301278.

32. Marks, T.; Trussler, S.; Smith, A.J.; Xiong, D.; Dahn, J.R. A Guide to Li-ion coin-cell electrode making for academic researchers. *J. Electrochem. Soc.* **2011**, *158*, A51, doi:10.1149/1.3515072.

33. Huang, C.; Dontigny, M.; Zaghib, K.; Grant, P.S. Low-tortuosity and graded lithium ion battery cathodes by ice templating. *J. Mater. Chem. A* **2019**, *7*, 21421–21431, doi:10.1039/c9ta07269a.

34. Kraft, L.; Habedank, J.B.; Frank, A.; Rheinfeld, A.; Jossen, A. Modeling and simulation of pore morphology modifications using laser-structured graphite anodes in lithium-ion batteries. *J. Electrochem. Soc.* **2020**, *167*, 013506, doi:10.1149/2.0062001jes.

35. Chen, K.H.; Namkoong, M.J.; Goel, V.; Yang, C.; Kazemiabnavi, S.; Mortuza, S.M.; Kazyak, E.; Mazumder, J.; Thornton, K.; Sakamoto, J.; et al. Efficient fast-charging of lithium-ion batteries enabled by laser-patterned three-dimensional graphite anode architectures. *J. Power Sources* **2020**, *471*, 228475, doi:10.1016/j.jpowsour.2020.228475.

36. Ji, H.; Zhang, L.; Pettes, M.T.; Li, H.; Chen, S.; Shi, L.; Piner, R.; Ruoff, R.S. Ultrathin graphite foam: A three-dimensional conductive network for battery electrodes. *Nano Lett.* **2012**, *12*, 2446–2451, doi:10.1021/nl300528p.

37. Wang, J.S.; Liu, P.; Sherman, E.; Verbrugge, M.; Tataria, H. Formulation and characterization of ultra-thick electrodes for high energy lithium-ion batteries employing tailored metal foams. *J. Power Sources* **2011**, *196*, 8714–8718, doi:10.1016/j.jpowsour.2011.06.071.

38. Shi, B.; Shang, Y.; Pei, Y.; Pei, S.; Wang, L.; Heider, D.; Zhao, Y.Y.; Zheng, C.; Yang, B.; Yarlagadda, S.; et al. Low tortuous, highly conductive, and high-areal-capacity battery electrodes enabled by through-thickness aligned carbon fiber framework. *Nano Lett.* **2020**, *20*, 5504–5512, doi:10.1021/acs.nanolett.0c02053.

39. Guan, X.; Zhang, Z.; Zhang, S.; Wang, Y.; Yang, H.; Wang, J.; Li, M.; Lu, H.; Li, Y.; Huang, Q.; et al. NIPS derived three-dimensional porous copper membrane for high-energy-density lithium-ion batteries. *Electrochim. Acta* **2019**, *312*, 424–431, doi:10.1016/j.electacta.2019.04.151.

40. Zhou, Y.N.; Xue, M.Z.; Fu, Z.W. Nanostructured thin film electrodes for lithium storage and all-solid-state thin-film lithium batteries. *J. Power Sources* **2013**, *234*, 310–332, doi:10.1016/j.jpowsour.2013.01.183.

41. Bates, J.B.; Dudney, N.J.; Neudecker, B.; Ueda, A.; Evans, C.D. Thin-film lithium and lithium-ion batteries. *Solid State Ionics* **2000**, *135*, 33–45, doi:10.1016/S0167-2738(00)00327-1.

42. Qin, X.; Wang, X.; Xie, J.; Wen, L. Hierarchically porous and conductive LiFePO4bulk electrode: Binder-free and ultrahigh volumetric capacity Li-ion cathode. *J. Mater. Chem.* **2011**, *21*, 12444–12448, doi:10.1039/c1jm11642h.

43. Bae, C.J.; Erdonmez, C.K.; Halloran, J.W.; Chiang, Y.M. Design of battery electrodes with dual-scale porosity to minimize tortuosity and maximize performance. *Adv. Mater.* **2013**, *25*, 1254–1258, doi:10.1002/adma.201204055.

44. Sun, C.; Liu, S.; Shi, X.; Lai, C.; Liang, J.; Chen, Y. 3D printing nanocomposite gel-based thick electrode enabling both high areal capacity and rate performance for lithium-ion battery. *Chem. Eng. J.* **2020**, *381*, 122641, doi:10.1016/j.cej.2019.122641.

45. Cirigliano, N.; Sun, G.; Membreno, D.; Malati, P.; Kim, C.J.; Dunn, B. 3D architectured anodes for lithium-ion microbatteries with large areal capacity. *Energy Technol.* **2014**, *2*, 362–369, doi:10.1002/ente.201402018.

46. Wang, C.; Taherabadi, L.; Jia, G.; Madou, M.; Yeh, Y.; Dunn, B. C-MEMS for the manufacture of 3D microbatteries. *Electrochem. Solid-State Lett.* **2004**, *7*, A435, doi:10.1149/1.1798151.

47. Li, L.; Erb, R.M.; Wang, J.; Wang, J.; Chiang, Y.M. Fabrication of low-tortuosity ultrahigh-area-capacity battery electrodes through magnetic alignment of emulsion-based slurries. *Adv. Energy Mater.* **2019**, *9*, 1–7, doi:10.1002/aenm.201802472.

48. Bolsinger, M.; Weller, M.; Ruck, S.; Kaya, P.; Riegel, H.; Knoblauch, V. Selective

surface treatment by means of IR-laser – A new approach to enhance the rate capability of cathodes for Li-ion batteries. *Electrochim. Acta* **2020**, *330*, doi:10.1016/j.electacta.2019.135163.

49. Robinson, J.P.; Ruppert, J.J.; Dong, H.; Koenig, G.M. Sintered electrode full cells for high energy density lithium-ion batteries. *J. Appl. Electrochem.* **2018**, *48*, 1297–1304, doi:10.1007/s10800-018-1242-y.

50. Maurel, A.; Courty, M.; Fleutot, B.; Tortajada, H.; Prashantha, K.; Armand, M.; Grugeon, S.; Panier, S.; Dupont, L. Highly loaded graphite-polylactic acid composite-based filaments for lithium-ion battery three-dimensional printing. *Chem. Mater.* **2018**, *30*, 7484–7493, doi:10.1021/acs.chemmater.8b02062.

51. Hu, J.; Jiang, Y.; Cui, S.; Duan, Y.; Liu, T.; Guo, H.; Lin, L.; Lin, Y.; Zheng, J.; Amine, K.; et al. 3D-printed cathodes of LiMn1−xFexPO4 nanocrystals achieve both ultrahigh rate and high capacity for advanced lithium-ion battery. *Adv. Energy Mater.* **2016**, *6*, doi:10.1002/aenm.201600856.

52. Cohen, E.; Menkin, S.; Lifshits, M.; Kamir, Y.; Gladkich, A.; Kosa, G.; Golodnitsky, D. Novel rechargeable 3D-Microbatteries on 3D-printed-polymer substrates: Feasibility study. *Electrochim. Acta* **2018**, *265*, 690–701, doi:10.1016/j.electacta.2018.01.197.